Spring 2002

Decomposition of Carbon Dioxide in a Capacitively Coupled Radio Frequency Discharge

Thao Hoang Dinh
Old Dominion University

DECOMPOSITION OF CARBON DIOXIDE IN A CAPACITIVELY COUPLED RADIO FREQUENCY DISCHARGE

by

Thao Hoang Dinh
B.S. May 1995, Old Dominion University

A Dissertation Submitted to the Faculty of
Old Dominion University in Partial Fulfillment of the
Requirements for the Degree of

DOCTOR OF PHILOSOPHY

PHYSICS

OLD DOMINION UNIVERSITY

May 2002

Leposava Vušković (Director)

Charles I. Sukenik (Member)

Gail E. Dodge (Member)

Gary E. Copeland (Member)

Robert L. Ash (Member)

ProQuest Information and Learning Company
300 North Zeeb Road
P.O. Box 1346
Ann Arbor, MI 48106-1346

ABSTRACT

DECOMPOSITION OF CARBON DIOXIDE IN A CAPACITIVELY COUPLED RADIO FREQUENCY DISCHARGE

Thao Hoang Dinh
Old Dominion University, 2002
Director: Dr. Leposava Vušković

Decomposition of CO_2 was studied in a capacitively coupled radio frequency discharge using Martian Simulant Gas mixture that contains 95% CO_2. The discharge was operated at a gas pressure of 3 to 6 Torr and a discharge power density of less than 2.0 W/cm^3. The main mechanism of the CO_2 decomposition process is the electron impact dissociation and the rate of the process depends on the electron density, N_e, the concentration of CO_2, and the reduced electric field, E/N. A self-consistent model was established to describe the CO_2 decomposition process based on these parameters. The model gave the microscopic description of the discharge in terms of the electron energy distribution function (EEDF) and electron mean energy T_e, electron density N_e, and dissociative rate coefficients. In addition, the CO_2 decomposition rate depends on all complex gas reactions during the discharge. A simplified set of major gas reactions was used to describe the rate of CO_2 decomposition in the discharge. The validity of the model was successfully verified by comparing the calculated results with the experimental results. The discharge characteristics such as T_e, N_e, and E/N, were determined by using the Langmuir probe technique, while the discharge temperature, T_g, was determined by using the CO rotational temperature that was obtained from the CO rotational emission spectrum, and compared with results obtained from the thermocouple measurements. The steady-state gas composition was measured using a quadrupole mass spectrometer. Measurement of gas composition in the discharge condition was within 5% of the prediction from the model. Due to a high power efficiency to decompose CO_2 by using an RF discharge, one direct application of the study is to produce oxygen on the planet Mars. In such an experiment, oxygen was extracted and diffused through a silver membrane used as one of the electrodes during

discharge. The oxygen flux produced by the present discharge condition was shown to reach about 5.0×10^{-14} $cm^{-2}s^{-1}$. The study of the CO_2 decomposition can be used in developing the optimum RF discharge conditions that yield the maximum oxygen flux production.

This thesis is dedicated to my beloved wife, Phuong Mai Nguyen,
and my lovely daughter, Diana AnhThu Dinh.

ACKNOWLEDGMENTS

It is my great pleasure to thank all the people who have helped and supported me in this work, and I hope these few words can express my gratitude.

I would like to thank my advisor, Leposava Vušković, who gave me constant help and suggestions about the research. Her insight of physics and beyond was always the most valuable thing for me to learn.

I would like to thank Svetoza Popovic, who gave me an infinite amount of his time in discussing the research with me and who suggested numerous physics ideas during the work. I also appreciate for all of his guidance and his help in writing the dissertation.

Many thanks also go to other members of my committee: Charles Sukenik, Gail Dodge, Gary Copeland, and Robert Ash for their critical review and suggestions on this work.

I want to thank the Physics Department of Old Dominion University for help and support, especially, Mr. Walt Hooks who was always willing to assist me.

Thanks to my fellow graduate students, in particular to George Brooke, Hugh Thurman, and Prasong Kessaratikoon. It was a pleasure to work with them and discuss physics.

A very special thanks "*Cám ơn rất nhiều*" to my wife, Phuong, who always supports me and bears with me through all years of the work, and my lovely daughter, Diana, who lifts my spirit by her joys and her smile. Many special thanks to my Dad, Thien, and my Mom, ThuLieu, my brothers, HoangThong, HoangThanh, and HoangThi, and my sisters, ThienThanh, and ThienThu, for their constant support and encouragement in so many ways.

TABLE OF CONTENTS

LIST OF TABLES

LIST OF FIGURES

Section 1
INTRODUCTION

The study of discharge processes in a CO_2 mixture was started in the middle of the 1970's when a CO_2 laser was shown to be one of the most efficient gas lasers (see, for example, [1-2]). However, the study emphasized the stability of CO_2 in a laser mixture that contained only a small amount of CO_2. Contrary to the study of laser discharges, this work emphasizes the CO_2 decomposition process in a discharge with a rich CO_2 mixture. The study could be further used to optimize discharge conditions for the CO_2 decomposition. A capacitively coupled radio frequency (CCRF) discharge was chosen due to its symmetric characteristics and power efficiency in comparison to its DC counterpart. The gas mixture used in this work contains 95.7% CO_2, simulating the Martian atmospheric composition gas. Hence, we named it Martian Simulant Gas (MSG).

The study of CO_2 decomposition in CCRF discharge was initiated by Shi et al. [3] in an attempt to use RF glow discharge to produce oxygen from CO_2 on Mars. They were surprised by the effectiveness of the technique in comparison to DC glow discharge. However, the mechanism of the process was not well understood, and the enhanced oxygen production flux at certain discharge configurations and conditions were not explained thoroughly. In order to understand these effects, we investigated the gas reactions in a similar mixture and discharge conditions by setting up a self-consistent gas kinetic model and by verifying the model through a series of experiments.

In CCRF discharge in a gas mixture with a large concentration of CO_2, the most active process is the electron impact dissociation of CO_2. In the first order approximation, the CO_2 decomposition rate is a function of the dissociation rate coefficient, electron density, and CO_2 density. In fact, the overall rate of CO_2 decomposition depends not only on dissociation of CO_2, but also on the CO_2 recombination rate during discharge. Hence, the CO_2 decomposition rate is also a function of all other gas reactions during discharge. Unlike other major gas reactions,

---

This dissertation follows the style of *The Physical Review*

electron impact dissociation depends directly on discharge power. During discharge, electrons gain energy from the RF field and transfer it to the molecules through vibration, rotation, excitation, dissociation, and ionization. The fraction of energy transfer attributed to each process depends on the magnitude of the corresponding cross section. The electron energy distribution in the discharge was obtained by solving the electron energy balance equation (e.g., Boltzmann equation). Then, rate coefficients of electron impact dissociation reactions could be calculated as a function of the field strength (e.g., discharge power). In the present model, only the dissociation rate coefficients of CO_2 and O_2 were calculated due to their high concentrations and low dissociation threshold energies. In addition, the fundamental discharge parameters, such as mean electron energy, T_e, mean electron density, N_e, and reduced electric field, E/N were derived from the model and were compared with the experimental values obtained with a Langmuir probe.

The first objective of the study was to establish a self-consistent model to describe the decomposition of CO_2 in a discharge. It includes an examination of the effect of microscopic parameters such as electron density, electron temperature, and electric field during CCRF discharge of CO_2, and an investigation of the influence of macroscopic parameters such as discharge pressure, temperature, and applied power on the rate of CO_2 decomposition. The second objective was to study the equilibrium and non-equilibrium conditions of CO_2 decomposition. The third objective was to optimize the CO_2 decomposition within the given range of the above parameters. The final objective was to consider the possibility of applying the work to Mars oxygen production or CO_2 reduction on Earth.

This dissertation is organized as follows: In Section 2, we will describe the model of the CO_2 decomposition process in CCRF discharge. It includes obtaining the electron transport solutions of the electron energy balance equation (e.g., Boltzmann equation) such as the dissociation rate coefficients, balancing all gas kinetic processes, and defining the spatial distribution of the field and charged particles between discharge gaps. In Section 3, we will discuss the experimental techniques to probe the discharge characteristics such electron density, electron temperature, reduced electric field and gas temperature as well as the measurement of steady-state gas composition. In Section 4, the comparison between the model and experimental results will be made, and we will

discuss one direct application of the study. Finally, we will develop conclusions in Section 5.

Section 2
GAS KINETIC MODEL OF RF DISCHARGE IN CO_2 WITH EMPHASIS ON MARTIAN SIMULANT GAS

2.1 Introduction

A model for Radio frequency glow discharges has been intensively investigated over the last few decades [4-11]. However, one of the major tasks remaining for researchers is to establish a self-consistent model for a particular discharge. The model should be able to describe correctly the microscopic behavior of electrons, such as the electron energy distribution function (EEDF), under the influence of external discharge parameters such as the applied electric field, gas pressure and gas composition. Then the values of the EEDF could be used to evaluate the electron transport properties such as average kinetic energy (e.g., temperature, T_e), drift velocity (V_d), mobility (μ_e), and diffusion coefficient (D_e). Knowing the electron transport coefficients one can predict quantitatively the discharge characteristics related to, for instance, chemical equilibrium (e.g., CO_2 dissociation rate coefficients, k_{CO_2}), or power dissipation. Three methods are widely used to describe the electron transport parameters in discharge. One popular approach is based on solving the Boltzmann equation in an approximation justified by discharge conditions; the second approach employs Monte Carlo particle interaction methods, and the third approach is a combination of the first two. For the discharge conditions of the present work, the use of the first, kinetic method is sufficient to evaluate the electron transport parameters with relatively short computational times.

In the kinetic model, the electron energy distribution function (EEDF) is obtained by solving the Boltzmann equation, specifically, by balancing the number of electrons in an elementary *phase space* volume. Simplified solutions of the model can be obtained by considering specific plasma conditions. In some cases, it is justified to treat the number of electrons in a unit volume as a constant. This is a reasonable approximation for a typical RF glow discharge, which is essentially a weakly ionized

plasma and consists largely of neutral particles (e.g., unexcited atoms or molecules) and a small fraction of charged particles (e.g., electrons and positive ions). The ratio of electron density or ion density to neutral density, defined as the ionization degree, is usually less than 10^{-5}. Therefore, in the present model, an ionization collision process is treated like the other electron energy dissipating processes: vibration, rotation, dissociation, and electronic excitation, neglecting the appearance of an additional electron after the ionization event. The dominant collisions are elastic. Another condition that simplifies the solution of the Boltzmann equation is treating the electron motion in the uniform electric field, E as in the DC field. This condition is applicable for the discharge if the electron collision frequency is much larger than that of the applied field, for example at pressures above 1 Torr and an RF frequency below 100 MHz.

One important property of the RF glow discharge is the state of non-equilibrium. Under the applied electric field, electrons start to accelerate and consequently increase their kinetic energy. In the course of acceleration toward the electrodes, the electrons mainly collide elastically with much heavier neutral particles. In fact, most scattered electrons increase their kinetic energies due to the effect of the applied electric field. As the result of net collisions and the influence of the field, the average energy of electrons becomes remarkably higher than the energy of the heavy particles. Therefore, the non-equilibrium state of the discharge plasma is manifested in different temperatures of electrons and heavy particles. A fraction of electrons keeps gaining more energy from the field until they reach the threshold for inelastic collisions. When inelastic collisions occur, electrons transfer most of their energy to the gas molecules and excite, ionize or dissociate the molecule. As a result, the population of electrons in the high-energy tail of the energy distribution decreases quickly as the energy increases. Thus, the combined result of all elastic and inelastic collision processes leads to a highly non-equilibrium electron energy distribution, and the EEDF shape is far from the Maxwellian distribution.

The self-consistent discharge model is based on not only the knowledge of EEDF (Section 2.2) but also on the type of gas mixture and the discharge configuration. A model should take into account all chemical reactions as well as the distribution of

electric field and the neutral density within the discharge. We will discuss the chemical reactions and its equilibrium in Section 2.3 based on the electron transport coefficients from the Boltzmann solution. The effect of the discharge electric field and gas density on the chemical reactions will be examined in Section 2.4.

2.2 Boltzmann Equations and Transport Coefficients of Electrons

The distribution of the electrons in their velocity space $\vec{v}$ at the space coordinate position $\vec{r}$ and at the time t is given by the electron velocity distribution function $f(\vec{r},\vec{v},t)$. The flow of the electrons through a unit velocity phase space volume with the distribution f in an applied electric field $\vec{E}$ is described by the Boltzmann transport equation [4-8]

$$\frac{\partial f(\vec{r},\vec{v},t)}{\partial t}+\vec{v}\cdot\vec{\nabla}_{\vec{r}}f(\vec{r},\vec{v},t)-\frac{e}{m}\vec{E}\cdot\vec{\nabla}_{\vec{v}}f(\vec{r},\vec{v},t)=\left(\frac{\partial f(\vec{r},\vec{v},t)}{\partial t}\right)_{coll}. \tag{1}$$

The right hand side of the equation represents the rate of change of f due to collisions of electrons with all particles present in the plasma. In the case of weakly ionized plasma, due to the low ion densities, this term takes into account only elastic and inelastic collisions between electrons and neutral atoms or molecules.

A complete general solution for Eq. (1) is impossible, and only approximate solutions are applied for certain cases. The homogeneous solution of Eq. (1) is usually assumed, which is true for the electrons in the bulk region of an RF glow discharge. In addition, a steady state solution is valid for the present discharge conditions where the electron collision frequency in the discharge is approximately two or three orders of magnitude larger than the driving frequency. Therefore, the electron distribution will reach equilibrium instantaneously with the applied electric field, and the discharge resembles a DC discharge. In the case of capacitive discharge, the solution can be further simplified by using symmetry about the discharge axis. The approximate solution is obtained by expanding it about the symmetry axis in a Legendre polynomial series and taking the first two terms of the expansion. By convention, the solution is expressed in terms of energy rather than velocity. Applying all the above conditions, a steady state isotropic solution can be obtained from the new form of Eq. (1) neglecting super-elastic collisions [9-11]

$$\begin{aligned}&\frac{1}{3}\left(\frac{eE}{N}\right)^2\frac{d}{du}\left(\frac{\varepsilon}{Q_m}\frac{df}{d\varepsilon}\right)+\frac{2m}{M}\frac{d}{d\varepsilon}\left(\varepsilon^2Q_m f\right)+\frac{2mkT}{M}\frac{d}{d\varepsilon}\left(\varepsilon^2Q_m\frac{df}{d\varepsilon}\right)\\&+\sum_j(\varepsilon+\varepsilon_j)f(\varepsilon+\varepsilon_j)Q_j(\varepsilon+\varepsilon_j)-\varepsilon f(\varepsilon)\sum_j Q_j(\varepsilon)=0.\end{aligned} \tag{2}$$

Q_m is the total elastic collision in the forward direction or the momentum transfer cross section; Q_j is the cross section of the j^{th} inelastic collision; m, e are the mass and charge of the electron; M, N, and T are the mass, density, and temperature of neutral gas molecules, respectively; k is the Boltzmann constant; $\varepsilon=mv^2/2$ is the electron energy where v is its velocity; f is the isotropic electron distribution function in the energy space (EEDF). The distribution function f satisfies the normalization condition

$$\int_0^\infty \varepsilon^{1/2} f(\varepsilon) d\varepsilon = 1. \tag{3}$$

Note that in Eq. (2), f depends only on the reduced electric field, E/N, and not on E or N separately. Here E is the effective field, and it relates to the field amplitude E_o by $E = E_{rms} = E_o/\sqrt{2}$.

For a gas mixture, an appropriate modification to the cross sections of all gas species in Eq. (2) should be taken into account: $Q_m = \sum Q_m^n G^n$ in the first term, $Q_m = \sum_n M Q_m^n G^n / M^n$ and $M = \sum_n M^n G^n$ in the second and third term. Here Q_m^n is the momentum transfer cross section, G^n is the mole fraction, and M^n is the mass of the molecule of the n^{th} gas [11].

Equation (2) is a non-linear second order differential equation, and it can be solved numerically. In the present research the EEDF is obtained by employing a computer code based on the technique of Pitchford, O'Neil, and Rumble [6] retaining only the first two terms in the Legendre polynomial expansion.

Electron transport coefficients and electron-molecule collision rates are derived from the EEDF. The most important rates and transport parameters that affect directly the chemical kinetic model are the reduced average electron energy T_e, drift velocity v_d, and rate constants k_i of certain processes:

$$T_e = \frac{2}{3}\bar{\varepsilon} = \frac{2}{3}\int_0^\infty \varepsilon^{3/2} f(\varepsilon) d\varepsilon, \tag{4}$$

$$v_d = -\left(\frac{2e}{m}\right)^{1/2} \frac{E}{3N} \int_0^\infty \frac{\varepsilon}{Q_m}\left(\frac{df}{d\varepsilon}\right) d\varepsilon, \tag{5}$$

$$k_j = \left(\frac{2e}{m}\right)^{1/2} \int_0^\infty \varepsilon Q_j(\varepsilon) f(\varepsilon) d\varepsilon . \quad (6)$$

Evaluating numerical values of the EEDF and electron transport coefficients for a particular gas mixture requires a set of its electron-molecule collision cross sections (see Eq. (2), (5), and (6)). Since the EEDF and electron transport coefficients are the fundamental parameters to establish a discharge model, a realistic discharge model for a gas mixture depends on reliable cross section data. In general, the collision cross sections are obtained from experiments or *ab initio* calculations. Unfortunately, not all gas mixtures have a complete set of electron-molecule collision cross sections; therefore, a limited and best available set of cross sections is usually used instead.

The gas mixture used in this research approximates Martian atmosphere, and it is called Martian Simulant Gas (MSG). MSG at the research grade of 99.99% consists of CO_2 (95.71%) with a minor concentration of other gases N_2 (2.75%), and Ar (1.54%).[1] During discharge, CO, O_2, and O are the major additional species, while other species are considered negligible. Hence, only the collision cross sections of the primary gas molecules CO_2, CO, O_2, O, N_2, and Ar are considered in evaluating EEDF and other transport parameters. These cross section data are compiled from many sources with special attention to CO_2, CO, and O_2 species. Most of these data are already well established from various experiments and theoretical calculation elsewhere [11-21]. Some collision cross sections, however, still need to be investigated further in order to improve the agreement between experiments and theory. Fortunately, the overall effect of the discrepancy between different cross section data on the EEDF results in the present case is rather negligible, especially in the low electron energy collision regions.

CO_2 data have vast applications in atmospheric studies, gas discharges, astrophysics, etc., but a comprehensive set of electron impact collision cross sections for CO_2 is still unavailable. Therefore, we will give below the description of the most available set of CO_2 cross section data.

---

[1] 100 ppm of OH radical was detected in the RF discharge of MSG.

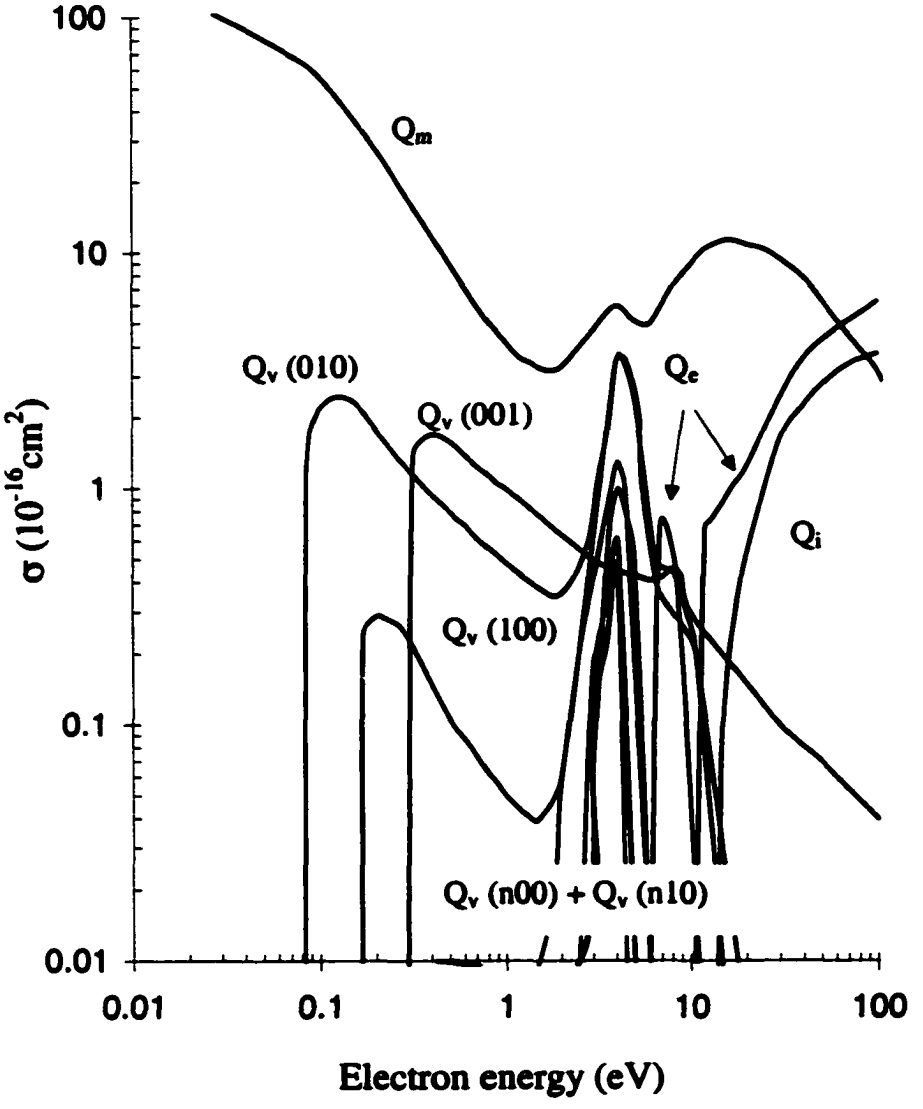

FIG. 1. Electron collision cross sections for CO_2 from Ref. [16]: Q_m, momentum transfer cross section; Q_v, vibrational excitation cross section; Q_e, electronic excitation cross section; Q_i, ionization cross section.

The CO_2 momentum transfer cross section possesses two dips, the first dip around 2 eV and the second dip around 6 eV (Fig. 1). Hake and Phelps [12] gave a major set of the CO_2 collision cross sections, including the momentum transfer cross section, based on swarm transport coefficients. In a model for a laser gas mixture, Lowke, Phelps and Irwin [11] improved cross sections based on newer CO_2 data. A few years later Shyn et al. [13] obtained similar values for the momentum transfer cross section data; however, at energies above 10 eV, their results are lower by 20% than those of Lowke. Register et al. [14] later reported even lower values of the momentum transfer cross section for CO_2 at 4, 10, 20, and 50 eV. More recently, Nakamura [16] obtained another set of CO_2 cross section data from swarm experiments with pure CO_2 and a dilute gas-rare gas mixture. He showed momentum transfer cross section data in close agreement with that of Register et al. [14]. In the newest theoretical studies of CO_2 momentum transfer cross section, Takekawa and Itikawa [17] calculated the cross section based on the *fixed-nuclei approximation* with an *ab initio* electrostatic interaction potential. Their results were in reasonable agreement with experimental data.

Within the inelastic collision cross sections of CO_2, the most important cross sections are three fundamental vibrational excitations: bending (010), symmetric stretch (100), and anti-symmetric stretch (001). These vibrational excitations (010), (100) and (001) are designated as Π_u, Σ_g^+, and Σ_u^+ states with threshold energies of 0.083, 0.167, and 0.291 eV, respectively (Fig. 1). The most common feature among these vibration cross sections is a sharp increase at their threshold energies. Except for the antisymmetric mode, all of the bending, symmetric stretch, and other higher vibrational excitation cross sections (n00) and (n10) have a strong resonance peak around 4 eV. At the resonance peak of vibration cross sections, Nakamura [16] obtained higher values in comparison to the results of Lowke, Phelps, and Irwin [11]. In recent theoretical studies, Takekawa and Itikawa [18-19] showed a similar result for the antisymmetric cross section, but a small energy shift at the resonance peak and slow decaying trends for the energy above 10 eV in both symmetric and bending modes.

The other major inelastic collision cross sections of CO_2 are the electronic excitation cross sections with threshold energies at 6.1 eV and 10.5 eV. The first excitation, designated as the $^3\Pi$ state of CO_2, rises to a maximum around 7 eV and is

known as the main contribution to CO_2 dissociation [12,20]. The cross section for the second peak has a sharp increase at its threshold and continues increasing at higher energies. Nakamura [16] obtained a smaller magnitude for the 7 eV cross section and a larger magnitude for the 10.5 eV cross section in comparison to Hake [12]. The electronic excitation cross section for dissociative attachment with peaks around 4 eV and 8 eV, originally obtained by Rapp and Englander-Golden [21], is also included in the set, but it is two orders of magnitude smaller than the other cross sections. Finally, the CO_2 ionization cross section with a threshold at 13.8 eV was obtained by Hake and Phelps [12] and is accepted and applied in most discharge models. Figure 1 represents a summary of major CO_2 electron collision cross sections that are in reasonable agreement with both experimental and theoretical results and are widely accepted in gas discharge models.

CO is one of the primary products during CO_2 decomposition and its presence in the discharge affects the way energy is distributed among the electrons. We will use the most available set of CO cross section data. Hake and Phelps [12] obtained a set of CO cross section data based on swarm transport coefficients. Land [22] later recompiled CO cross section data base on a vast range of electron transport coefficient data and improved the results of Ref. [12]. It is considered the most complete and available set of electron impact cross section for CO, and it has been tested and applied in many discharge models involving CO. Similar to CO_2 cross section data, CO elastic and inelastic cross section data feature two resonance peaks around 2 and 10 eV (see Fig. 2). The major electronic excitations for CO are the $a^3\Pi$, $a'^3\Sigma$, $A^1\Pi$, $b^3\Sigma$, $C^1\Sigma$, and $E^1\Pi$ states and an excitation with the threshold energy at 13.5 eV. Recently, Middleton et al. [23] reported an additional differential cross section set for CO electronic excitation states. However, more data are needed in order to obtain the total electronic excitation cross section. Therefore, we will use the available CO cross section data compiled by Land [22] as shown in Fig. 2.

Molecular oxygen is another major product in MSG discharge. It results from the recombination of atomic oxygen produced from CO_2 dissociation. Therefore, the O_2 cross section data are also needed for inclusion in the present model. Figure 3 represents the O_2 momentum cross section and other inelastic cross sections which are taken from

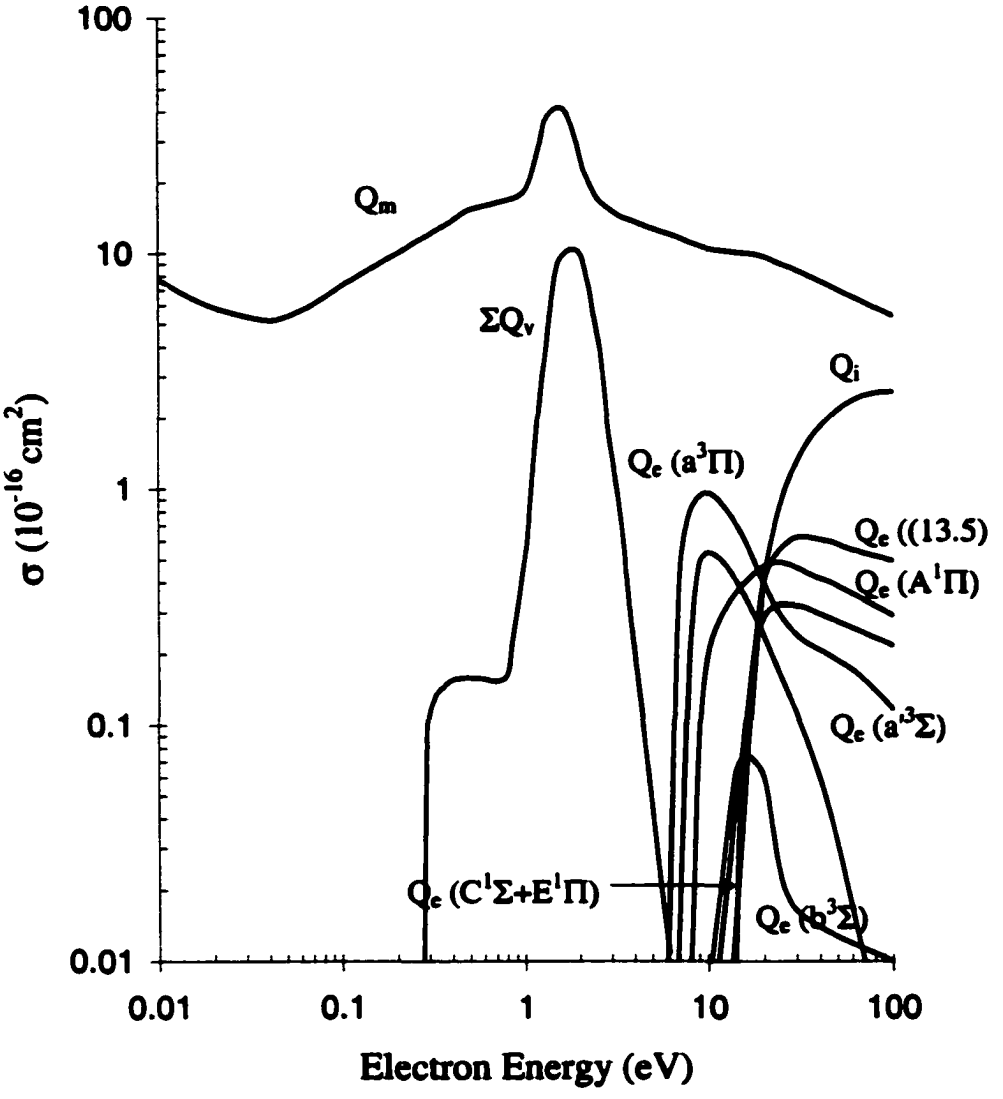

FIG. 2. Electron collision cross sections for CO from Ref. [22]: Q_m, momentum transfer cross section; Q_v, vibrational excitation cross section; Q_e, electronic excitation cross section; Q_i, ionization cross section.

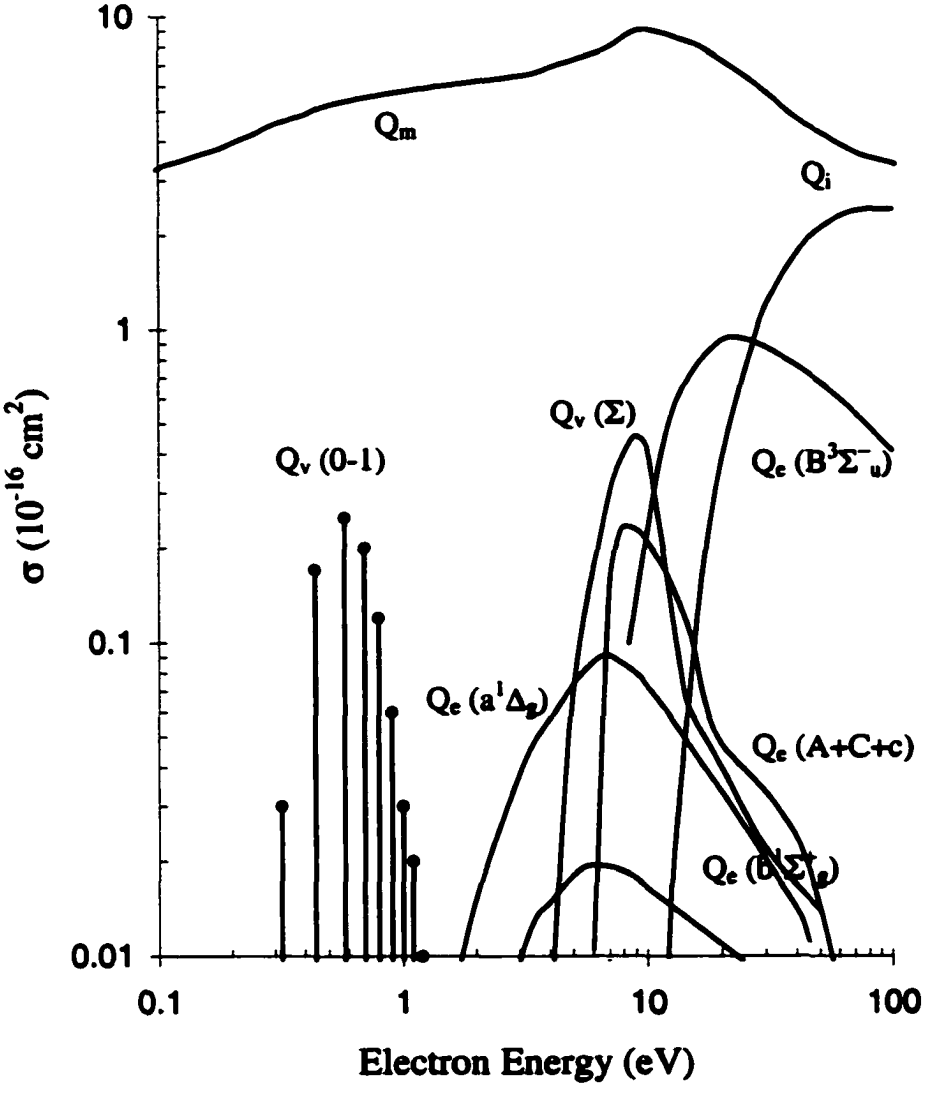

FIG. 3. Electron cross sections for O_2 from Ref. [24] and [25]: Q_m, momentum transfer cross section; Q_v, vibrational excitation cross section; Q_e, electronic excitation cross section; Q_i, ionization cross section.

references [24-25]. The magnitude of the dissociative attachment cross section is too small to show in the figure. Note that the O_2 electron collision cross sections are several times smaller than those of CO_2 and CO; therefore, the contribution of the O_2 cross section to the EEDF result will be minimal. The same effect could be applied to O, N_2, and Ar due to their small concentrations in the MSG mixture. The electron cross section data for O and N_2 are summarized by Itikawa [25] and for Ar are given by Frost and Phelps [9,25].

The accuracy of numerical results can be verified by comparing calculated results with other data for a particular gas. Figure 4 is a comparison of the EEDF values obtained by the present model at gas temperature of 300 K and by Nighan [27] for pure CO_2 gas. At higher values of reduced electric field *E/N*, both of the EEDF values are the same. However, the disagreement between the present EEDF and Nighan data increases as *E/N* decreases. The discrepancy arises due to the difference in the CO_2 electron collision cross sections used in the present model and in the Nighan model. As we have seen in the previous paragraph, the present model employed a set of CO_2 collision cross sections that have a larger magnitude for the bending and symmetric vibration cross sections around 4 eV in comparison to the earlier cross section data used by Nighan. As a result, the energetic electron population drops around this value of energy, and a smaller EEDF was obtained in the present model. The electron loss becomes more obvious at small values of reduced electric field when not many energetic electrons are present in the discharge. The electron loss is minimal when *E/N* is high enough so that more energetic electrons are produced than lost. Furthermore, the loss of energetic electrons depends on electronic cross sections and ionization cross sections and they agree in both models. Therefore, the agreement in Fig. 4 has confirmed the validity of the EEDF numerical results for the present model for pure CO_2 gas.

EEDF in the current range of *E/N* is not in equilibrium due to inelastic collisions. Electrons do not have a Maxwellian distribution; e.g., EEDF is not represented by a straight line on an energy plot. Figure 4 is an example to show this characteristic. All EEDF in the figure have two major population depletions around 0.1 eV and 4.0 eV. The first drop is due to the sharp increase of three fundamental vibrational excitation cross sections at their threshold energies. The latter reflects the energy loss of electrons

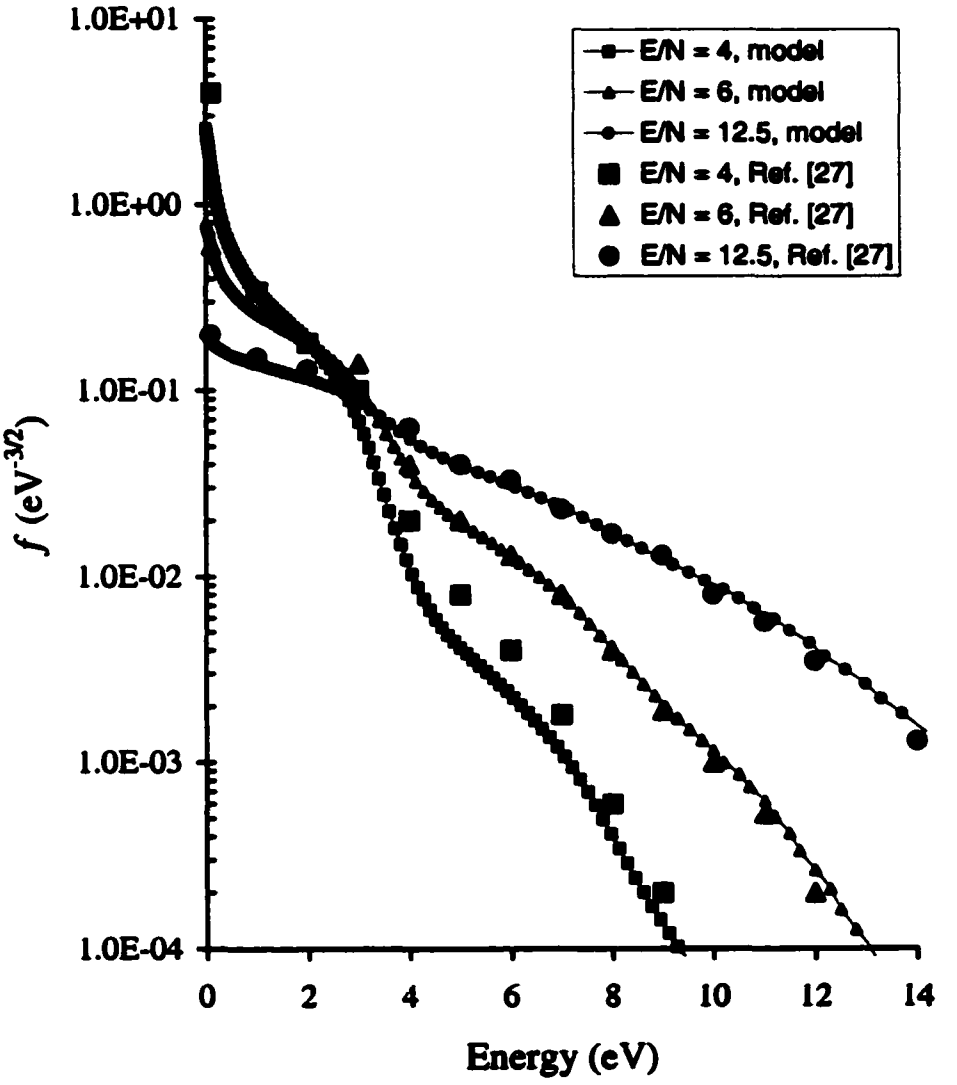

FIG. 4. Electron energy distribution function in a pure CO_2 discharge at various reduced electric fields, *E/N*, in units of 10^{-16} Vcm^2.

due to the resonant peak of elastic and bending, symmetric stretch and other higher vibration modes. The EEDF has a plateau over the energy range from 1.0 to 4.0 eV where electron loss comes mainly from momentum transfer collisions. The mean electron energy in the plateau resembles closely the Maxwellian temperature that can be measured using a Langmuir probe. Figure 4 also shows that the EEDF has a steeper slope at larger *E/N* and approximates Maxwellian characteristics. At a constant gas density, *N*, the number of energetic electrons increases proportionally with the field strength, *E*, which implies a higher mean electron energy.

The results can be extended to the MSG mixtures by taking into account all cross sections of CO_2, CO, O_2, O, N_2 and Ar with their appropriate mole fractions in Eq. (2). In addition, the MSG mixture also varies due to the decomposition of CO_2 during RF discharge, and CO and O_2 are the other dominant constituents in the mixture. Figure 5 shows an example of different EEDFs for a selected mixture of CO_2, CO, and O_2 at gas temperature of 300 K that may represent of the reacted MSG mixture during discharge. As the percentage of CO and O_2 increases due to the CO_2 dissociation, there is a decrease in the number of fast electrons in the EEDF, due to the presence of a large number of inelastic excitation processes such as electronic and rotational excitations of CO and O_2. On the other hand, the number of slow electrons increases due to the decreasing number of vibrational excitations of CO_2. As a result, the values of mean electron temperature and the dissociation rate of CO_2 can be changed slightly due to this variation of the EEDF. In the Section 2.2, we will investigate the variation of dissociation rates due to the change of gas mixtures because of chemical reactions happening during RF discharge.

The electron average energy is also referred to as the mean electron temperature, which is one of most important transport coefficients in plasma discharge. This can be obtained immediately from the EEDF by using Eq. (4). Figure 6 shows the mean electron temperature T_e as a function of reduced electric fields, *E/N*. T_e varies nearly linearly with *E/N* in the discharge of the MSG mixture. Thus, at a fixed discharge pressure, T_e increases with increases in the magnitude of the applied field, and therefore with the applied discharge power at a fixed discharge volume. The larger mean electron temperature will increase the rate of CO_2 and O_2 dissociation since a larger T_e means a

larger number of energetic electrons. Therefore, more electrons are able to dissociate gas molecules.

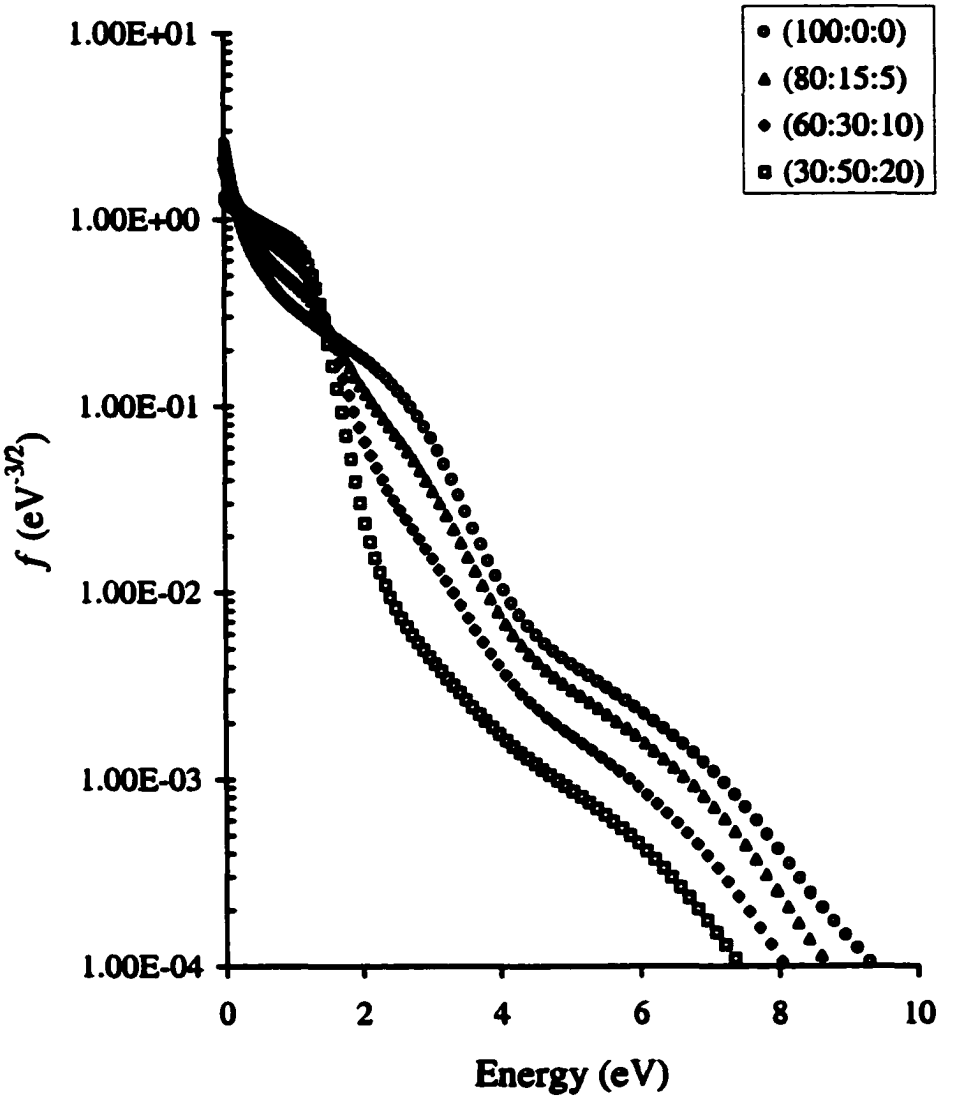

FIG. 5. Electron energy distribution function in various gas mixtures (CO_2:CO:O_2) at $E/N = 4 \times 10^{-16}$ Vcm^2.

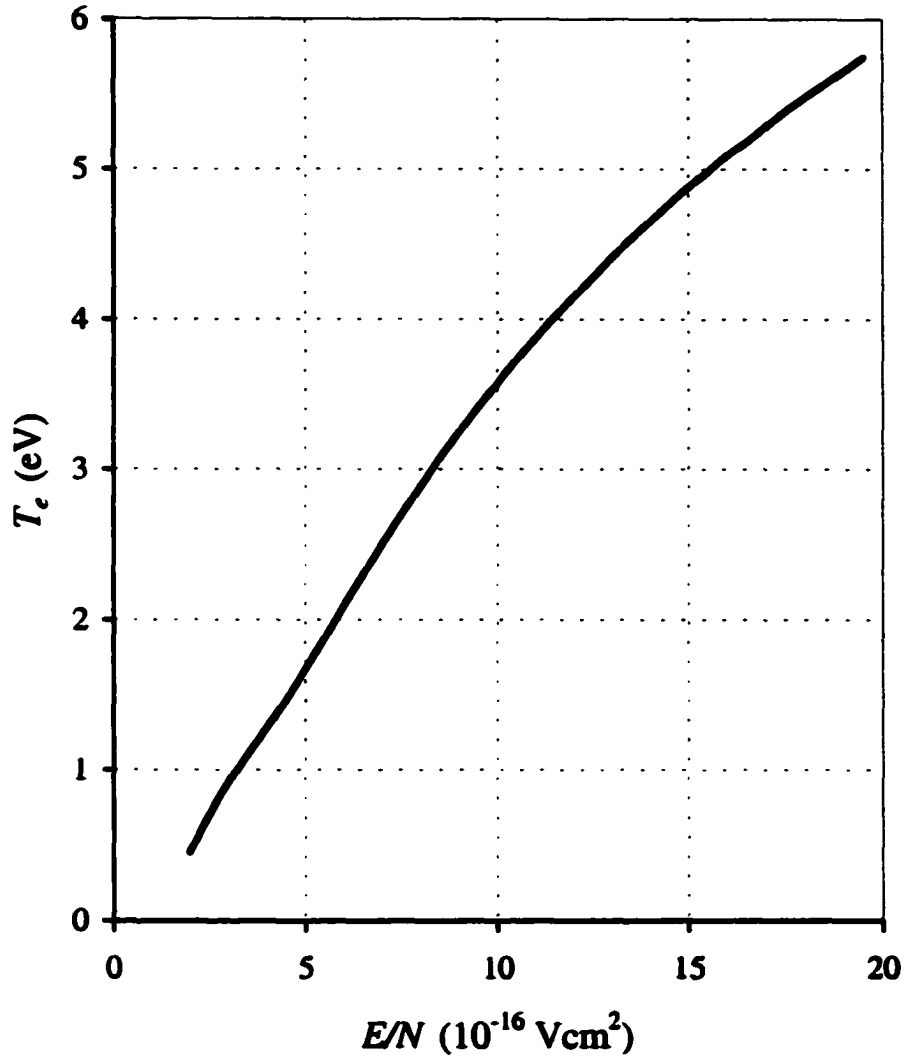

FIG. 6. Electron temperature as a function of the reduced electric field.

The dissociation rate coefficients of CO_2 and O_2 (k_{CO_2} and k_{O_2}) and the electron drift velocity (V_d) are obtained by using Eq. (5) and (6) with the electron impact dissociation cross section at a threshold energy of 7 eV for CO_2, and 4.5, 6.0, and 8.4 eV for O_2. Figure 7 shows the dissociation rate coefficients of CO_2 and O_2 and the electron drift velocity as a function of the reduced electric field *E/N* for the MSG mixture. The electron drift velocity is nominally constant over the range of *E/N* studied. On the other hand, the CO_2 and O_2 dissociation rate coefficients increase strongly with the reduced field. This can be explained in terms of the increasing number of energetic electrons that reach the CO_2 dissociative threshold energy. The rate of oxygen dissociation is only slightly greater than that of CO_2 at the small values of the reduced field *E/N*. However, as *E/N* increases the difference between these rate coefficients becomes significant. This effect can be explained by comparing the excitation cross sections that result in the dissociation of CO_2 and O_2. For O_2 molecules, these cross sections span a wider range of energy in contrast to the sharp peak for CO_2. In addition, the 8.4 eV energy-loss cross section that contributes to dissociation of O_2, extends to higher electron energy. Therefore, as the reduced field increases, the mean electron energy increases (Fig. 6) and a larger number of electrons dissociate the oxygen.

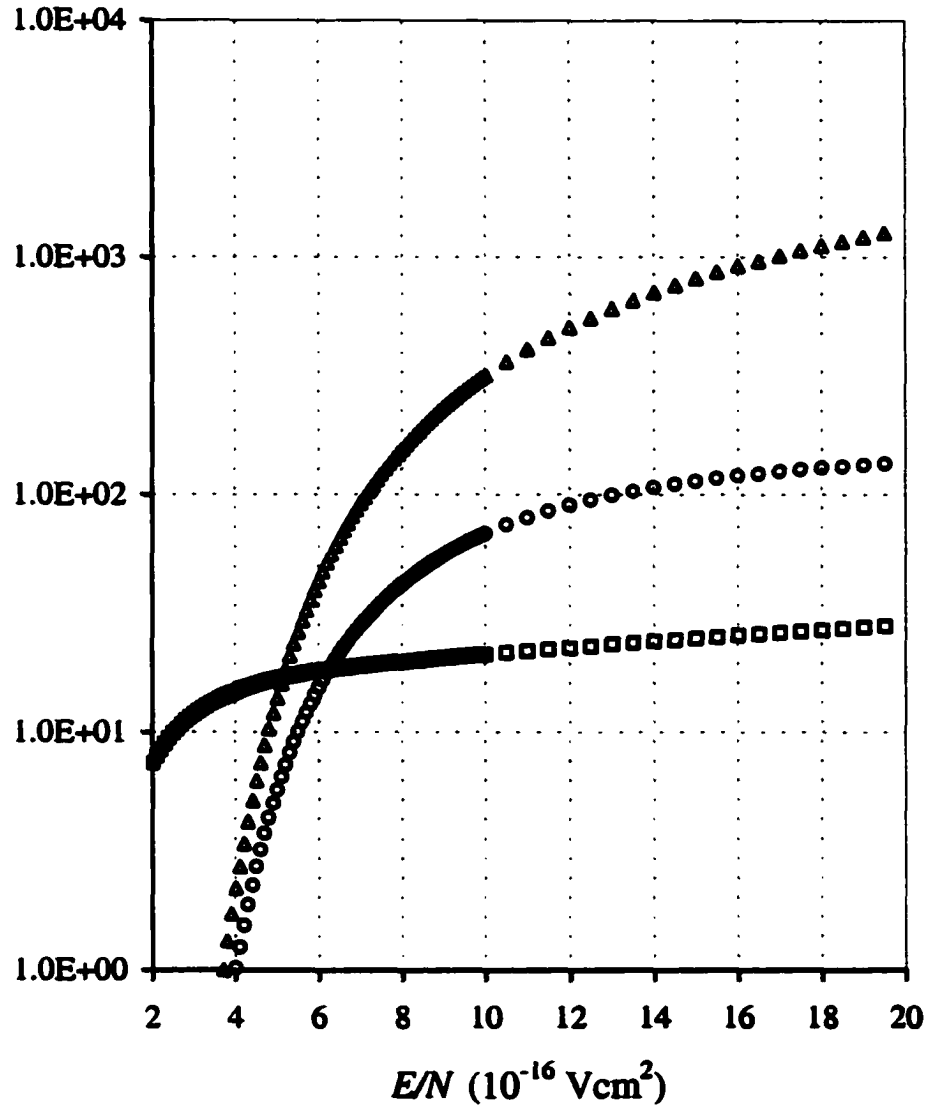

FIG. 7. Dissociation rate coefficients, k_{CO_2} and k_{O_2}, and electron drift velocity, V_d as a function of reduced electric field, E/N: ○, k_{CO_2} (10^{-11} cm^3/s); △, k_{O_2} (10^{-11} cm^3/s); □, V_d (10^7 cm/s).

2.3 Gas Phase Chemical Kinetics

Gas phase chemical kinetic analysis is a necessary procedure in every molecular discharge because the dissociation rate is a major concern in most discharges involving molecular gases. In this work, we consider the dissociation and reformation rates of CO_2 within an MSG mixture exposed to the radio-frequency discharge. In contrast to the CO_2 laser modeling, where the dissociation level is minimized, we investigate the conditions that maximize the dissociation rate of the CO_2 in the discharge.

In Appendix A, we have listed the most probable gas phase chemical reactions in the radio-frequency discharge of the MSG mixture. These reactions emphasize the loss and the formation of the active species such as CO_2, CO, O_2, O, and O_3, which are the primary gas components in this mixture. In the MSG mixture, N_2 gas (2.7%) is a buffer gas during the discharge and does not react with others constituents. It plays the role of a third body in the three body reactions or acts as an agent of energy transfer in the dissociation of oxygen molecules (Section 2.2). Argon, the only inert gas in the MSG mixture with a concentration of less than 2%, is likely the main source of positive ions to create the space-charge neutrality of the plasma in the bulk region (the number of Ar metastable atoms is small for the discharge conditions due to the collisional de-excitations or collisions with electrode surfaces). Even though Ar has a higher ionization threshold from the ground state (15.76 eV) than other molecules like CO_2, CO, or O_2, Ar^+ ions are less active than molecular ion species (CO_2^+, CO^+ or O_2^+). The rate of neutralization of Ar^+ ions is much slower than the molecular counterpart ions. Therefore, the time averaged concentration of Ar^+ ions is largest in the discharge. We have observed that, at the same discharge parameters, (e.g., power input, gas pressure and discharge gap) a discharge with a small fraction of Ar in CO_2, such as the MSG mixture, is much easier to generate and becomes more stable than in the case of pure CO_2.[2] Most reaction rate coefficients are compiled from various sources, and they generally have weak temperature dependence unless indicated otherwise. For strong temperature dependent reactions, the rate coefficients were taken at 400 K, which is the approximate gas temperature in the discharge.

---

[2] Water trace is present in the mixture, and its effect will be discussed later.

Consideration of all possible reactions is lengthy and even unnecessary. We have developed a discharge model that has utilized a simpler set of chemical gas kinetics but still carries almost the same degree of accuracy. The present kinetic model has focused on the dominant neutral species. We have neglected most of the reactions involving charged particles in the model due to the weak ionization (e.g., $N_+/N = N_e/N \sim 10^{-8}$-$10^{-9}$). Furthermore, some neutral reactions in the table have relatively low rate coefficients in comparison to the others; therefore, they can be neglected without any major effects. The dissociation for CO and N_2 has been neglected in the present model since their dissociation energies are much higher than those of the other major gas components like CO_2 and O_2.

The process that controls the dissociation of CO_2 in electrical discharge is the electron impact dissociation

$$e + CO_2 \rightarrow CO_2^* \rightarrow CO + O + e \qquad (a)$$

$$e + CO_2 \rightarrow CO + O^-. \qquad (b)$$

The reaction (a) is the primary dissociative channel and involves the electronic excitation of CO_2 with the threshold energy near 7 eV [11-12,28-29]. The second reaction (b), dissociative attachment, is another possible dissociative channel in the discharge. However, the cross section for this process is about two orders of magnitude smaller than the cross section for electronic excitation. Therefore, the dissociative attachment reaction can be neglected in this analysis. In addition, the contribution of vibrational excitation to the dissociation of CO_2 is still uncertain and therefore has not been considered here. Capezzuto et al [28] studied the influence of the vibrationally excited states on the dissociation of CO_2, and their results indicated an insignificant effect for gas pressures below 20 Torr, which is the case for the present discharge conditions.

The mechanism for CO_2 reformation is mainly associative detachment and oxidation of CO in MSG:

$$O^- + CO \rightarrow CO_2 + e \qquad (c)$$

$$O + CO \rightarrow CO_2 + h\nu \qquad (d)$$

$$O + CO + M \rightarrow CO_2 + M \ (M=CO_2) \qquad (e)$$

The rate coefficients for these reactions [30-32] are 7×10^{-10} cm^3/s, 2×10^{-20} cm^3/s, and 2.4×10^{-36} cm^6/s, respectively. The associative detachment reaction (c) is, therefore, the dominant reaction to reform CO_2. The inclusion of reactions (d) and (e) only changes the equilibrium gas composition by less than 5% percents. Hence, we will exclude the reactions (d) and (e) and include only the reaction (c) in the model as the main CO_2 reforming mechanism.

2.3.1 Gas Phase Reactions

We list the reactions that affect significantly the production and destruction of the neutral species in the gas kinetic model in Table I. The rate coefficients for these reactions either are calculated directly from the Boltzmann code or are compiled carefully from various literature sources.

TABLE I. List of major gas reactions in discharge of MSG mixture.

No.	Reaction	Rate Coefficient	Ref.
Dissociation			
R1	$e + CO_2 \rightarrow CO + O + e$	k_1=f(E/N)	present
R2	$e + O_2 \rightarrow 2O + e$	k_2=f(E/N)	present
R3	$e + O_3 \rightarrow O^- + O_2$	$k_3=1\times10^{-9}$ cm^3/s	present
Reformation			
R4	$O + O_3 \rightarrow 2O_2$	$k_4=4.6\times10^{-14}$ cm^3/s	[32, 34-35]
R5	$O + O + M \rightarrow O_2 + M$	$k_5=8\times10^{-33}$ cm^6/s (M=CO_2)	[32, 36]
R6	$O + O_2 + M \rightarrow O_3 + M$	$k_6=2.4\times10^{-34}$ cm^6/s (M=CO_2)	[35]
R7	$O^- + CO \rightarrow CO_2 + e$	$k_7=7\times10^{-10}$ cm^3/s	[32, 37]
R8	$O^- + O \rightarrow O_2 + e$	$k_8=2\times10^{-10}$ cm^3/s	[30, 38-40]
R9	$O^- + O_2 \rightarrow O_3 + e$	$k_9=1.0\times10^{-12}$ cm^3/s	[38-39]
R10	$CO + OH \rightarrow CO_2 + H$	$k_{10}=1.5\times10^{-13}$ cm^3/s	[31, 39-40]
R11	$O + OH \rightarrow O_2 + H$	$k_{11}=3.0\times10^{-11}$ cm^3/s	[31]

In the following section, the rate coefficients of reactions (R1) to (R9) will be discussed initially for the "water free" MSG model. Reactions (R10) and (R11) are included in the "extended model" to take into account the contamination of OH radicals.

The dissociation rate coefficients for reactions (R1) and (R2) are calculated using Eq. (6) and EEDF are obtained from the Boltzmann code described in Section 2.1. The cross section for the electron impact dissociation of CO_2 has a threshold of 7 eV. The electronic excitation cross sections for O_2 are the excited state $B^3\Sigma_u^-$ with a threshold of 8.4 eV and $A^3\Sigma_u^+$, $C^3\Delta_u$, and $c^1\Sigma_u^-$ with the threshold energies between 9.7 and 12.1 eV [24]. Byron and Apter [32] suggested additional contributions of 4.5 eV and 6.0 eV energy loss due to the dissociation rate of O_2 in the high current density discharge. In addition, following an argument similar to Byron and Apter, we multiply the O_2 dissociation rate by a factor two that accounts for O_2 dissociation by excitation transfer from N_2 and CO in the discharge. Eliasson and co-workers [41] used this excitation transfer to explain of the unexpectedly high ozone yield in the discharge of O_2/N_2. During the discharge, the electronically excited N_2 ($A^3\Sigma_u^+$ and $B^3\Pi_g$) is capable of transferring its energies to O_2 molecules and exciting them to the dissociation level (8.4 eV and 6.0 eV, energy loss). The same principal can be applied for the case of the electronically excited CO (a $^3\Pi$ and $a'^3\Sigma$). In other words, the additional excitation exchange processes involving N_2 and CO effectively increase the dissociation rate of O_2.

One of the critical reactions shown in Table I is the dissociation attachment of O_3, reaction (R3). It is the main source of negative atomic oxygen ions, O^-, which combine with CO to reform CO_2. The rate coefficient for reaction (R3) is somewhat controversial. Byron and Apter [32] suggested a large effective rate coefficient for the reaction that is ascribed as due to the vibrational excitation of ozone. Conversely, Leys et al. [40] proposed a value about three orders of magnitudes smaller for the rate coefficient of this reaction according to the negative ion densities from their Langmuir probe measurements. Running the model with these two extreme values, we obtained variations for the CO_2 dissociation level from 5 to 7%. In addition, by using the newest cross section of dissociative attachment of O_3 from Walker et al. [33] to compute the rate coefficient, with the help of the Eq. (6), we obtained a value for k_3 of about 10^{-9} cm^3/s, which is also in agreement with the rate deduced from the swarm experiment of

Stelman et al. [42]. Moreover, the variation of the CO_2 dissociation due to the uncertainty in the rate of the dissociative attachment of ozone is minimized further with the introduction of water contamination. In short, we found it reasonable to use the 10^{-9} cm^3/s value for the rate coefficient of dissociation attachment of ozone for the model.

The rate coefficients of reactions (R4) and (R6) are taken from the literature [32,34-36] at 400 K (approximating the discharge temperature in the present work), verified by the experiment described in Section 3. The associative detachment reaction (R7) is known as the main mechanism to reform CO_2. This reaction removes the negative ions O^- at a rate that is as fast as the rate at which they are created from the reaction (R3) even with a moderate amount of CO in the discharge. Therefore, the negative ions O^- play the role of the chain carriers during the discharge. The reactions (R8) and (R9) are also O^- removal reactions; however they contribute less than 5% of the gas variation compared to reaction (R7).

2.3.2 Rate Equations: Time Dependent and Steady State Model

The gas composition at every stage of the RF discharge of MSG could be obtained by solving a system of rate and mass conservation equations that are usually expressed in terms of the concentrations of species, rate coefficients, and stoichiometric coefficients [32]. In a time-dependent model, the system reduces to a combination of coupled differential and algebraic equations. Steady-state models are a set of algebraic equations.

The major elementary reactions in RF discharge of MSG are listed in Table I. Intermediate reactions, such as those involving electronically excited states including the metastable states, are neglected. Therefore, molecular and atomic species are assumed only to be in ground states. Based on the discussion in the previous section, the minimal system of rate and mass conservation equations is given by:

$$\frac{d[CO_2]}{dt} = -k_1 N_e [CO_2] + k_4 [O^-][CO] \tag{7}$$

$$\frac{d[O_3]}{dt} = \left(k_6[M][O] + k_9[O^-]\right)[O_2] - \left(k_3 N_e + k_4[O]\right)[O_3] \quad (8)$$

$$\frac{d[O]}{dt} = \left(k_1[CO_2] + 2k_2[O_2]\right)N_e - \left(k_4[O_3] + 2k_5[O][M] + k_6[O_2][M] + k_8[O^-]\right)[O] \quad (9)$$

$$\frac{d[O^-]}{dt} = k_3 N_e[O_3] - \left(k_7[CO] + k_8[O] + k_9[O_2]\right)[O^-] \quad (10)$$

$$[CO_2] + [CO] = [CO_2]_o \quad (11)$$

$$2[CO_2] + [CO] + [O] + 2[O_2] + 3[O_3] = 2[CO_2]_o \quad (12)$$

In Eq. (7) - (12), $[X]$ is the concentration of species X; k_n is the rate coefficient of the n^{th} reaction; $[CO_2]_o$ is the initial concentration of CO_2 in the MSG; M in the three-body reactions is taken to be equal to $[CO_2]_o$. Equations (11) and (12) represent approximately the mass conservation of carbon and oxygen atoms in the discharge. In the first equation, by ignoring the carbonaceous ions: $[CO_2^+]$, $[CO_3^+]$, $[CO_4^+]$, $[CO_3^-]$, and $[CO_4^-]$, which all have negligible number densities in comparison with their neutral counterparts, the total density of CO and CO_2 is always equal to the initial CO_2 in the mixture. Similarly, Eq. (12) represents the mass conservation of atomic oxygen in the discharge, neglecting the oxygen-containing ions. Note that even though the negative ions, O^-, have an active role in the production and loss of neutral species, their presence does not contribute by any significant amount to the mass conservation of oxygen in the discharge.

The steady state solution of the system was obtained by setting the time derivatives on the right hand sides of the Equations (7) - (10) equal to zero. The set of six nonlinear, coupled equations and six unknowns $[CO_2]$, $[CO]$, $[O_2]$, $[O_3]$, $[O]$, and $[O^-]$ can be solved numerically by iterative procedures, due to its fast convergence. Figure 8 shows the steady state solutions for Martian Simulant Gas in RF discharge as a function of the reduced field *E/N*. Since the rates of the dissociation of CO_2 and O_2 are dependent on the reduced electric field, *E/N*, the equilibrium of the neutral species also depends on the values of *E/N*. For the remainder of this work, we will use the notation k_{CO_2} and k_{O_2}, rather than k_1 and k_2, respectively.

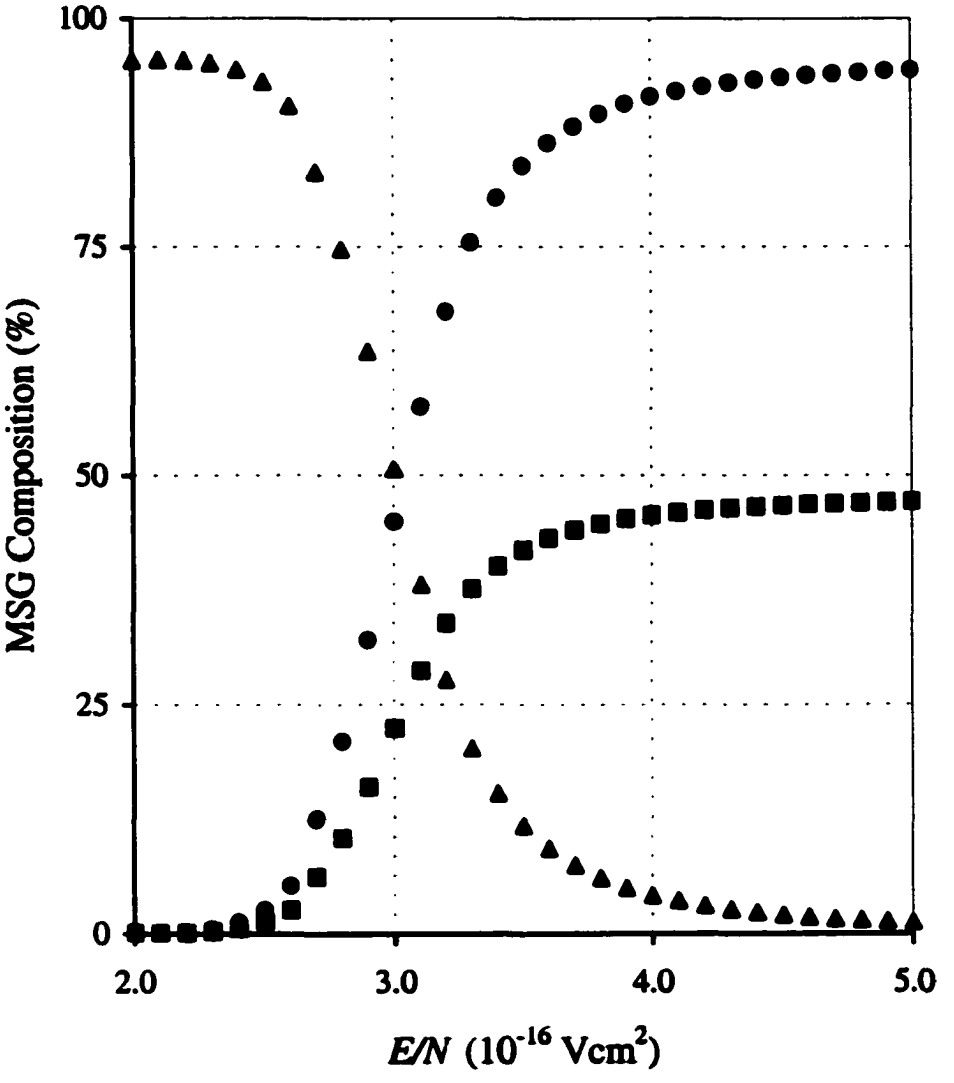

FIG. 8. Steady state composition of Martian Simulant Gas in RF discharge as a function of the reduced electric field, *E/N*: ▲, CO_2; ●, CO; ■, (O_2+O).

The time evolution of the neutral species concentrations in the mixture was computed using a 4th order Runge-Kutta method. Figure 9 describes the change of the gas constituents with time. About 80% of the CO_2 dissociation was achieved within five seconds. From the figure, the concentration of atomic oxygen reaches saturation much faster than that of the molecular oxygen and carbon monoxide molecules. However, the dissociation of CO_2 occurs more slowly. This indicates that any excessive production of atomic oxygen is immediately lost via recombination to form new oxygen molecules.

The time evolution calculation of the gas components in the mixture was performed with fixed dissociative rate coefficients for CO_2 and O_2, based on the initial MSG mixture. From Eq. (6) of Section 2.1, these rate coefficients were only computed from the high-energy fraction of the electron energy distribution function due to the threshold energies of the corresponding dissociative excitation cross sections. In addition, the result from Fig. 5 shows the high-energy fraction of the EEDF is smaller for the larger percentage of CO and O_2 in the MSG mixture. Therefore, the MSG mixture decomposes during discharge, resulting in smaller values of the EEDF and the dissociative rate coefficients of CO_2 and O_2 are smaller. The process of calculation of the time varying rate coefficients is as follows: Using the initial MSG mixture as the starting point (t = 0 sec), the EEDF and the corresponding rate coefficients were computed; then, a new MSG composition was determined at a selected time step. New EEDF and rate coefficients were computed subsequently. These rate coefficients then were used to compute a new MSG composition after each time step. The process was repeated until the MSG mixture achieved equilibrium.

The influence of time varying MSG concentrations on k_{CO_2} is shown in Fig. 10, where the concentrations were updated at time steps of 0.5, 1.0 and 2.0 sec. The results show minor differences within time dependent k_{CO_2} computing at these different time steps. The constant k_{CO_2} (not shown in the figure) is a straight line parallel with the x-axis and agrees with the time dependent k_{CO_2} at t = 0 sec. The results indicate that k_{CO_2} decreases with the discharge time. The rate of change of the time varying k_{CO_2} is most significant in the beginning of the MSG discharge. As the discharge reaches equilibrium

the time varying k_{CO_2} also reaches a constant minimum approximately one order of magnitude smaller than its initial value.

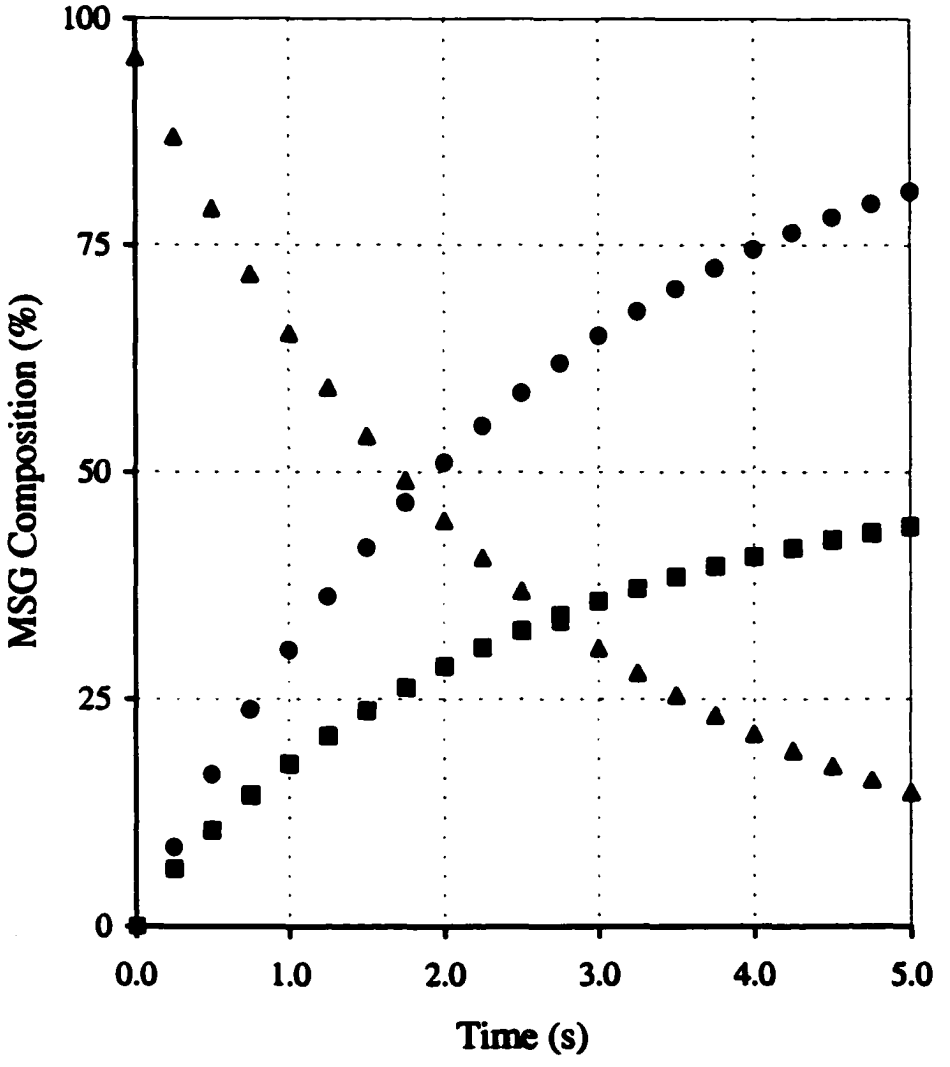

FIG. 9. Martian Simulant Gas composition in RF discharge at E/N=5.0×10^{-16} Vcm^2, p = 5 Torr, T = 400 K: ▲, CO_2; ●, CO; ■, (O_2+O).

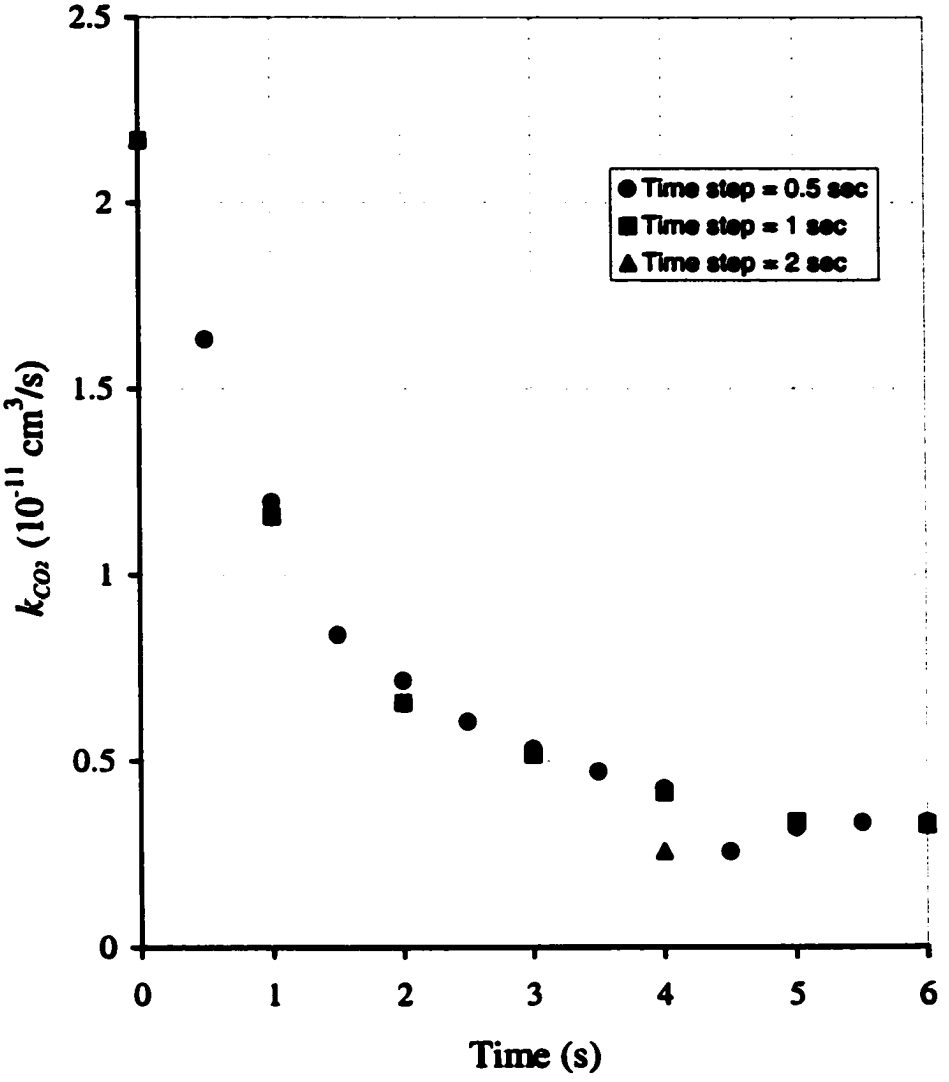

FIG. 10. Influence of mixture update times on the CO_2 dissociation rate coefficient, k_{CO_2}, during the discharge. Symbols indicate various time increments used in computation of gas composition.

The time dependent dissociation rate coefficients for CO_2 and O_2 increase the equilibrium time constant of the MSG mixture substantially in RF discharges. Since time varying rate coefficients are smaller than the initial fixed rate coefficients, the decomposition processes for the MSG mixture are slower. As a result, it reaches equilibrium more slowly. Figure 11 compares CO_2 time evolution in the MSG mixture during RF discharge with time varying and fixed rate coefficients. Over the same computation time (e.g., 6 sec), the percentage of CO_2 dissociation with time varying rate coefficients is about 10% less than the result with fixed rate coefficients. This is an interesting effect and could be an important feature for gas mixtures where the decomposition is more important. During the glow discharge, the rate coefficients are not constant and the rate of gas decomposition could be different.

In addition to the rate coefficients, the electron density is a key parameter that controls the rate of the gas kinetic processes in the RF discharge. The electron density, N_e, is proportional to the time average of RF power dissipated into the discharge, the magnitude of the applied electric field, and electron drift velocity [32],

$$N_e = \frac{\overline{P}}{eN(E/N)v_d} \tag{13}$$

where N is the gas number density; P is the power density; e is electrical charge; v_d is the electron drift velocity, and E/N is the reduced electric field. The bar represents the time averaged value. For typical discharge conditions, in the frequency interval between 20 and 50 MHz, and for pressures in the 5 to 10 Torr range, the relaxation time for electrons through momentum transfer collisions is much smaller than the period of the applied field. Therefore, electron transport coefficients behave as if they were in a constant electric field. The electron drift velocity varies instantaneously with the applied field, E, or the reduced field (E/N), and it can be obtained from steady state solutions of the Boltzmann code (see Eq. (5)). The time averaged power density and the gas density are determined from the experiment. For selected values of the reduced field (E/N), the electron densities can be obtained from expression (13).

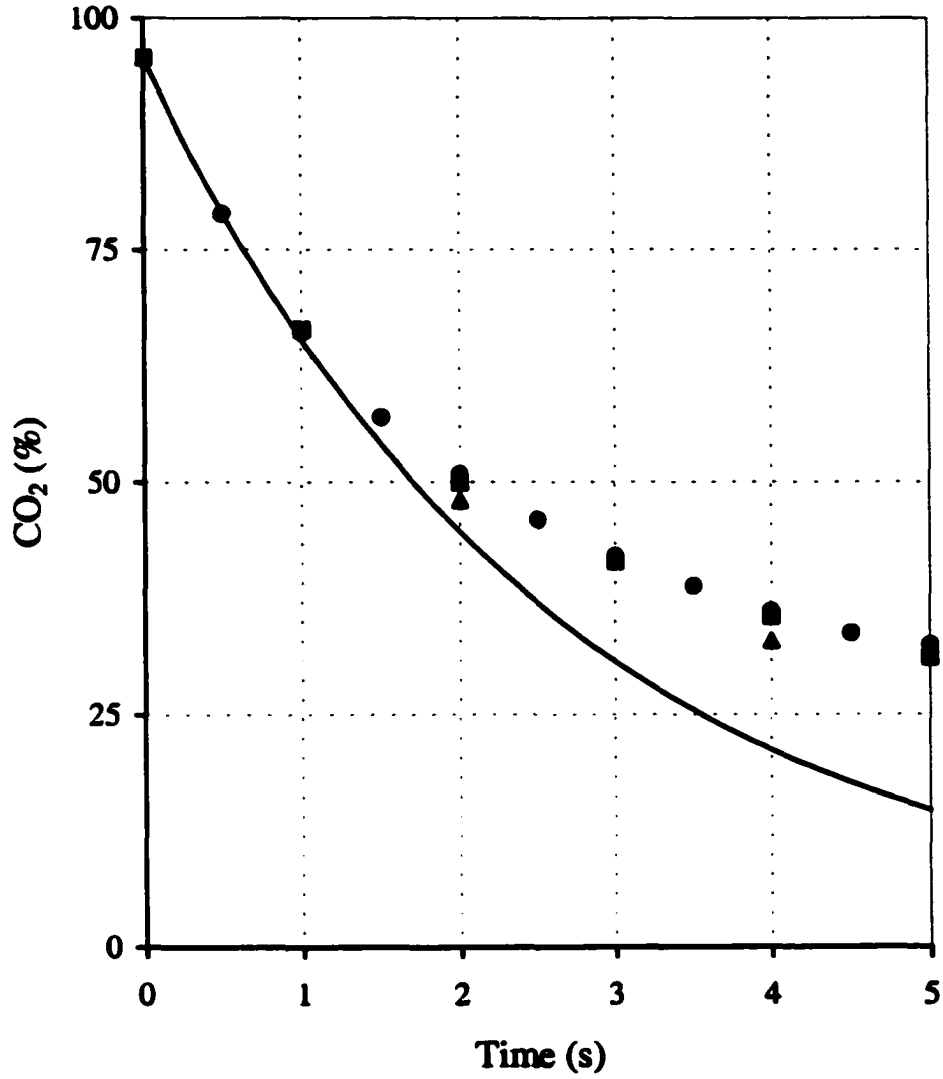

FIG. 11. Influence of time dependent discharge coefficients on CO_2 dissociation. Calculation was performed with k_{CO_2}: solid line, constant; ●, 0.5 time step; ■, 1.0 time step; ▲, 2.0 time step.

In order to see the effect of the electron density, N_e, on the dissociation of CO_2 in the mixture, we show in Fig. 12 the characteristic time of the dissociation of CO_2 as a function of electron density. The characteristic time is defined as the time when the natural logarithm of the ratio $[CO_2]_o/[CO_2]$ is equal to one where $[CO_2]_o$, and $[CO_2]$ are the CO_2 concentrations at the initial time and at time t, respectively. The characteristic time decays exponentially with increases in electron density. This indicates a strong dependence of electron density on all dissociation and recombination reactions during the discharge. As a result, the time for the gas to achieve its equilibrium composition depends largely on the values of electron density in the discharge.

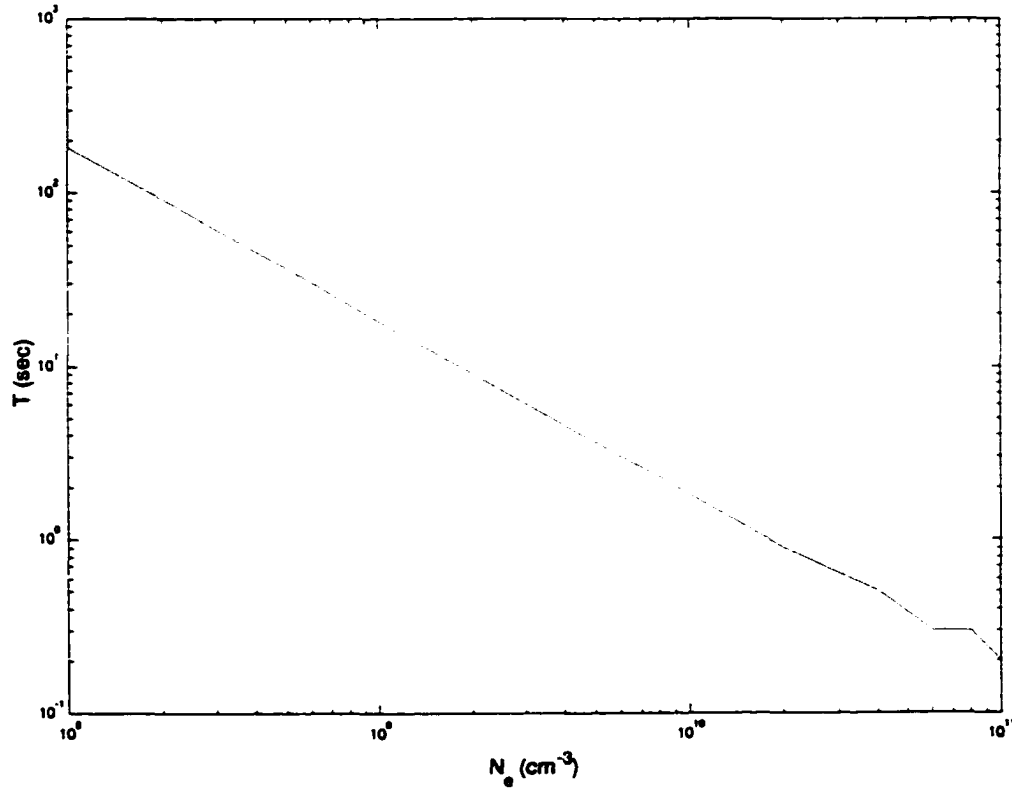

FIG. 12. Dependence of the characteristic time for CO_2 dissociation on electron density at E/N=5.0×10^{-16} Vcm^2.

2.3.3 Effect of OH Radicals

The OH radicals are effective in carbon dioxide reformation and oxygen recombination. In the previous discussion, the model assumed a water-free system and has excluded the reactions (R10) and (R11) in Table I. However, in a realistic conditions of the discharge, the trace of water is always present. The effect of OH radicals from contaminating water vapor is summarized in these reactions.

R10	$CO + OH \rightarrow CO_2 + H$	$k_{10}=1.5\times10^{-13}$ cm^3/s	[31, 39, 40]
R11	$O + OH \rightarrow O_2 + H$	$k_{11}=3.0\times10^{-11}$ cm^3/s	[35]

The first reaction has a direct negative effect on the CO_2 dissociation which is the reformation of CO_2. As pointed out by most CO_2 laser models, the water greatly reduces the dissociation level of CO_2 through the reaction (R10) by the recombination of OH with CO to reform CO_2. The generation rate of OH radicals by the dissociation of water molecules is relatively fast [40], $k = 10^{-9}$ cm^3/s. With an electron density of 10^{10} cm^{-3}, the concentration of OH radical is about 10% of the initial water concentration in the system. At a concentration of OH as small as 50 ppm in the discharge, the dissociation of CO_2 is limited to about 50% of its initial concentration while at the same discharge power, without the OH radical, the dissociation is nearly 100% (see Fig. 9 and Fig. 13). Therefore, we decided to include the reactions involving the OH radical in the simulation model. Results of this "expanded" model will be compared with experimental results in Section 3.

2.3.4 Negative Ions and Metastable Species

With the exception of the O^- ions that behave as intermediate species in the neutral reactions, we excluded the reactions involving other secondary negatively charged particles such as O_2^-, CO_3^-, and CO_4^- in this model. Their expected influence on the variation of the neutral gas composition was minimal. In addition, the influence of negatively charged particles on electron density was negligible due to the large quantity of CO that is present in the discharge. It was well known that in the CO_2 discharge, CO

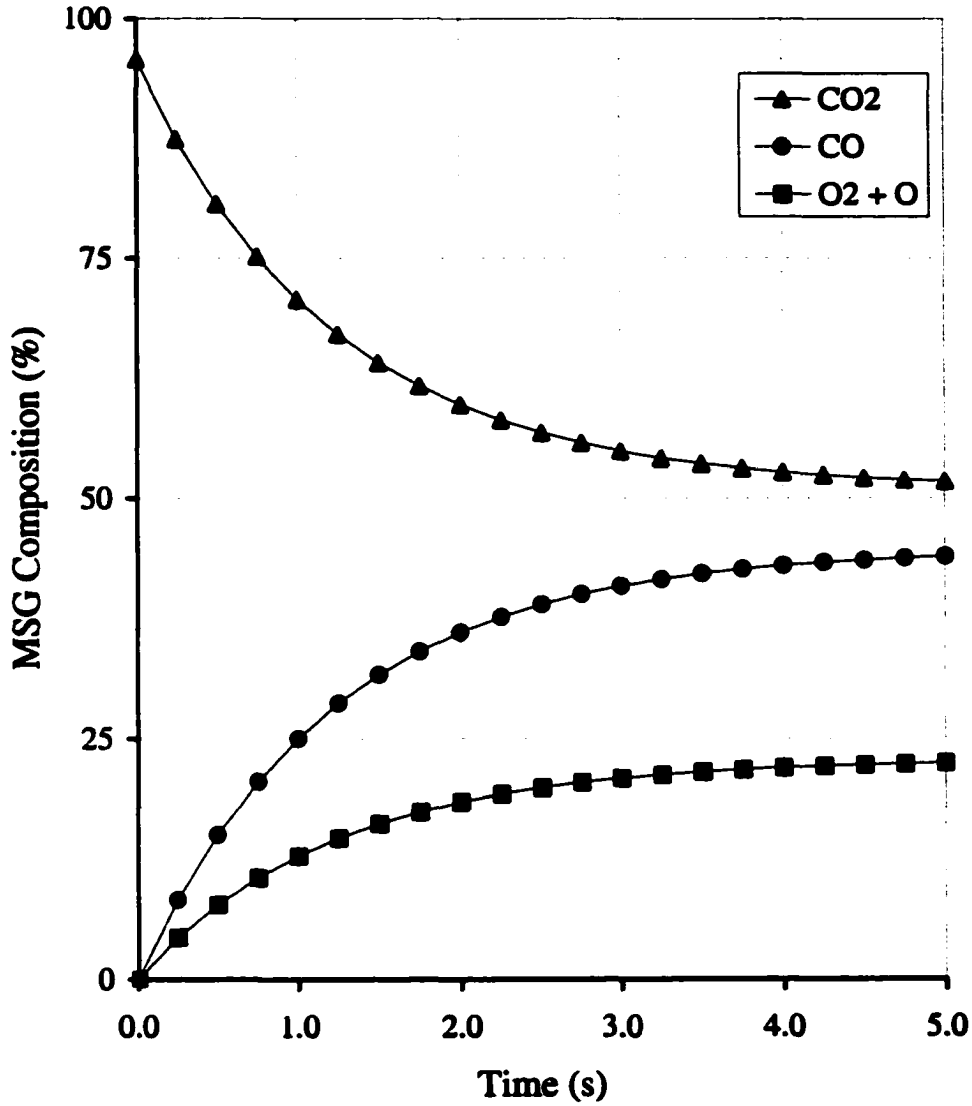

FIG. 13. Effect of on the variation of MSG composition with time in RF discharge. Data were calculated at E/N=5.0×10^{-16} Vcm^2, p = 5 Torr, T = 400 K, and *[OH]* = 50 ppm. The lines connect data points are used only to guide eyes.

is a very effective detachment species (see reaction (R7) in Table I). Hence, most of the dissociation attachment reactions will be balanced out by the associative attachment of CO. Nighan and Wiegand [38] pointed out that when the CO fractional concentration, $f = [CO]/([CO_2]+[CO]) \geq 0.1$ or, roughly, [CO] is larger than 10% of [CO_2], then the influence of other negative-ion processes can be neglected. In our discharge conditions, the CO concentration is typically larger than 50%, which is well beyond the level to consider the contribution of other negative ion reactions. In addition, applying the discharge conditions and running the model in steady-state with the production and loss of the negative ion reactions, the computed concentration of negative ions was about an order of magnitude less than the electron density. Therefore, we believe that other negative ion reactions have a negligible effect on the electron density and on the neutral gas composition.

Formation of metastable atomic oxygen O (^1D, ^1S) and molecular oxygen O_2 ($^1\Delta$) during discharge is an interesting phenomenon excluded from the gas kinetic discussion in the present model. Their concentrations in the discharge mixture can enhance the dissociation rate of the ground state O_2 ($X^3\Sigma^-$), and reduce the concentration of ground state atomic oxygen O (^3P) due to its high activation energy.

2.3.5 Influence of N_e on the CO_2 Equilibrium

In the dry (water-free) system, the variation of electron density affects not only the transient behavior but also the concentration of CO_2 at equilibrium. Since the main mechanism controlling CO_2 dissociation is electron impact, the rate of CO_2 dissociation is directly proportional to the electron density. This is equivalent to an increase in CO density. Meanwhile, the rate of production of ozone depends indirectly on electron density through reactions (R6) and (R9), as a result, the rate of production of O^-, which is necessary to combine with CO in order to reform CO_2, decreases. The characteristic time of dissociation for CO_2 is proportional to the variation of electron density on a logarithmic scale. The variation of N_e does not affect the transient rate of dissociation of CO_2, but it affects precisely the equilibrium concentration of CO_2.

2.4 Discharge Model

In a typical capacitive RF glow discharge, the value of the reduced electric field *E/N* is not a constant along the longitudinal axis. Assuming a uniform pressure and temperature within the discharge gap, *E/N* is directly proportional to the applied electric field, *E*. For a symmetric capacitive RF discharge, the absolute electric field, $|E|$, has a nearly parabolic shape with a minimum at the bulk plasma and a steep rise near the electrodes. The minimum of $|E|$ is due to the charge neutrality of the bulk, and the rise of $|E|$ is due to the space charge separation in the sheath region where positive ions are dominant. The quantitative model for the spatial distribution of the field E and the charge densities can be described by a set of continuity equations and an electrostatic equation [43]

$$\frac{\partial N_e}{\partial t}+\frac{\partial \Gamma_e}{\partial x}=\nu_i N_e-\beta N_e N_+, \quad \Gamma_e=-N_e\mu_e E \tag{14}$$

$$\frac{\partial N_+}{\partial t}+\frac{\partial \Gamma_+}{\partial x}=\nu_i N_e-\beta N_e N_+, \quad \Gamma_+=N_+\mu_+ E \tag{15}$$

$$\frac{\partial E}{\partial x}=\frac{e}{\varepsilon_o}(N_+-N_e) \tag{16}$$

where N, Γ, and μ are the density, flux and mobility of charged particles, respectively; the subscripts e and + stand for electrons and ions; ν_i is the ionization rate; β is the recombination rate; e is the electron charge; ε_o is the permittivity of free space.

In this model, two important assumptions were made that simplify the discharge description but preserve the main characteristics. First, the system is reduced to one dimension due to the symmetry of the discharge set-up, neglecting boundary effects. Second, the diffusion of charged particles to the walls is neglected.

In order to illustrate the main phenomenological characteristics of the discharge we need the spatial distribution of N_e, N_+, and E. These parameters and their transient behavior are more interesting in the present model. Therefore, we further simplify the system using the time averaged values of N_e, N_+, and E. This can be accomplished by integrating both sides of the above system of equations over one period of the applied

field with the assumption that the variation of these values over a period is negligible. Equations (14) to (16) can be rewritten as follows:

$$\mu_e E\frac{\partial N_e}{\partial x}+\mu_e N_e\frac{\partial E}{\partial x}+\alpha\mu_e N_e E-\beta N_e N_+=0 \tag{17}$$

$$\mu_+ E\frac{\partial N_+}{\partial x}+\mu_+ N_+\frac{\partial E}{\partial x}-\alpha\mu_e N_e E+\beta N_e N_+=0 \tag{18}$$

$$\frac{\partial E}{\partial x}=\frac{e}{\varepsilon_o}(N_+-N_e). \tag{19}$$

The ionization rate is approximated here by using the Townsend ionization coefficient, α, $\nu_i = \alpha\mu_e E$. This approximation of the ionization rate is valid for this type of discharge since the electrons perform drift-oscillation motions that resemble the case of a DC discharge (Section 2.2). For CO_2, the ionization coefficient is expressed by an empirically fitted formula suggested by Townsend: $\alpha/p = C_1 \exp(-C_2 p/E)$, where p is the gas pressure in Torr and E is electric field in Vcm^{-1}. The best fit for CO_2 ionization data at low E/p (e.g., $E/p < 20$ $Vcm^{-1}Torr^{-1}$) gave values for C_1 and C_2 of 0.1 $cm^{-1}Torr^{-1}$ and 20 $Vcm^{-1}Torr^{-1}$, respectively [45]. The approximate values for electron and ion mobility, μ_e and μ_+, in the present discharge, are $10^{-5}/p$ $Torrcm^2V^{-1}s^{-1}$ and $10^{-3}/p$ $Torrcm^2V^{-1}s^{-1}$, respectively and the recombination coefficient, β, is 10^{-7} cm^3s^{-1}. In addition, the model assumes a uniform temperature distribution along the gap, and therefore, uniform gas density, which means that the coefficients μ_e, μ_+ and β remain constant.

The symmetry of the discharge configuration can be further used to simplify the solution by applying boundary conditions at the center of the discharge. Quasi-neutrality of the bulk is one boundary condition (e.g., $N_e = N_+$). Another boundary condition is specified by the magnitude of the applied field E_o at the electrodes. In practice, the solution of the system of Eqs. (17) - (19) converges faster utilizing a trial and error value of E at the center of the discharge; however, the actual boundary condition E_o should be fixed in order to obtain consistent solutions. A more flexible boundary condition is specified by fixing potentials at the electrodes. This potential relates to E in terms of the integral of E over the discharge gap D. The above system of equations can be solved numerically with the 4th order Runge-Kutta method via backward integration from the discharge center to the electrodes. Since we are more

interested in reduced field values *E/N* than *E*, in the following section we will convert all results of *E* into *E/N* and take into account the variation of gas density *N* as a function of the pressure and temperature.

The reduced electric field *E/N* as a function of position along one half of the inter-electrode gap is shown in Fig. 14 at different bulk densities, N_e: (a), 1×10^9; (b), 5×10^9; and (c), 1×10^{10} cm^{-3}. The calculation is performed with a discharge gap of 0.5 cm at a pressure of 5.0 Torr, and temperature of 300 K. A fixed potential boundary was imposed in the calculation such that the total area under *E/N* was the same with a fixed *N*. Figure 14 illustrates important properties of this type of discharge. The reduced electric field has a minimum in the bulk plasma and a strong gradient close to the electrodes in the sheath region; furthermore, the field gradient increases with increasing bulk density. These properties are related directly to the sheath thickness and the Debye length λ_D, which is the quantity describing the charge separation in the plasma. The axial distribution of the electron densities along one half of the discharge gap is shown in Fig. 15 with the same discharge and boundary conditions as in Fig. 14. The axial distribution of the electron density decreases faster for the larger bulk density closer to the electrodes. Both figures 14 and 15 assumed the symmetry of *E* and N_e on the other half of the discharge gap.

Figures 14 and 15 show that the characteristic lengths, where the gradient of reduced electric field and electron density become significant, increase inversely with bulk densities. The first length is referred as the sheath thickness, and the other length is the Debye length, λ_D. In fact, they are proportional to each other, and the sheath thickness is approximately equivalent to 2-3 Debye lengths. From Fig. 14, the sheath thickness with $N_e = 1\times10^9$ cm^{-3} is estimated to be between 0.1 cm and 0.15 cm. To justify the estimation of the sheath thickness, we evaluated the value of the Debye length using the expression $\lambda_D \sim 743[(T_e/N_e)]^{1/2}$ where T_e is given in eV, and N_e in cm^{-3}. If we take the electron temperature $T_e = 4$ eV and the electron density, $N_e = 10^9$ cm^{-3}, then λ_D is about 0.05 cm. The sheath thickness is approximately equivalent to 2-3 Debye lengths. Therefore, we conclude that present model reasonably describes the sheath thickness.

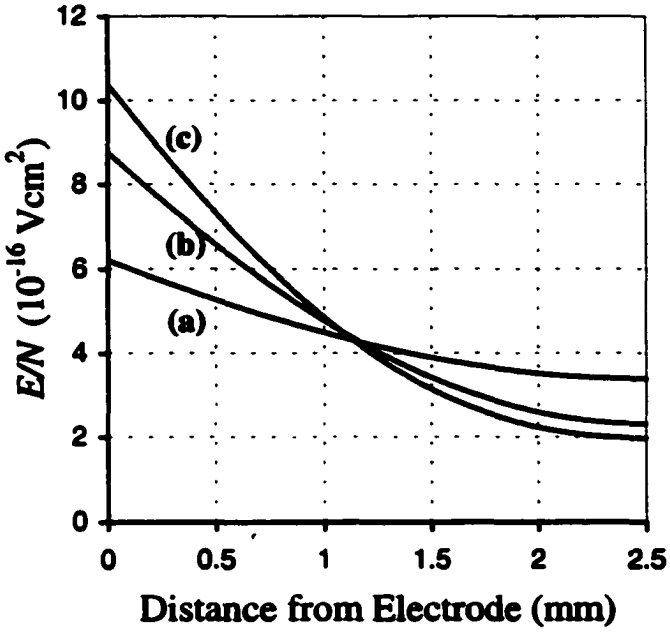

FIG. 14. Axial distribution of the reduced electric field along one half of the discharge gap at p = 5.0 Torr, T =300 K, and bulk densities: (a), 10^9; (b), 5×10^9; (c),10^{10} cm^{-3}.

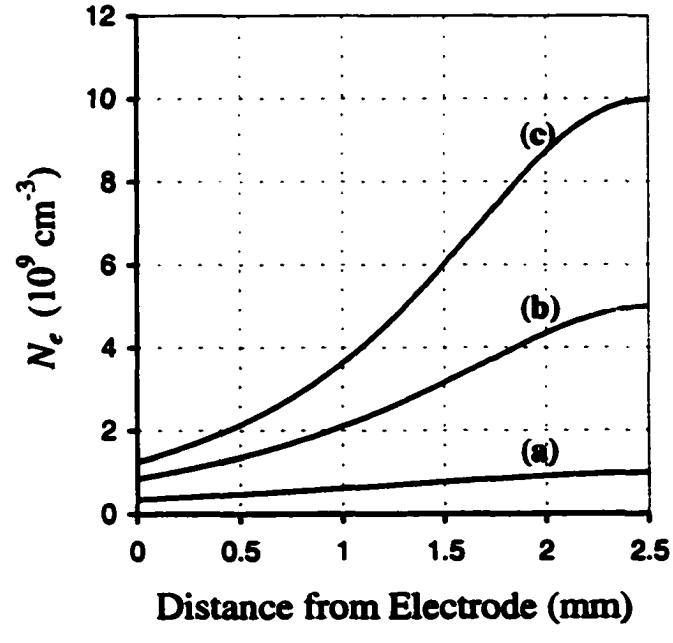

FIG. 15. Axial distribution of electron density along one half of the discharge gap at p = 5.0 Torr, T =300 K, and bulk densities: (a), 10^9; (b), 5×10^9; (c), 10^{10} cm^{-3}.

The axial distribution of the reduced electric field *E/N* is inversely proportional to the gas neutral density *N*. This implies *E/N* is proportional to gas temperature *T* and is inversely proportional to gas pressure *p*. However, the pressure dependence of *E/N* is not linear.

In Figure 16, *E/N* is calculated at pressures of 4 Torr, 5 Torr, and 6 Torr with $N_e = 5\times10^9$ cm^{-3} and $T = 300$ K. *E/N* decreases as pressures increases. Moreover, at lower pressures the slope of *E/N* becomes steeper near the electrodes and flatter at the discharge center. This is because *E/N* decreases inversely with increasing pressures not only because of larger neutral densities but also due to larger ionization coefficients, α. From the above relationship between ionization coefficients, with pressures and applied electric fields (see page 46), ionization rates increase significantly only when the exponential term in the Townsend ionization coefficient becomes less dominant, which is at higher applied field values (e.g., near electrodes).

The present model can be used to predict several important characteristics of this type of discharge. The reduced electric field *E/N* has a minimum at the center of discharge and increases exponentially to maxima at the electrodes. The electron density decreases from the center toward the electrodes. *E/N* decreases with increasing pressure.

The above model describes quantitatively the distribution of the field and charged particles within the discharge gap. In practice, the diffusion of charged particles, the presence of negative ions, and the non-uniform temperature distribution along the discharge gap have to be taken into account, making the calculation of *E* and N_e more complicated. In the present work, the quantitative values of *E/N* and N_e are accurate enough to examine their influence on chemical reactions during the discharge.

The rate of CO_2 dissociation depends on both the reduced field *E/N* and electron density N_e in the discharge. Since *E/N* is a fundamental parameter that controls the electron energy distribution, its variation affects electron transport parameters including the CO_2 dissociation rate by electron impact (Section 2.2). Therefore, an increase of *E/N* results in the increase of CO_2 dissociation. In addition, a decrease in N_e will reduce the number of CO_2 dissociation events (Section 2.3). In a typical RF discharge, as seen from the above model, these two parameters vary with opposite trends along the axis.

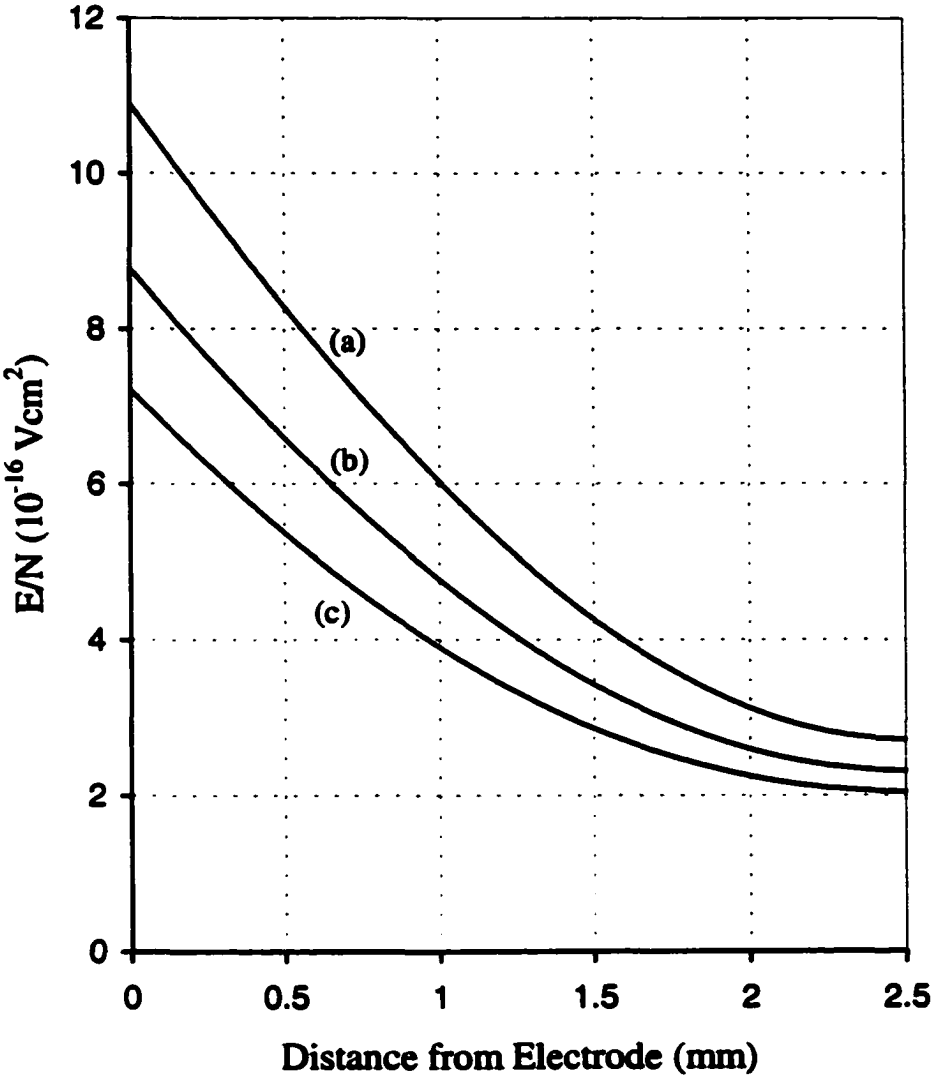

FIG. 16. Axial distribution of reduced electric field along one half of the discharge gap at $N_e = 5\times10^9$ cm^{-3}, $T = 300$ K, and various pressures: (a) 4 Torr, (b) 5 Torr, (c) 6 Torr.

E/N increases from a minimum at the center of the discharge to a maximum at the electrodes. On the other hand, N_e decreases from a maximum at the center to a minimum in the vicinity of electrodes. In order to see, tentatively, how the CO_2 dissociation rate changes with the variation of E and N_e along a discharge gap we plot the relative intensity of CO_2 as a function of position at a fixed discharge time in Fig. 17. The calculation was performed with several values of *E/N* taken from curve (b) in Fig. 14 and the corresponding values of N_e from curve (b) in Fig. 15. In addition, the calculation assumed a uniform temperature throughout the discharge gap, and therefore, a uniform gas density.

An important conclusion can be drawn from the diagram. The relative intensity of CO_2 is minimal near the electrodes and maximal in the bulk. This results because the dissociation rate is maximal near the electrodes where the reduced electric field is the strongest. However, the phenomenon can occur when the electron density gradient is small enough due to various conditions such as a larger plasma bulk density, higher temperature, or higher pressure near the electrodes.

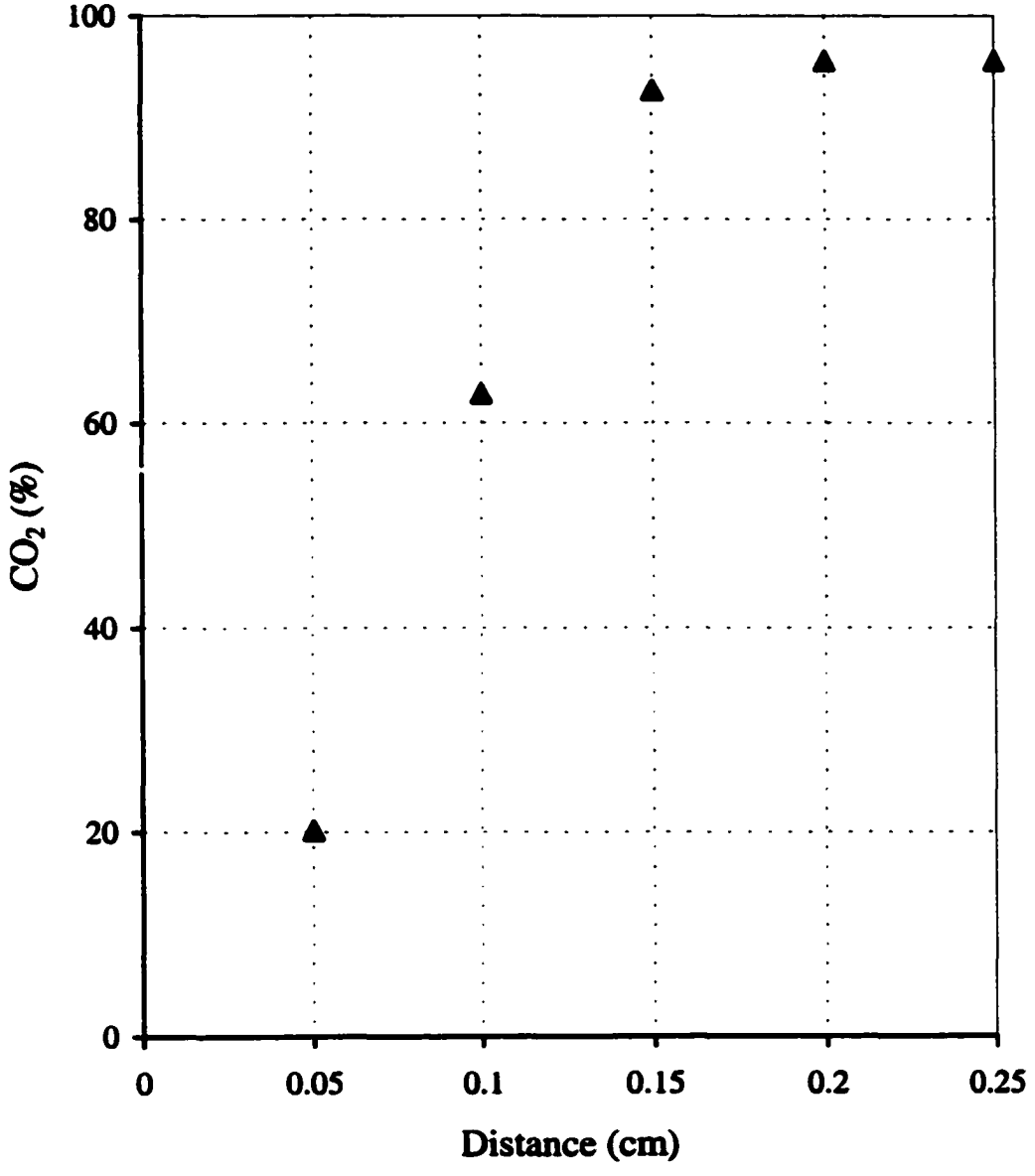

FIG. 17. **Axial distribution of CO_2 concentration along one half of the discharge gap at p = 5.0 Torr and T = 300K. One electrode is at 0 cm and the discharge center is at 0.25 cm.**

Section 3
EXPERIMENT

3.1 Experimental Apparatus

The RF system consists of a RF signal generator with an operational range of 1 kHz to 520 MHz (WaveTek 3006), an RF power amplifier with an operational range of up to 75 W over the frequency interval 9 KHz to 250 MHz (Dressler Alpha 250/75), a matching network, and a parallel plate electrode discharge chamber. The power amplifier had an output impedance of 50 Ω and all cables in the RF system were 50 Ω coaxial cables. The RF source was calibrated from 20 to 40 MHz with an oscilloscope at low power. The impedance matching of the discharge chamber was achieved using a T-type matching network with variable inductors and was monitored by using an in-line wattmeter (Bird, Model 43) to measure forward power P_f and reflected power P_r into and from the discharge chamber, respectively. Total input power is defined as $\Delta P = (P_f - P_r)$. The best impedance matching was determined from the smallest ratio of $\phi = P_r/P_f$, and the impedance of the discharge chamber was calculated based on a relationship of power ratio, ϕ, to standing wave ratio, s, in the following [44]:

$$s = \frac{1+|\Gamma|}{1-|\Gamma|} = \frac{1+\sqrt{\phi}}{1-\sqrt{\phi}}, \quad \Gamma = \frac{Z - Z_o}{Z + Z_o}. \tag{20}$$

Γ is called the reflection coefficient; Z_o, and Z are the impedance from the output power amplifier and discharge chamber, respectively. Z_o is always 50 Ω. The matching circuit is a T-type network with three inductor elements. The discharge is operated with an RF frequency from 20 MHz to 40 MHz and RF power from 1.0 W to 10.0 W. The RF generator and RF amplifier were isolated from commercial power using an isolation transformer.

The gas used in our experiments was Martian Simulant Gas (MSG) mixture at a research grade (99.99%) composed of 95.71% CO_2, 2.75% N_2 and 1.54% Ar.[2] The gas flow was regulated by a system of flow controllers including a step motor valve (Granville-Phillips, Model 201 Servo Driven Valve), a pressure flow controller (MKS 244), two capacitance manometer gauges to monitor chamber pressure (covering the pressure range 10^{-3} – 10^{3} Torr) (MKS 122A), and a pressure read-out (MKS PDR-C-2C). The gas composition resulting from the glow discharge was sampled by a Quadrupole mass spectrometer (UTI 100C) through a leak valve (Granville-Phillips) that was capable of sustaining a difference in pressure from 10 Torr in the discharge cell to 10^{-8} Torr in the QMS. The QMS is capable of scanning mass to charge ratios from 1 to 300 *m/e* at a resolution of unity. The scanning signal of the QMS could be recorded by a computer or sent directly to a X-Y recorder. The gas exhaust was pumped by a turbomolecular pump (Alcatel Drytel 31) with a pumping speed of about 450 l/min at N_2 pressures less than 1 Torr.

The discharge chamber was a standard 70.0 mm length stainless steel cube with a side entrance of 38.1 mm. The charge chamber was insulated electrically from the vacuum system by ceramic vacuum-sealed feedthroughs. The chamber was evacuated by a turbomolecular pump to a background pressure of 10^{-7} Torr. Electrodes were made from two stainless steel cylinders with diameters of 25.4 mm and lengths of 7.5 mm, mounted at the center of the chamber. One electrode was electrically grounded to the discharge chamber. The powered electrode was connected to the external RF source using an electrical feedthrough. The spacing between electrodes was varied using a linear motion controller attached to the ground electrode. The effective discharge volume was from 1.5 cm^3 to 5.0 cm^3. A small gas flow was maintained between the electrodes during discharge. Furthermore, after every measurement, a strong flush of fresh MSG was introduced through the discharge chamber as a means for cleaning the chamber. A general schematic of the experimental apparatus is shown in Fig. 18. In addition, for specific plasma diagnostic experiments (Section 3.2 and 3.3), the specific probes (Langmuir probes or thermocouples) were placed between the electrodes, and a monochromator was placed outside the chamber window.

---

[2] 100 ppm of OH radical was detected in the RF discharge of MSG.

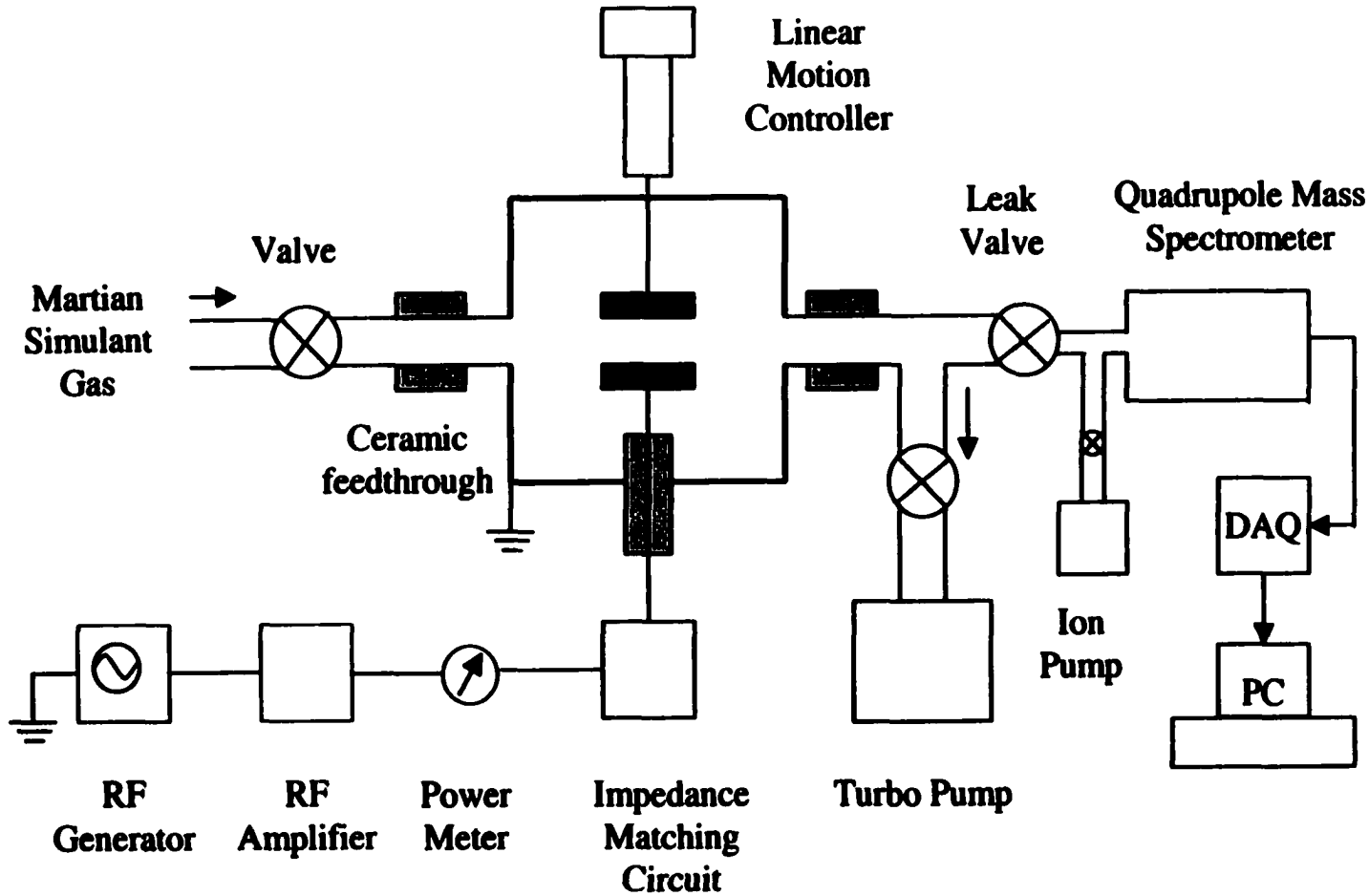

FIG. 18. Schematic of RF discharge in Martian Simulant Gas

3.2 Determination of Electron Temperature and Electron Density

3.2.1 Introduction to the Langmuir Probe Technique

The Langmuir probe is one of the earliest and most useful tools in plasma diagnostics. Langmuir probes are made of conducting material and they are inserted into plasmas while maintaining some applied positive or negative voltage to produce electronic or ionic current. The Langmuir probe experiment is constructed with a simple apparatus; however, the interpretation of Langmuir probe results is relatively complicated. We will not go into details of the theory of the Langmuir probe in this thesis, since it has already been explained and worked out in many textbooks [47-49]. We will summarize some of the most important features of Langmuir probe diagnostics, especially in the context of describing the operation of a double probe technique.

The double probe technique possesses a major advantage over the single probe method, namely the capability to measure plasma parameters, electron density N_e, and electron temperature T_e, in a high frequency discharge with a not well-defined reference electrode (e.g., in an electrodeless RF discharge).

Figure 19 shows the scheme of a double probe system. It consists of two cylindrical probes (P_1, P_2) that are placed around a point in the plasma with potential V_S. A polarity reversible potential, V, is applied between probes with P_1 more negative than P_2. Two sheath layers are formed at each probe with potentials V_1, V_2, respectively. In a general case, we assume a spatial plasma potential difference between the two probes, V_f, which is also the probe potential when the net current through the probes is zero. From the potential distribution of the double probe shown in Fig. 20, we have the following relationship:

$$V + V_2 = V_1 + V_f. \tag{21}$$

For the simplest case, where $V_f = 0$, the applied potential is equal to the potential difference between the two probes. Note that either probe potential cannot be positive with respect to the plasma potential. For any slightly positive change closer to the plasma potential, the system will immediately receive a large amount of electronic

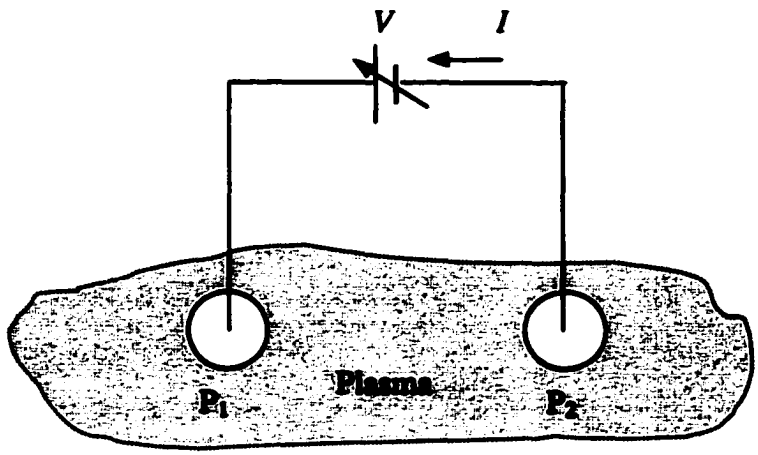

FIG. 19. Schematic of double probe system.

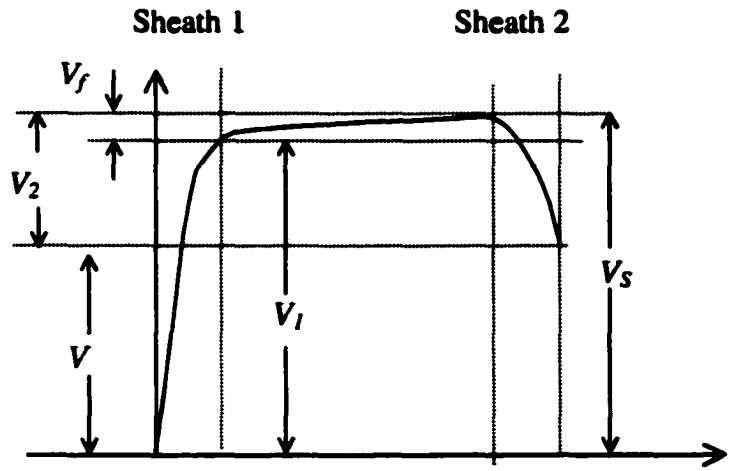

FIG. 20. Double probe potential characteristic.

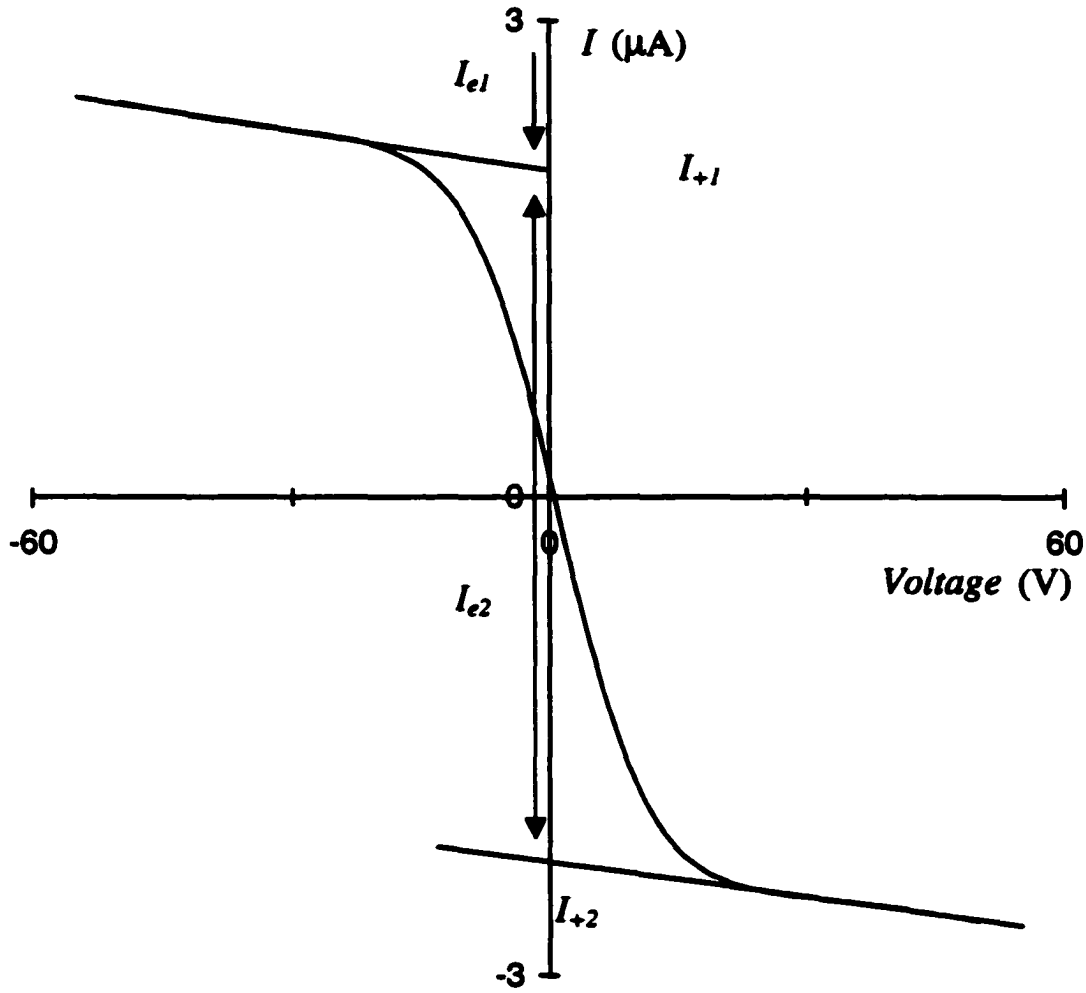

FIG. 21. Voltage current characteristic of symmetric double probe.

saturation current. This happens because the electron temperature is much higher than the ion temperature.

Another important feature of double probes is the "floating" condition of the system, since the total current flowing through the system is always equal to the sum of electron and ion currents. Let I_e and I_+ be the magnitudes of the electronic and ionic currents to each probe. Take the positive sign as for the positive current, then the total current, or the measured current, is expressed as:

$$I = I_{+1} - I_{e1} = -(I_{+2} - I_{e2}) \tag{22}$$

or

$$I_{+1} + I_{+2} = I_{e1} + I_{e2}. \tag{23}$$

If the potential of one probe is much more negative than the other (e.g., $|V| >> 0$), the ion current to this probe is dominant, and the electron current to the probe is nearly zero. Furthermore, the ion current to the probe reaches saturation and depends weakly on V. When the potential difference between probes is small, the ion current is compensated by the electron current where the latter depends strongly on V since the number of electrons reaching the probe is proportional to an exponential of probe potential V (e.g., $N_e \sim N_o exp(-eV/kT_e)$. The closer V approaches zero, the more strongly I depends on electron current. Therefore, by varying the potential applied to the double probe, different values of currents can be obtained. A typical current-voltage characteristic curve for a symmetric double probe is shown in Fig. 21.

Plasma parameters, such as average electron temperature, electron density, and local electric field can be extracted from the V-I characteristic curve of the double probe. If the probes are identical (same shape and area) and are positioned on an equipotential surface (in the present case, that is a plane perpendicular to the discharge axis), a simple formula is derived to measure the average electron temperature [45]:

$$\frac{I_{+1}}{T_e} = \frac{dI_{+1}}{dV_1} - 2\frac{dI}{dV}. \tag{24}$$

I_{+1} is the ion saturation current and it is usually found by extrapolating the gradual slope part of the I-V characteristic curve; T_e is the mean electron temperature, expressed in Volts; dI_{+1}/dV_1 is assumed equal to dI_{+1}/dV, the gradual slope of the curve; dI/dV is the slope of total current at the symmetry point O. In the case of an ideal double probe system, the I-V curve has a flat ionic saturation current at a very large $|V|$. As a result,

dI_+/dV is equal to zero. In practice, this term is non-negligible due to the small area of the probe and the effect of energetic ions that keep impinging on the probes.

Electron density can be derived from ionic saturation current. The detailed theory is rather complicated. Here we present only a summary of the explanation given in Ref. [47-49]. When a probe is applied with a negative potential V, the probe is attractive to positive charges and repulsive to most of the electrons. The probe is surrounded by a layer of positive charges (sheath) that defines the maximum number of ions able to reach the probe surface or the ion saturation current. In addition, there is an intermediary layer or pre-layer between the non-perturbed plasma and the sheath layer surrounding the probes. In the pre-sheath, the ions under the influence of the negative probe potential, V, gain additional velocity that is comparable to the thermal electron temperature T_e and can be approximated as follows:

$$v_+ \approx \sqrt{\frac{2e|V|}{M}} \approx \sqrt{\frac{2kT_e}{M}} = \sqrt{2}v_B, \text{ where } v_B = \sqrt{\frac{kT_e}{M}} \tag{25}$$

where e is the ion charge; k is the Boltzmann constant; M is the ion mass, and v_B is called the Bohm velocity. Moreover, the quasi-neutrality condition is still maintained in the pre-sheath as in the non-perturbed plasma region, where ion density is the same as electron density. According to their theory, the electron density in the pre-sheath is approximately equal to $N_e/\bar{e}$, where N_e is electron density in the non-perturbed plasma region, and $\bar{e}$ is the base of natural logarithms. Therefore, the ion saturation current is then equal to

$$I_+ = Aen_+v_+ \approx \frac{\sqrt{2}}{\bar{e}} AeN_e\sqrt{\frac{kT_e}{M}} \tag{26}$$

where A is the area of the probe; T_e is the electron temperature. Therefore, the electron density, N_e, can be found if the ion saturation current and electron temperature are known.

If double probes are placed in a non-equipotential surface (e.g., along the discharge axis), the spatial plasma potential is not zero. Then the local electric field can be found by measuring the floating potential where the total current vanishes and by knowing the distance between the two probes. The local electric field is then $E = \Delta V/\Delta x$. Note that in the non-equipotential measurement, we cannot measure the plasma

potential, V_S; we only measure the potential difference between probes, which gives the average electric field in the region.

In short, by analyzing the I-V characteristics obtained from experiments in the discharge plasma based on the Langmuir probe theory (see Eqs. (24) and (26)), we can extract crucial plasma parameters such as average electron temperature and electron density. In addition to the floating advantage of a double probe system, which does not need a well-defined reference electrode, the double probe can also be used to measure the local electric field in the plasma.

3.2.2 Experimental Set-up

Two identical cylindrical probes were prepared for the Langmuir probe experiment. The probes were polished carefully and cleaned thoroughly in an Ultrasonic cleaner to prevent any contamination to the discharge from surfaces of the probes. The tips of the probes were made of 99.9% pure Tungsten with very high anti-corrosion properties and resistance to the electron bombardment during discharge. Each probe had a diameter of 0.4 mm and a length of 4.0 mm exposed to the discharge. The distance between probes could be adjusted from 0.5 mm to 2.5 mm, depending on the requirements of the experiment. The rest of the probe was insulated in a double-pore ceramic sleeve to prevent any unwanted charge collection at the discharge edge. Probes were positioned in two positions: (1) on a plane perpendicular to the discharge axis, or (2) on a plane parallel to the discharge axis. In the first configuration, the plasma potential difference between the probes was nearly zero, and the analysis of the I-V characteristic curve could be simplified due to the symmetry of the probe position. In the second configuration, the local electric field could be obtained based on the ratio of plasma potential difference to the probe separation distance.

The probes were spot-welded to two electrical feedthroughs connected to an external circuit. The power supply circuit was a series of batteries applied to probes at a constant and stable potential (they varied by 1% in five hours) with a maximum of ±50.0

V. The batteries were used in attempting to minimize the influence of RF noise during measurements. The applied potential increment could be as small as 1.0 mV by using a

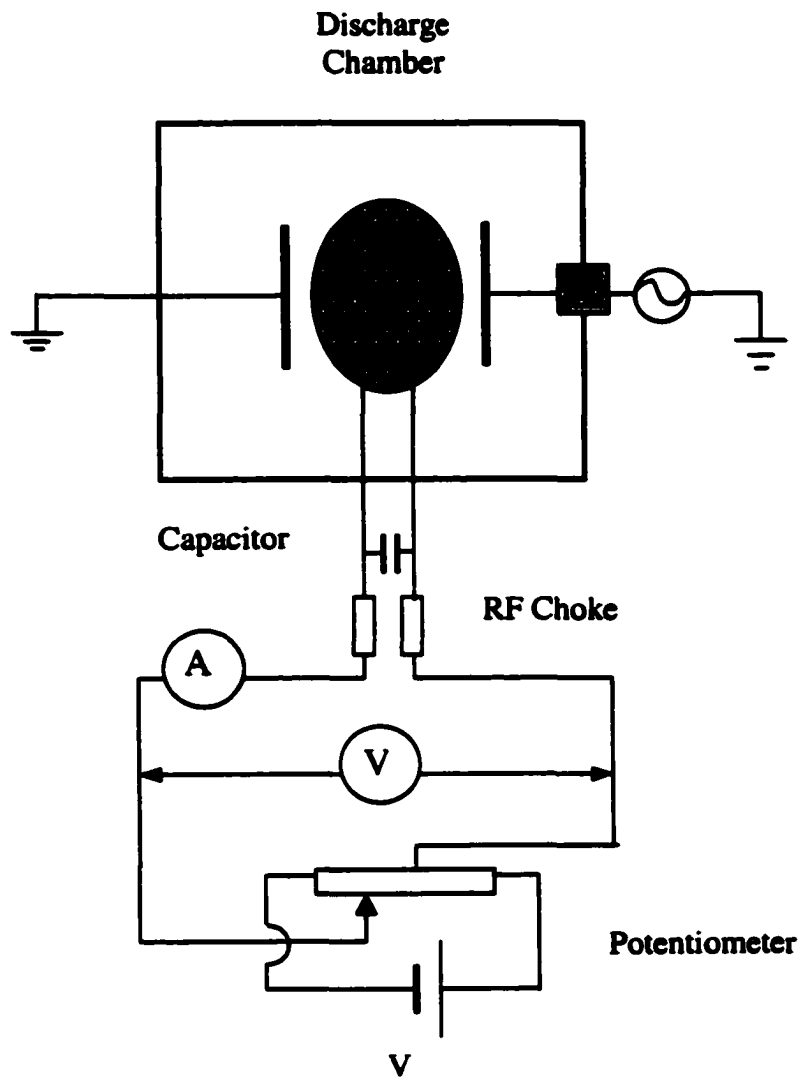

FIG. 22. Schematic of Langmuir probe experiment.

high precision 100 KΩ potentiometer. The probe voltage was measured using an electrometer with a very high input impedance, so that the leakage current through the meter was much smaller than the measured probe current. An ammeter, capable of measuring current in the microampere range was employed. In addition, an RF filter circuit, including a capacitor and inductors, was inserted between the power supply circuit and the probes to eliminate the effect of RF noise across the probes and the external circuit. During discharge, a reversible voltage was applied between the probes, and probe currents were measured corresponding to each value of the applied voltage. A schematic of Langmuir probe circuit and probe tips was shown in Fig. 22 and Fig. 23.

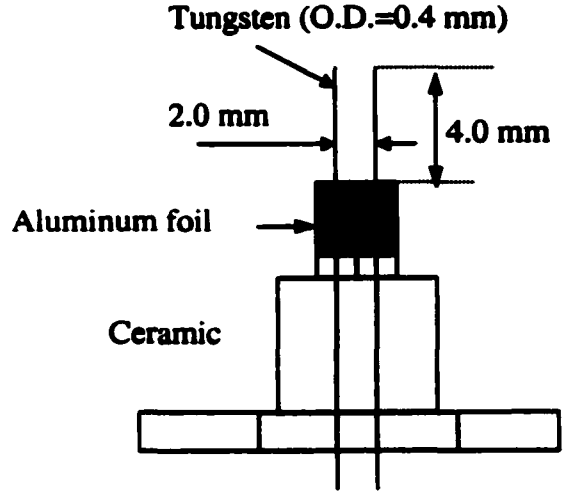

FIG. 23. Tips of Langmuir probes.

3.2.3 Langmuir Probe Results and Discussion

In the first series of measurements, the characteristic electron temperature was determined. The probes were placed at the center of the discharge and in the same plasma potential surface, which was perpendicular to the electrode transverse axis. The electron temperature was assumed isotropic along the radial axis of the plane. Electron temperatures were measured at two different pressures p = 3.0 Torr and 5.0 Torr, and three different discharge gaps, D = 6.5 mm, 8.0 mm and 10.0 mm. A typical measured I-V characteristic is shown in Fig. 24 at the discharge power of 1.0 W, p = 5.0 Torr, and D =6.5 mm. The clear symmetry of the characteristic curve with respect to zero implied that the probes were placed in the same potential surface of discharge. However, a slight difference in the top and bottom ion saturation currents indicated that the probe areas were not exactly the same. Furthermore, the slopes of the ion saturation were not completely flat which normally happens in the small probe case. This will add a small error to the electron density analysis that we will discuss later.

In Fig. 25, we plot the mean electron temperatures as a function of discharge power density, which we defined roughly as the ratio of average input power to discharge volume (product of the electrode area and the electrode separation distance). The increase of discharge power density could be achieved via an increase in power at a fixed discharge gap or by decreasing the discharge gap at a fixed input power. The electron temperature was observed to increase linearly with power density at both discharge pressures. In fact, electron temperature was observed to increase with input power independently. This can be easily understood as follows. Electrons are driven by an applied electric field, and they collide randomly with molecules. Mean electron temperature, T_e, is proportional to the square of the electron average drift velocity, which depends on the driving field E. Any increase in power density will result in an increase in field magnitude, and therefore, the increase in T_e. In fact, T_e is linearly proportional to the reduced electric field E/N at most conditions of interest here. In order to verify this, we fixed the power density, and measured T_e at two discharge pressures, p = 3.0 Torr and 5.0 Torr. T_e was found to be inversely proportional to pressure at the same power density. At higher pressure, which is equivalent to increased gas density N, T_e assumed

a smaller value. This is a strong indication of the dependence of T_e on the reduced electric field *E/N*.

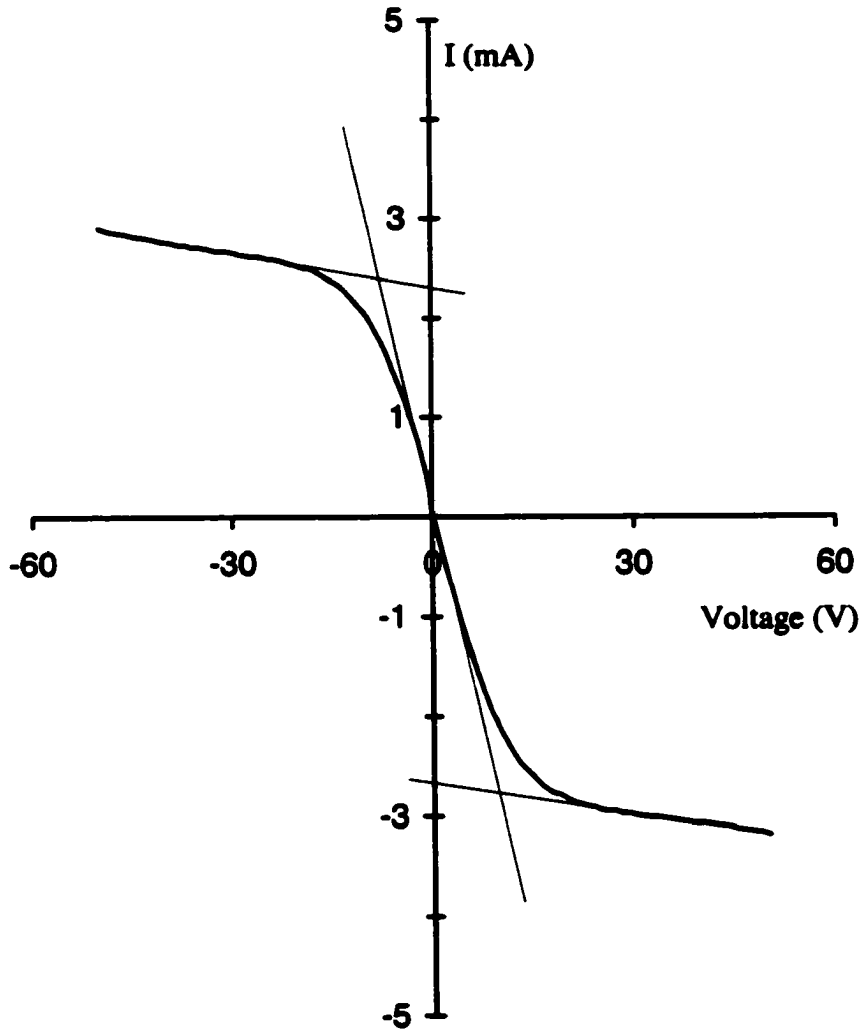

FIG. 24. I-V Characteristic measurement of discharge at P = 1.0 W, p = 5.0 Torr, D = 6.5 mm.

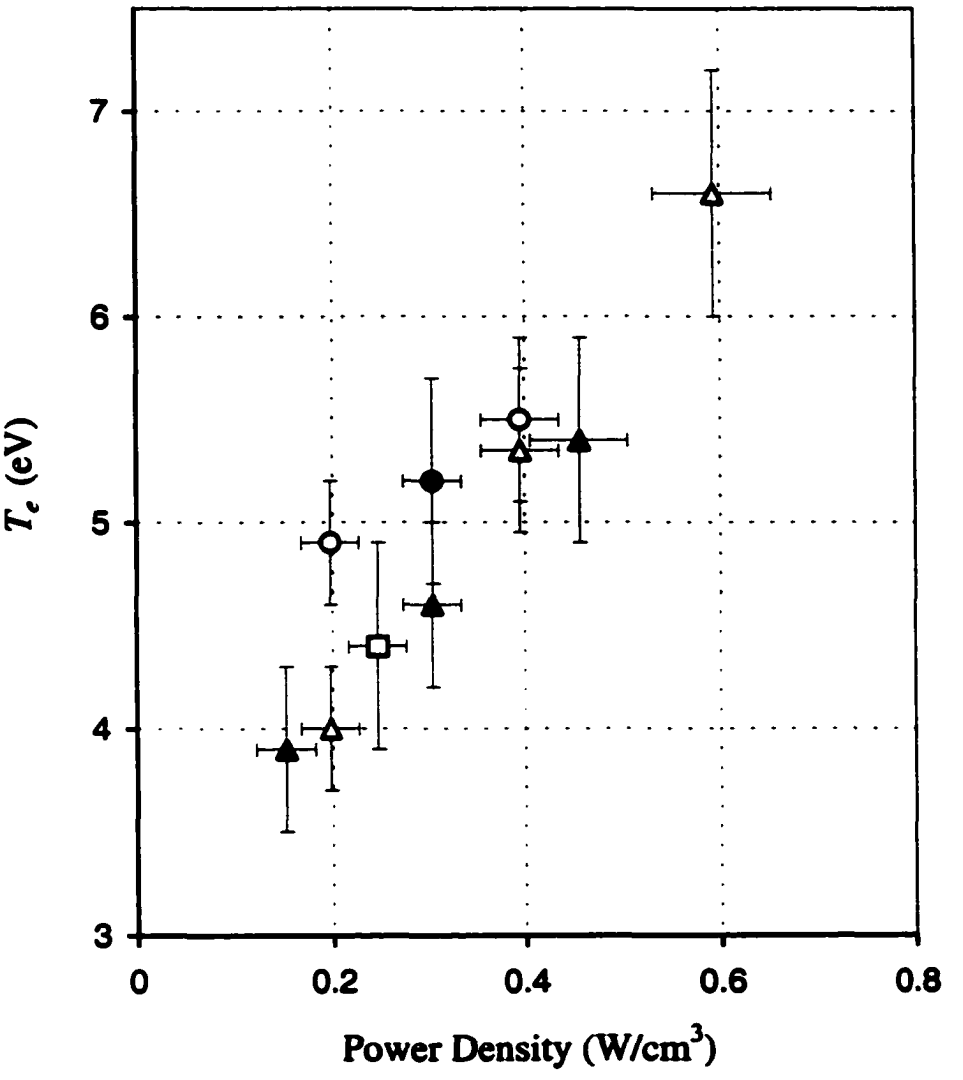

FIG. 25. Electron temperature as a function of power density at various discharge conditions: ●, p = 3 Torr and D = 6.5 mm; ○, p = 3 Torr and D = 10.0 mm; ▲, p = 5 Torr and D = 6.5 mm; △, p = 5 Torr and D = 10.0 mm; □, p = 5.0 Torr and D = 8.0 mm.

The electron temperature determined by the Langmuir double probe method has shown a strong linear proportionality to the reduced electric field with increasing power, decreasing discharge gap or decreasing pressure. These data exhibit a result consistent with our previous calculations of the electron temperature from the kinetic equations in Section 2.1 (see Fig. 6) where T_e increased linearly with reduced electric field E/N. The y-axis error bars are the experimental standard deviations (e.g., the root-mean-square deviation) from the mean value ($y = y_{ave} \pm \sigma$, $\sigma = [(\Sigma(y_i-y_{ave})^2/n]^{1/2}$, where n is the numbers of measurements). The x-axis error bars are due to the uncertainty in the power measurements, which is proportional to the input power.

The electron density was evaluated based on electron temperature and ion saturation current measured with the double probe system using Eq. (26). The ions attracted to the probes are assumed to be Ar^+, since this species is present in the MSG discharge and Ar^+ is more stable than other ions. The dependence of N_e on E/N is not obvious, since N_e is inversely proportional to the square root of T_e and is directly proportional to I_+. Moreover, N_e has shown a weak dependence on T_e and a strong dependence on I_+. This is implied from the interpretation given in Section 3.2.1, where the ion density in the pre-sheath layer was assumed proportional to the bulk electron density. The electron density is plotted as a function of power density for various discharge conditions in Fig. 26. N_e exhibits an exponential dependence on power similar to the T_e trend. This effect can be explained as follows. As the power density rises, the mean electron temperature increases. More electrons are capable of ionizing atoms or molecules. Therefore, an increase in power density will result in an increase in electron density within the bulk. As an exception, there is a dip in electron density at the value of power density of 0.3 W/cm^3 at p = 3.0 Torr. The cause of the dip is presently unknown. Experimental error cannot be excluded, as seen by the range of error bars on the diagrams. The y-axis error bars are the statistical errors and the x-error bars are the uncertainty in power measurement as explained in the previous paragraph. The dependence of N_e on discharge pressure has characteristics similar to T_e. A pressure increase from 3.0 Torr to 5.0 Torr results in a slight loss of N_e. This is probably due to the decrease in the electron mean free path with pressure. Note that there are two separated patterns of electron densities at 5.0 Torr that correspond to different discharge

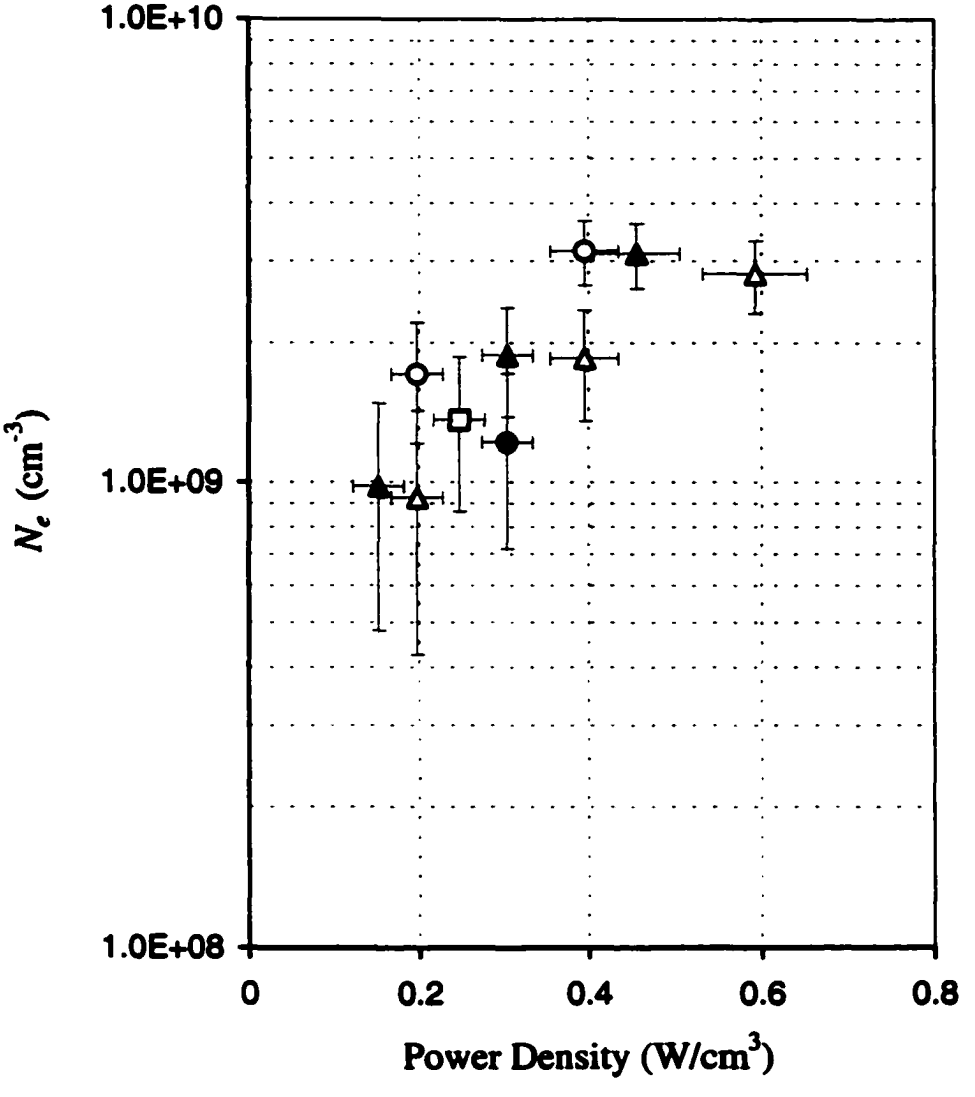

FIG. 26. Electron density as a function of power density at various discharge conditions: ●, p = 3 Torr and D = 6.5 mm; ○, p = 3 Torr and D = 10.0 mm; ▲, p = 5 Torr and D = 6.5 mm; △, p =5 Torr and D = 10.0 mm; □, p = 5.0 Torr and D = 8.0 mm.

gaps, D = 6.5 mm and D = 10.0 mm, with a slightly higher shift in N_e for the smaller discharge gap. The decrease in power density does not agree linearly with the increase of the discharge gap, possibly indicating a nonlinear relationship between the power density and the discharge gap. The effect is due to the sheath formation at electrodes. The interpretation is rather complicated, and more experiments are needed. Since the effect is not strong, we have assumed a uniform power distribution throughout the discharge gap.

Figures 27 and 28 display the electron temperature and electron density dependence on power density at different gas flow rates. The measurements were performed at pressure of 5.0 Torr and a discharge gap distance of 6.5 mm. Similar to previous results, T_e is linearly proportional to power density and N_e is exponentially proportional to power density at various gas flow rates F. There is no significant variation in N_e with flow rates, and the dependence of T_e on the flow rate is not obvious. However, it is noted that a slight variation in T_e is observed at low F. This is probably due to the additional presence of gas dissociation products such as CO, O_2, and O during the discharge. At low flow rates, CO_2 molecules have a longer dwell time, and more CO_2 molecules dissociate into CO, O_2. These additional molecules are known to remove "tail" electron energy from the EEDF due to their large rotational excitation cross sections. As a result, the mean electron temperature is smaller for longer dwell times, or the slower flow rates.

The axial distributions of electron temperature and electron density along the transverse axis were also investigated. The measurements were performed with a double Langmuir probe placed on an equipotential plasma surface (parallel with the electrodes) and moved along the transverse axis while the power, pressure, and discharge gap were maintained at 0.3 W, 5.0 Torr and 6.5 mm, respectively. The results are shown in Fig. 29 and Fig. 30. Both figures illustrate the maximum of electron energy and density obtained near the center of the discharge. Measurements near electrodes are affected by two different electron sources. The primary electron source is from the plasma bulk. The electrons are attracted toward the electrodes during a half period of low RF potential. They experience multi-inelastic collisions with ions or neutral molecules in the region and lose most of their energy near the electrodes. Another electron source is

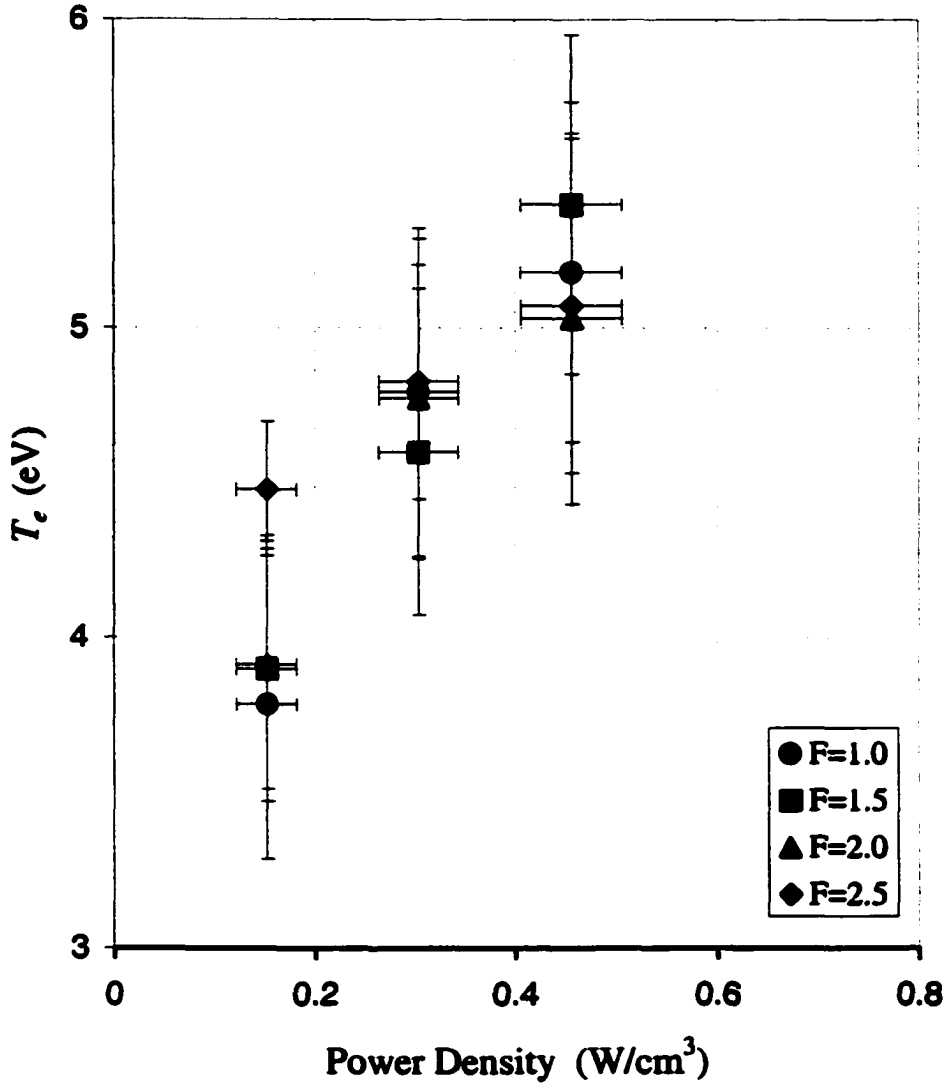

FIG. 27. Electron temperature as a function of power density at various gas flow rates, F (cm^3/s).

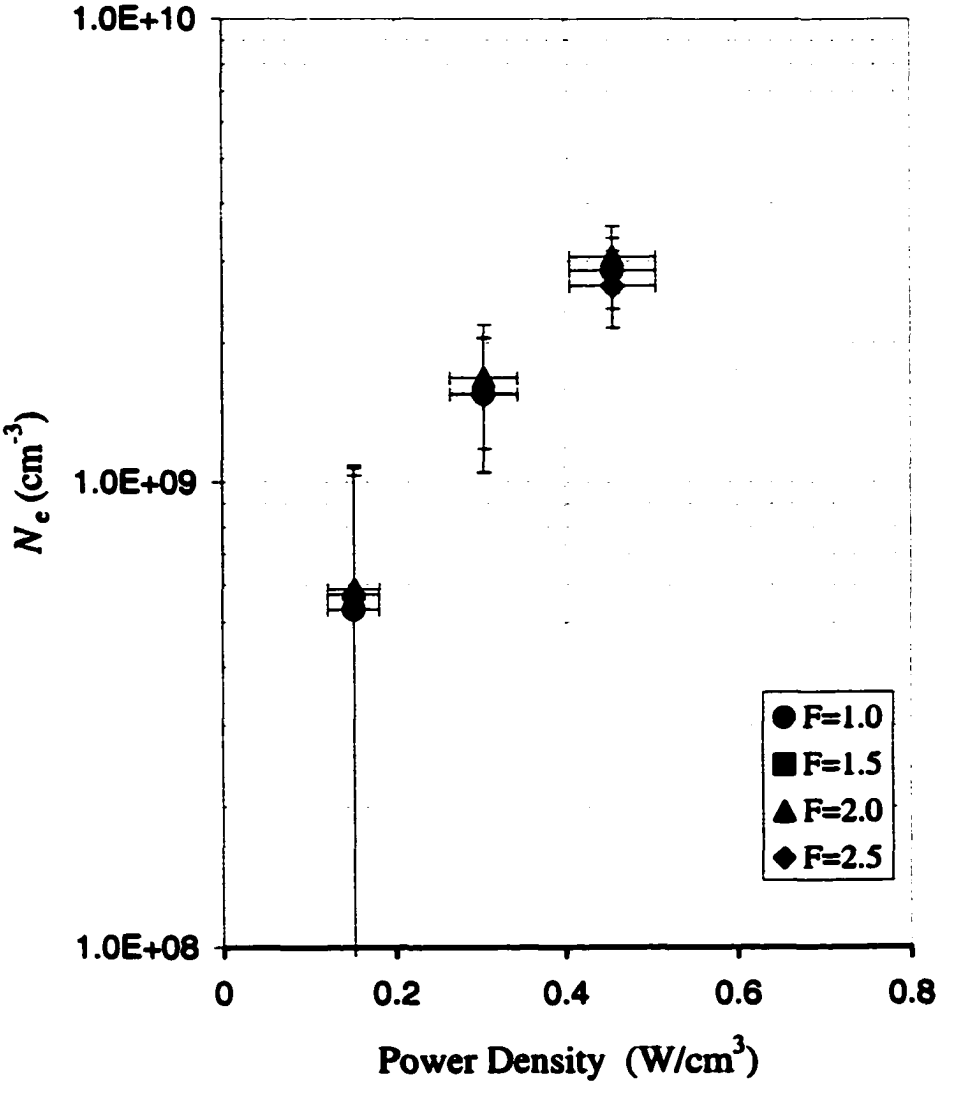

FIG. 28. Electron density as a function of power density at various gas flow rates, F (cm^3/s).

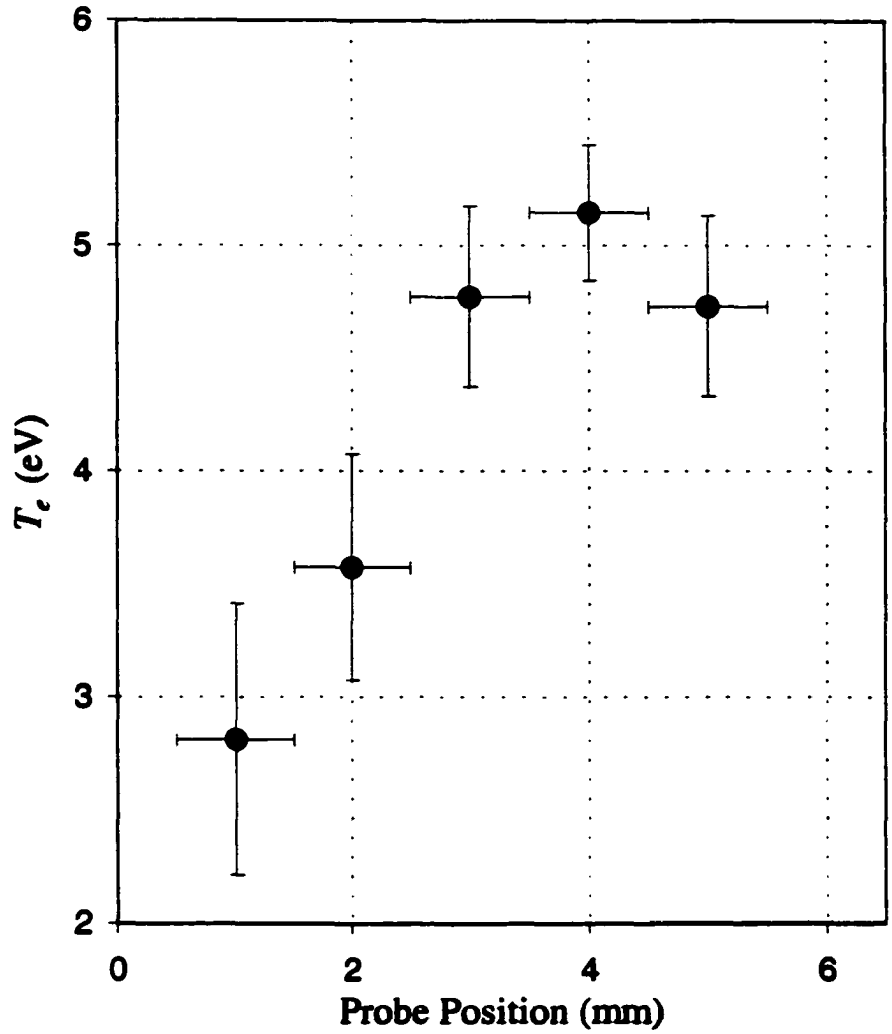

FIG. 29. Axial variation of electron temperature at p = 5.0 Torr and P = 0.3 W/cm^3 with the power electrode at 0.0 mm and the grounded electrode at 6.5 mm.

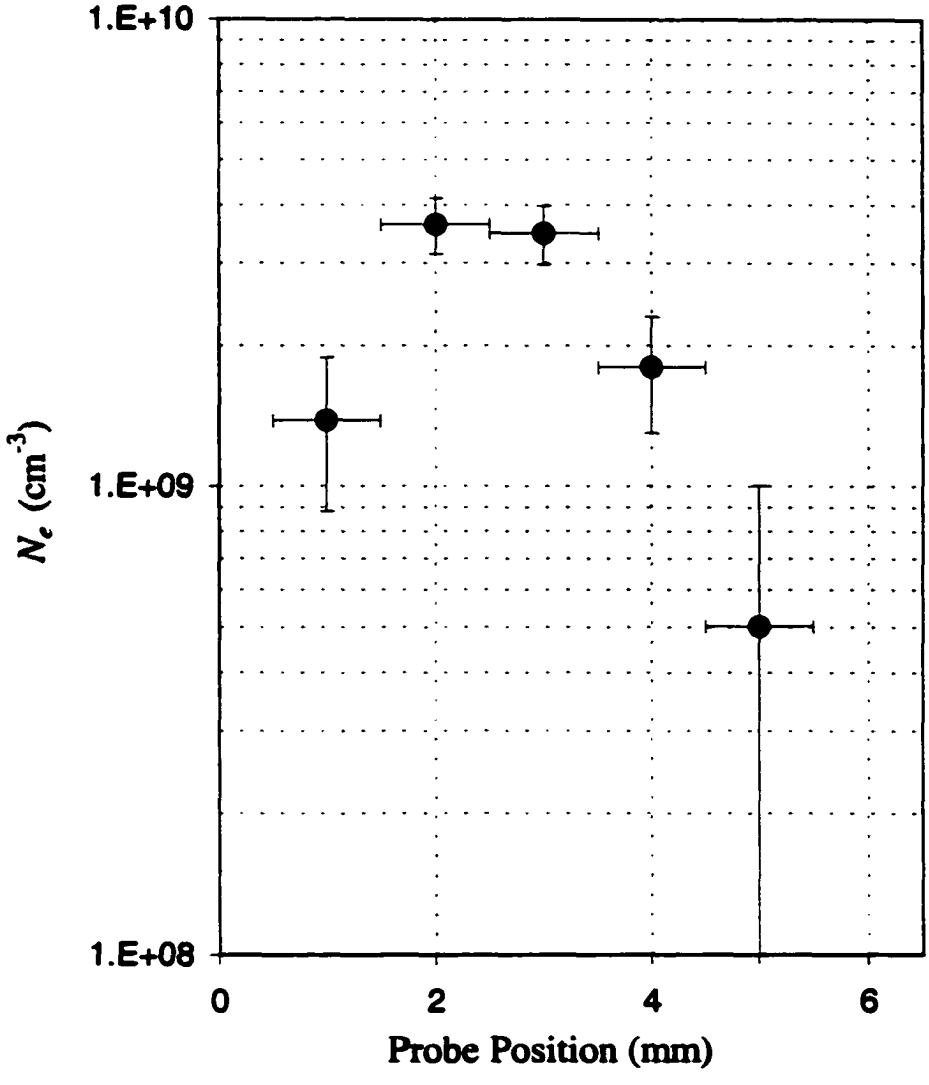

FIG. 30. Axial variation of electron density at p = 5.0 Torr and P = 0.3 W/cm^3 with the power electrode at 0.0 mm and the grounded electrode at 6.5 mm.

due to secondary electrons emitted from the electrodes due to bombarding electrodes with ions that are then driven toward the bulk with increasing energy during the next RF half period. It is possible that ultraviolet radiation affects the electrode surfaces and generates photoelectron; however, this was not taking into account in the present work. The axial distribution of N_e is typical for a capacitive discharge and was predicted by models and confirmed by experiments [43, 45, 47]. The maximum of N_e at the discharge center is due to several factors including the lowest electric field in that region and the sheath formation near the electrodes preventing electrons from approaching them. The slight shift of the N_e maximum closer to the power electrode is likely due to a higher positive potential for this electrode with respect to the other electrode, connected to ground. The y-axis error bars are the statistical error of the measurements and the x-axis error bars are the uncertainty in the probe position measurements.

Measurements of electron temperature and electron density based on the Langmuir double probe can contain systematic errors due to several effects. The primary systematic error can arise due to compatibility between the Debye length ($\lambda_D \sim 743[T_e/N_e]^{1/2} \sim 10^{-2}$ cm) and the electron mean free path ($l_e \sim [NQ_m]^{-1} \sim 10^{-2}$ cm). Then, only the energetic electrons are capable of reaching the probes. As a result, values of T_e can be overestimated due to the tendency to collect only "tail" electrons. Furthermore, N_e can be underestimated for the same reason. Only a fraction of the energetic electrons in the distribution reaches the probe surface. In addition, a constant noise effect from the RF source could be present all the time, even in the case when the RF filter circuit was installed between the probes and the external circuit.

A Langmuir double probe system was used to find the distribution of local electric field across the discharge gap by measuring the plasma potential difference between the probes knowing the probe separation distance. Note that we cannot measure the plasma potential, V_S. We only measure the potential difference between probes, which gives the average electric field of the region. Measurements of electric field are performed by placing the probes parallel to the transverse discharge axis and at different positions on the axis. The separation distance between probes was varied from 0.5 mm to 1.25 mm. Figure 31 illustrates the results in terms of the reduced electric field E/N, which is a more fundamental plasma parameter than the electric field itself.

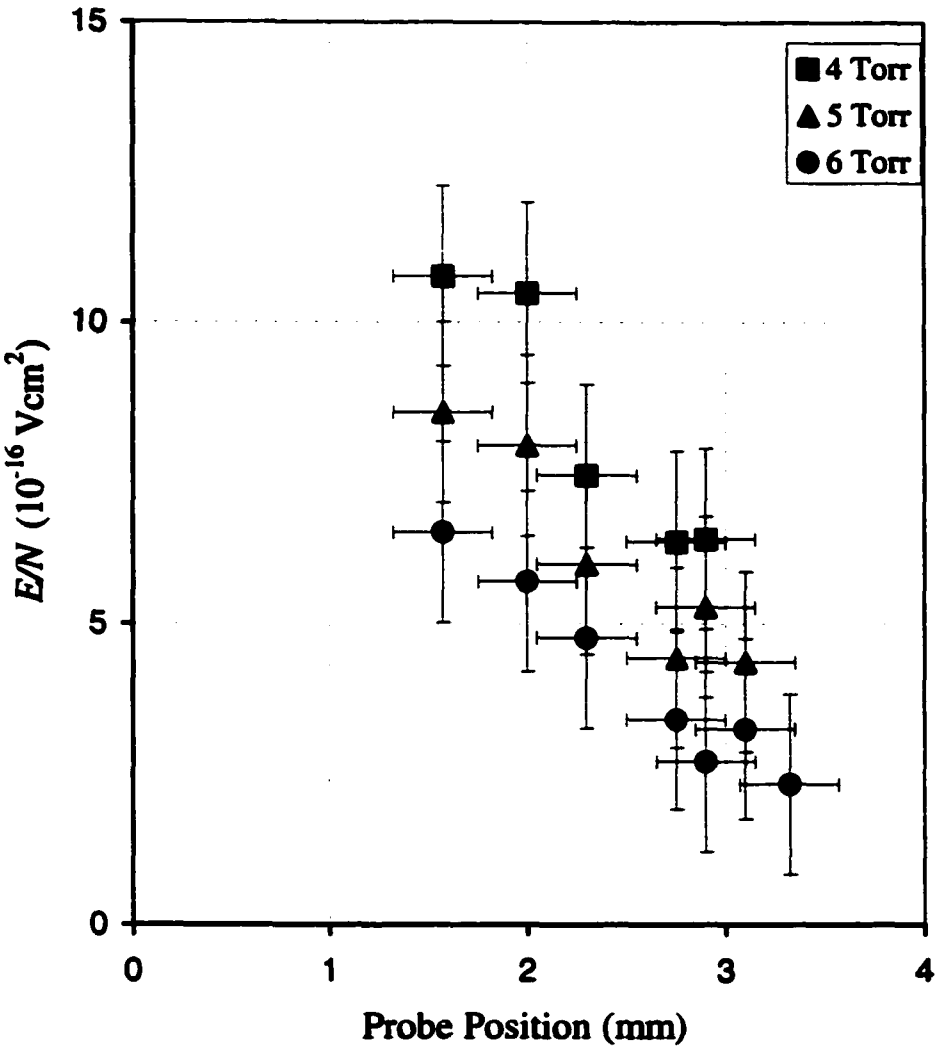

FIG. 31. Axial variation of reduced electric field at a power density of 0.5 W/cm^3 with the power electrode at 0.0 mm and the grounded electrode at 6.5 mm.

Gas density was determined from discharge pressure and gas temperature, assumed to be 400 K at the center of the discharge. Measurements were performed at several points on the discharge axis, from the center of the discharge to the powered electrode, at a power of 5.0 W, and a discharge gap of 6.5 mm. The reduced electric field was observed to increase close to the electrode. This result substantiates the presence of a sheath layer forming in front of the electrode where the potential decreases most rapidly. In addition, the reduced electric field decreases with increases in pressures.

The results of Langmuir probe experiments have revealed the characteristics of the present discharge. Electrons are concentrated in the discharge center with a density of approximately 3×10^{9} cm^{-3} and a mean temperature of 4 - 5 eV. The reduced electric field was lowest at the discharge center and increased toward the electrodes. The results of these discharge parameters are consistent with the prediction based on our simplified model in Section 2 (see Figures 6, 14, and 15) for T_e, N_e and E/N.

3.3 Determination of Gas Temperature

The gas kinetic temperature in reactive glow discharges is one of the crucial parameters needed to characterize the gas kinetics of the discharge. Since the rates of processes occurring in the discharge depend on the local gas temperature, the determination of gas kinetic temperature can help predict accurately the equilibrium of the mixture. Increases in gas kinetic temperature result in decreases of the gas density which results in an increase in the reduced electric field *E/N*. The reduced electric field, *E/N*, is the parameter used in the Boltzmann equation (see Eq. (2)) and therefore affects the EEDF and transport coefficients of the ionized gas. Therefore, it is considered the fundamental parameter of the discharge.

One of the standard diagnostic techniques used in discharges involving molecular gases is the determination of rotational temperature from the rotational spectra of the excited molecules. Rotational temperature often is identified with gas translational temperature, assuming thermodynamic equilibrium of the molecular gases in the discharge. However, it has been observed that rotational temperature may not be equal to translational temperature when chemical reactions are involved [48]. Therefore, we chose two different methods for measuring gas temperature in order to avoid any error based on the assumption of equivalence between rotational temperature and translational temperature. In the first section, we will discuss gas temperature measured by a classical thermocouple technique. This technique is affected by the perturbation of the measured signal due to the RF field. We will describe steps taken to reduce this effect.

In the next section, we will focus on the temperature measurements evaluated from the rotational emission spectrum of CO molecules in the discharge. We will describe possible errors arising from the assumption of thermodynamic equilibrium and the equivalence of rotational and translational temperature.

3.3.1 Thermocouple Measurement Technique

A type K thermocouple was made of Chromel/Alumel (Ni-Cr/Ni-Al) wire 0.005 inch in diameter. The maximum measurement range of the thermocouple is from – 200°C to 1250°C. The manufacturer's standard limit error is 0.75% at a temperature larger than 0°C. A Fluke digital thermometer, Model 2165A, was calibrated for use with this type of thermocouple. The thermocouple was calibrated at the temperature of boiling water, which is approximate the current discharge temperature range. The systematic error due to the electrical connection and length of the extension wire was estimated to be no more than 5% at room temperature, which is satisfactory in the present range of temperature measurements.

The thermocouple probe was placed into the plasma bulk region in the plane parallel to the electrodes. It was connected with a double electrical feed-through to the digital thermometer outside of the chamber. The experimental scheme is shown in Figure 32.

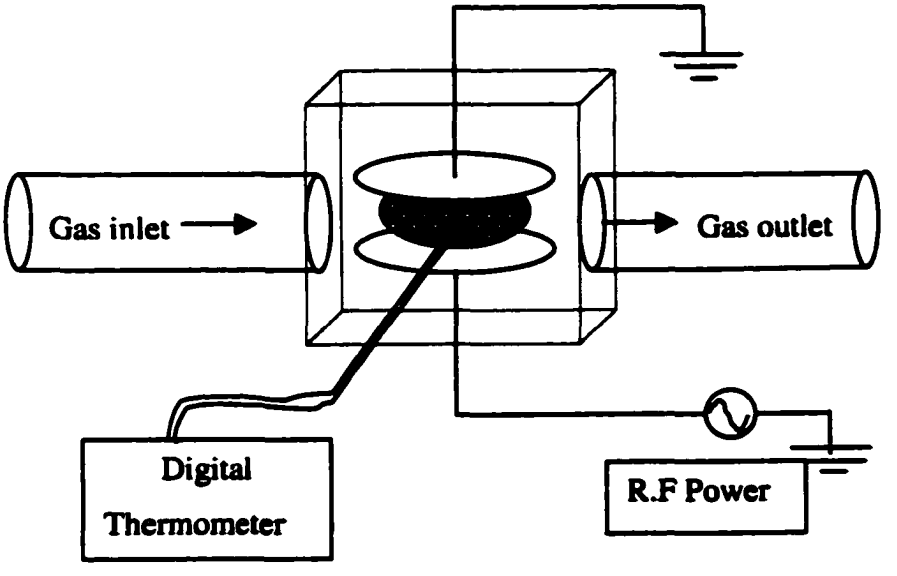

FIG. 32. Schematic of thermocouple probe measurement.

A large error can be introduced in the thermocouple measurements due to the influence of the RF field during the discharge since it acts as an antenna. One way to get around this problem is by monitoring at the decay of the thermocouple signal in the afterglow of the discharge. The thermocouple signal shows a sudden drop immediately after the discharge is turned off, and the amplitude of the drop is proportional to the operating power (Fig. 33). Since the duration time of the drop is much shorter than the normal decay time of the real discharge temperature, the amplitude of the discharge temperature can be determined by extracting the instantaneous drop from the decay signal. Gas temperatures in the discharge are then determined from the decay rate of the signal from the thermocouple.

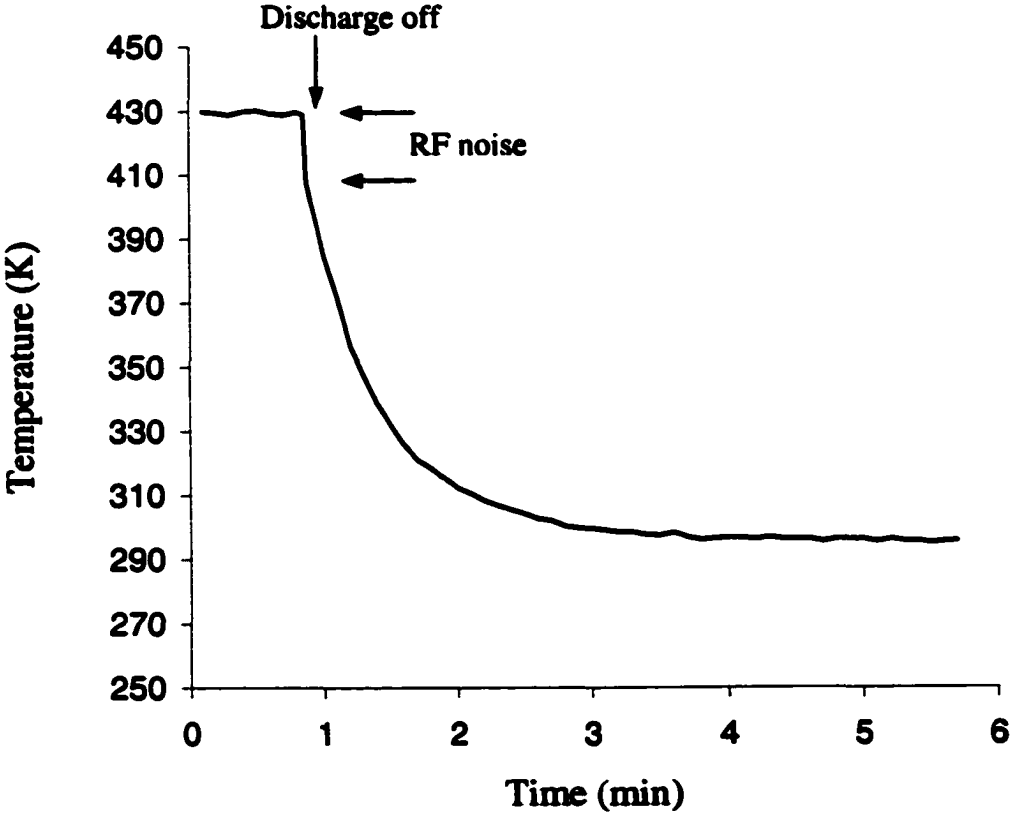

FIG. 33. Decay of temperature in discharge afterglow measured with thermocouple probe at $P = 5.0$ W, $p = 5.0$ Torr, $D = 0.8$ cm.

Figures 34 and 35 show discharge temperature as functions of the power at different pressures and different electrode gaps, respectively. In the low power range (e.g., $P < 5.0$ W), the temperature is linearly proportional to the discharge power. This is an expected consequence of cumulative ohmic heating in the plasma due to the momentum transfer collisions between electrons and neutrals. Larger power results in a larger applied oscillating field and in a larger effective momentum transfer to the neutral particles.

However, as the power increases further, the temperature shows a non-linear behavior, which arises due to boundary effects. The nonlinear behavior can be explained in the following way. When the power is low, the plasma is confined within the region between the electrodes where the electric field is uniform. As the power is increased gradually, the plasma expands radially toward the edge of the electrodes because of the increasing discharge current density. Hence, the average kinetic energy of electrons in the bulk increases, and the average gas temperature follows the increase similarly. The current density eventually reaches its the saturation limit due to the restricted area of the electrodes. As the power increases further, the discharge is no longer confined within the electrodes but expands around their edges. It is then shaped by the complex distribution of the electric field at the edges. Therefore, the power density is no longer increasing linearly proportional with increases in power, and the discharge temperature is no longer linearly proportional to power. The boundary effect is larger at higher pressures and at smaller discharge gaps as shown in Figures 34 and 35. In fact, the boundary effects at higher power can be observed directly by extended luminosity around the edges as shown in Fig. 36(b), and this is not the case in Fig. 36(a). The discharges in figures 36(a) and 36(b) are at the same pressure, $p = 6.0$ Torr, and at a discharge gap, $D = 6.5$ mm.

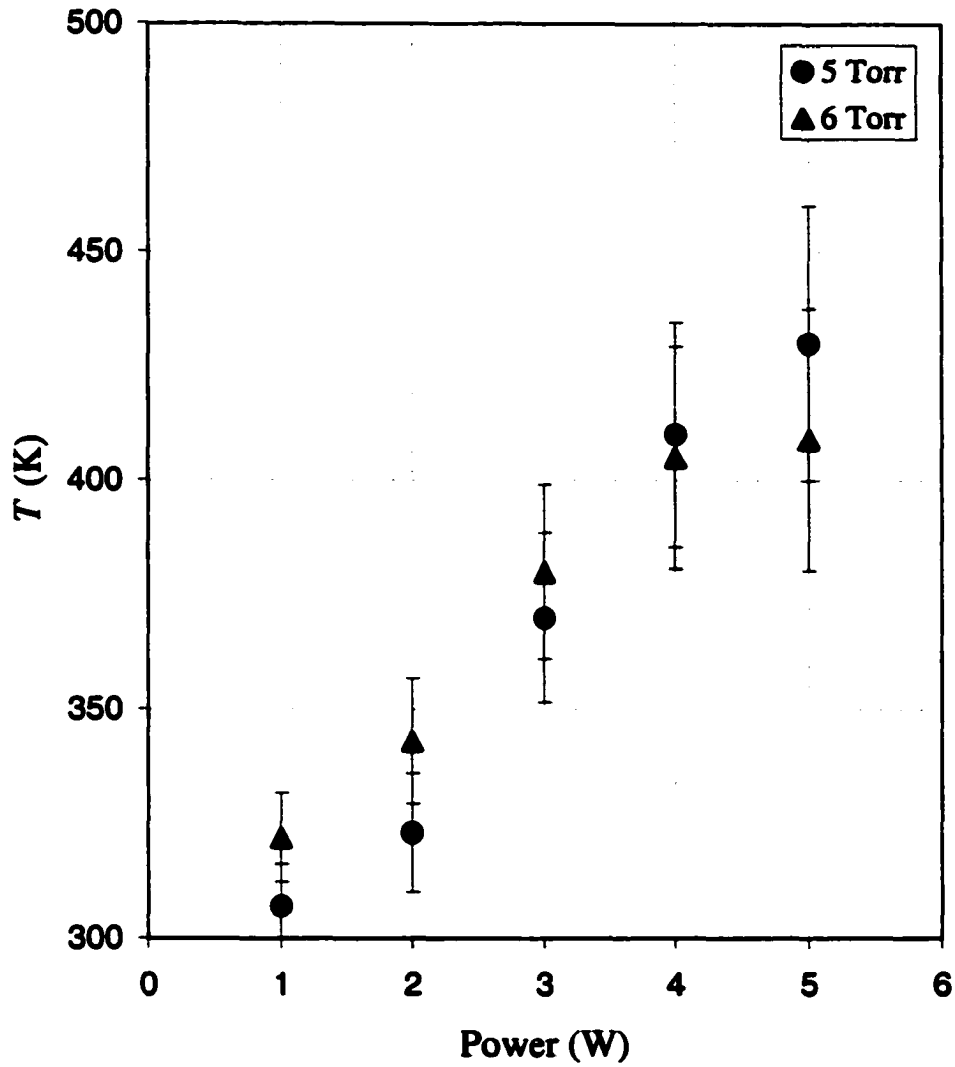

FIG. 34. Gas temperature as a function of power at gap D = 8.0 mm and different pressures.

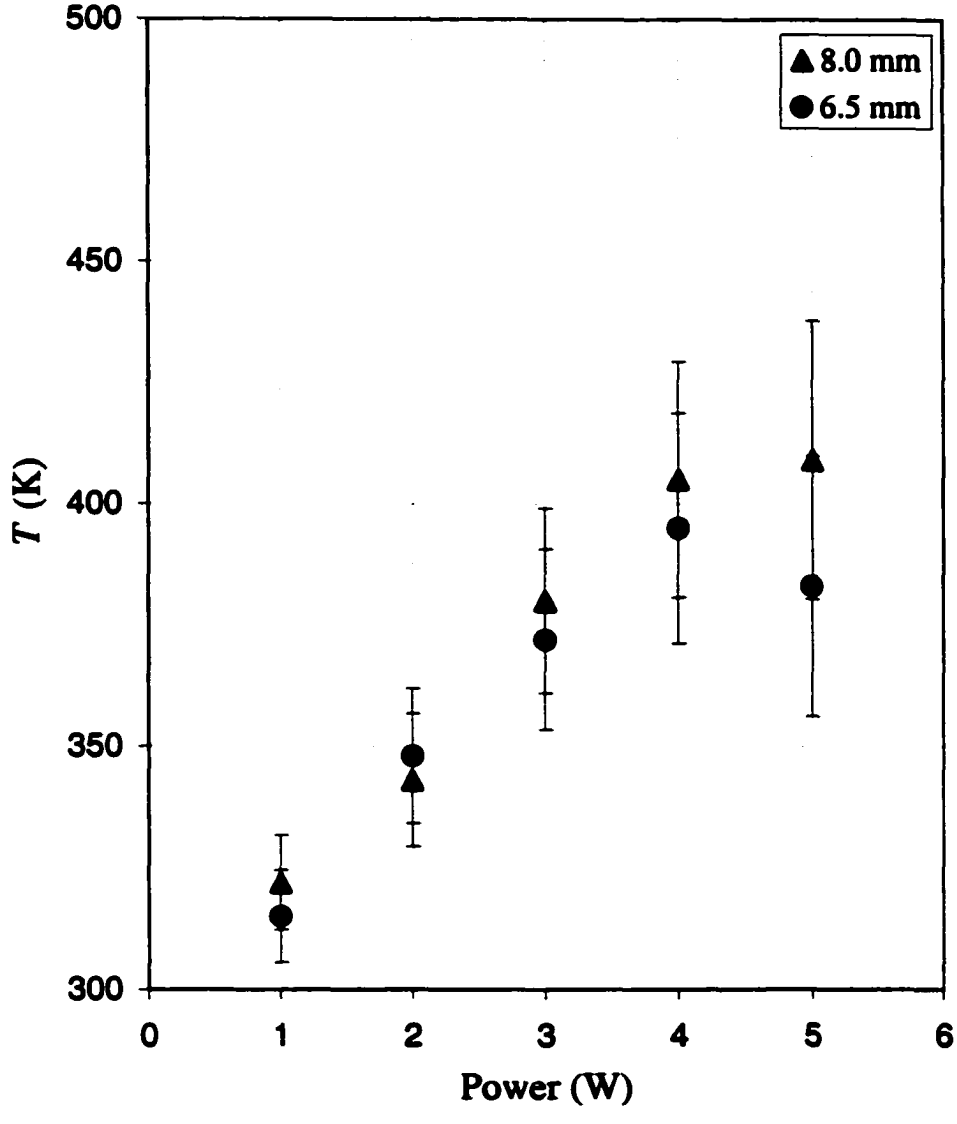

FIG. 35. Gas temperature as a function of power at a pressure of 6.0 Torr and different discharge gap.

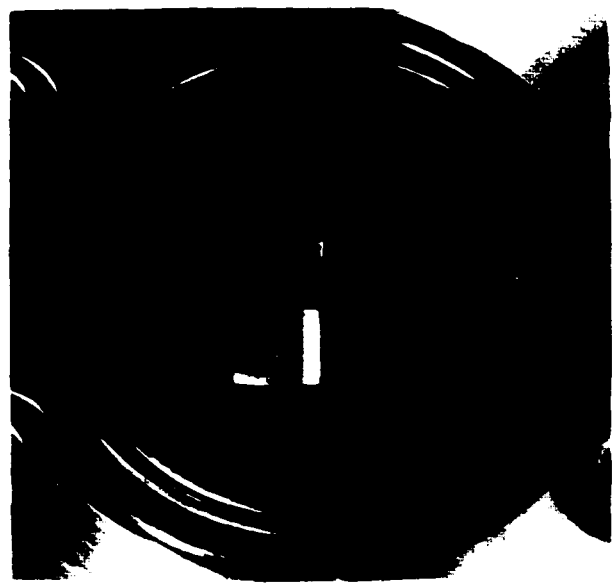

(a) $P = 3.0$ W

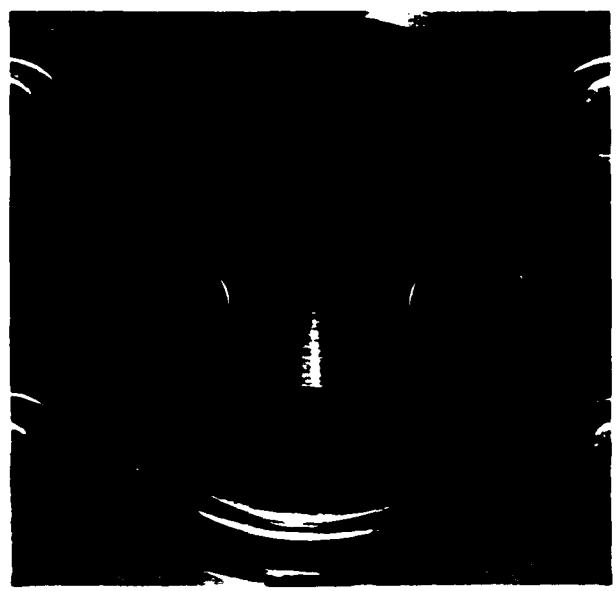

(b) $P = 6.0$ W

FIG. 36. Boundary effects. Discharge at low power (a) confined between the electrodes. Discharge at high power (b) penetrating laterally into the cell volume (see areas marked with circles).

Since the boundary effect results from the distribution of the field lines between electrodes and between the power electrode and the ground chamber, it can be minimized by placing a dielectric shield around the power electrode. In the present discharge configuration, the power electrode is a cylinder with a length of about 0.8 cm and a diameter of 2.54 cm. Two concentric hollow glass cylinders with a total thickness of 0.5 cm were used to shield the side of the power electrode from the discharge. Figure 37 and 38 compare temperature measurements as a function of power with and without the glass shield around the power electrode. Figures 37 and 38 show results at two different electrode gaps while the pressure was kept constant. Temperatures measured without the shield had a maximum or saturation value around $P = 4.0$ W. On the other hand, the measurements made with the shield show a linear relationship between the temperature and the power over the full range (the correlation coefficients of the linear fit of data points with shield are 0.996 and 0.985 in Fig. 37 and Fig. 38, respectively. These linear fits were not shown for the clarity of the figures). In addition, at the same input power, the measurements performed in the discharge with a smaller gap ($D = 0.65$ cm) had slightly smaller average temperatures than those measured with the larger gap ($D = 0.8$ cm). This effect can be explained by the heat loss from the bulk plasma to the electrodes. Heat transfer to the electrodes could be relatively large for the narrower discharge gap. Heat dissipation at the edges is relatively smaller than that to the electrodes. Therefore, cooling by heat transfer to the electrodes is much larger in the case of the smaller inter-electrode gap. As a result, it reverses the effects of ohmic heating due to the increase of the reduced electric field and cooling by convection.

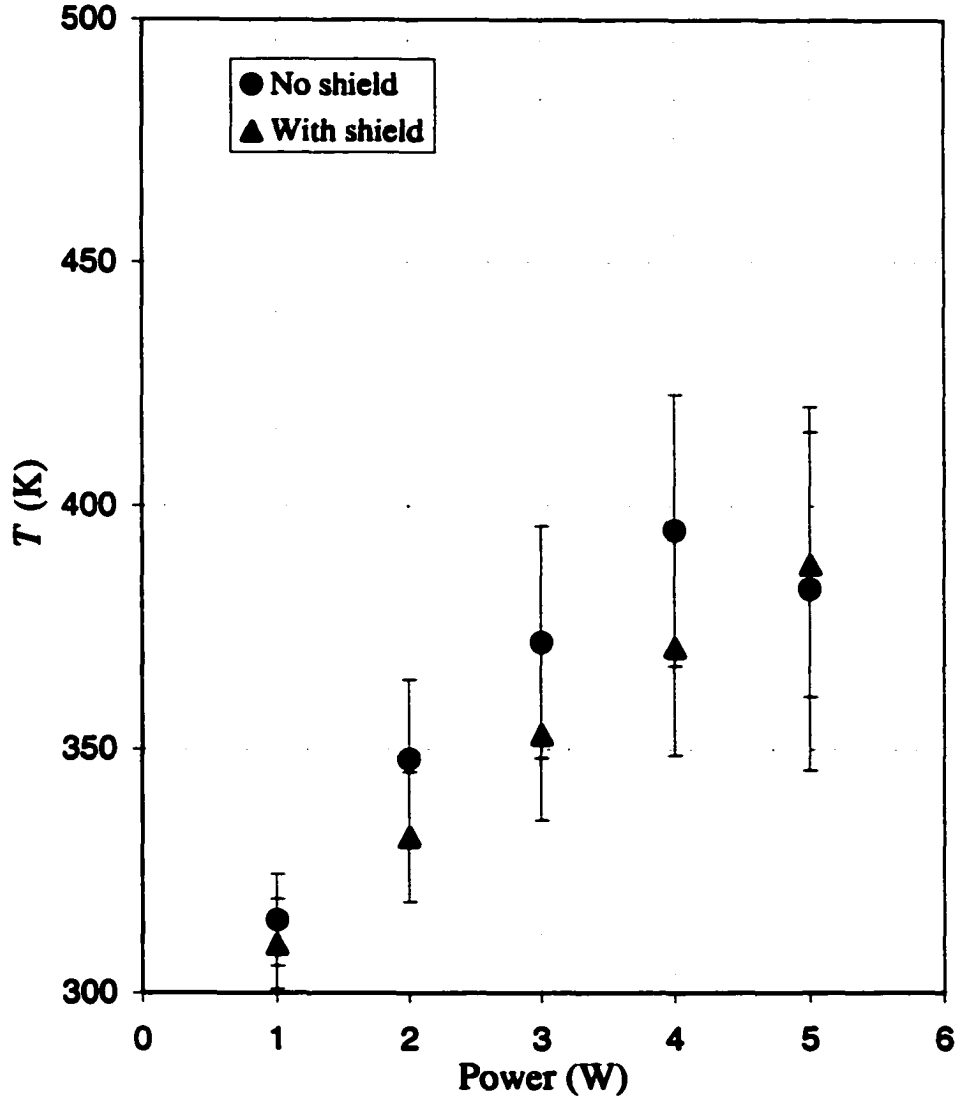

FIG. 37. Gas temperature as a function of power at gap $D = 6.5$ mm and pressure $p = 6.0$ Torr.

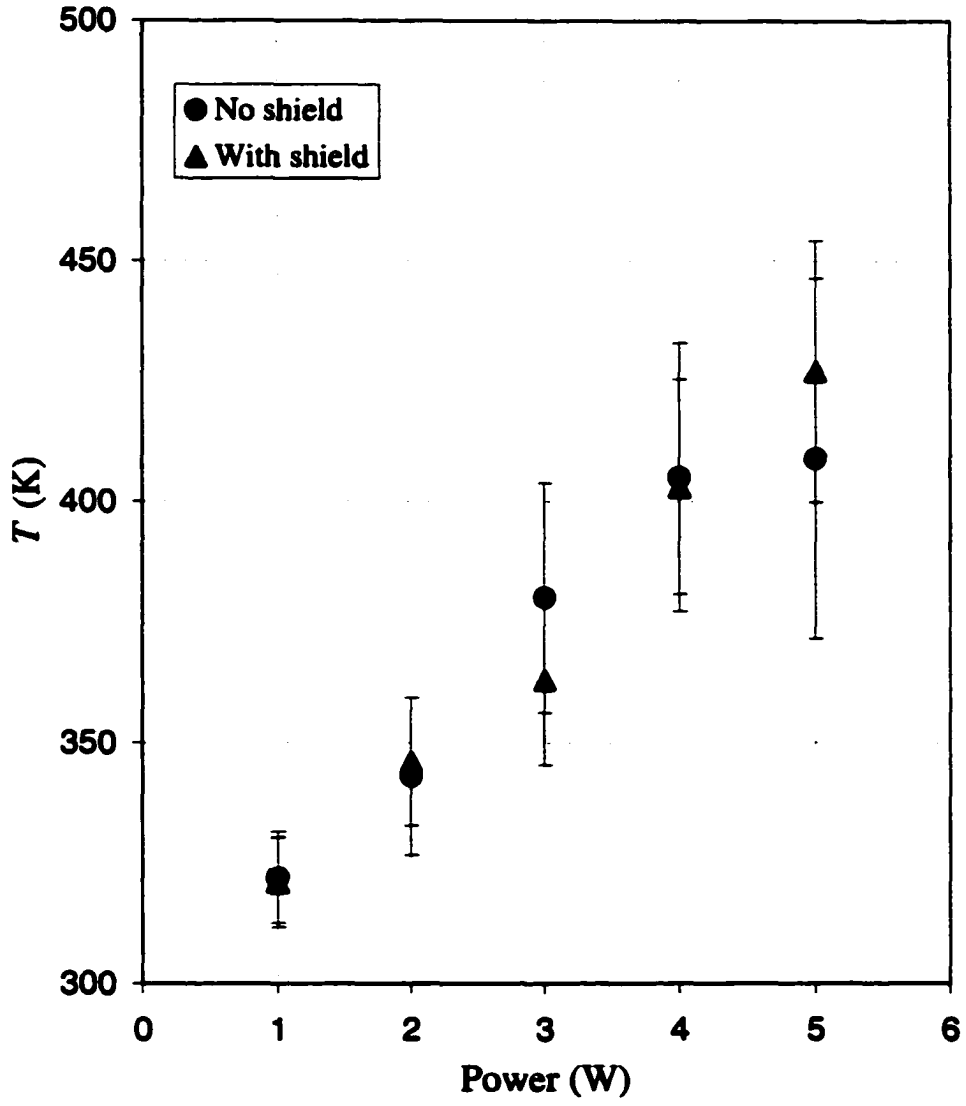

FIG. 38. Gas temperature as a function of power at gap D = 8.0 mm and pressure p = 6.0 Torr.

3.3.2 CO Emission Spectroscopy

Several highly accurate diagnostic techniques, such as coherent anti-Stokes Raman scattering, laser-induced fluorescence (LIF) and optical emission spectroscopy (OES) can be used to determine the temperature. The diagnostic techniques based on OES are attractive since they are simple, noninvasive and *in situ*. One example of OES is the spectroscopic determination of the rotational temperature from the spectra of diatomic molecules. The intensity of light emitted from excited molecules is used to perform the rotational temperature measurements.

When the gas mixture reaches equilibrium in a weakly ionized discharge (all chemical reactions play a minimal role), the only major inelastic collisions in the weakly ionized gas that could affect the gas temperature are the electron excitation and neutral-neutral collisions. Therefore, in steady state, heavy particles in gas discharge plasma can achieve partially thermodynamic equilibrium where rotational and translational temperatures are practically equal, although the electron and gas temperatures are far from equilibrium. Using the assumption of equivalence between rotational and translation temperature we can correlate accurately rotational temperature with gas temperature. The results of the rotational temperature based on OES are then compared with the gas temperature that was measured by the classical thermocouple probe.

The resemblance of the rotational energy distribution of excited state molecules to the ground state molecules is the basis for the gas discharge temperature measurements. In the ground state, the distribution of rotational levels in molecules is proportional to the Boltzmann factor, $exp(-E_{Rot}/kT)$. During electrical discharge, with an average electron energy of a few electron volts, the molecules are excited by electron impact. However, due to their large masses in comparison to electrons, the excited molecules have essentially the same angular momentum and rotational energies. Hence, the excited molecules possess nearly the same distribution of rotational levels as those in the ground state. By carefully examining the spontaneous emission spectra from the de-excitation process of the molecules, we can identify the rotational structure of the excited molecules. Therefore, we can deduce the rotational temperature of the molecules, which we identify with the gas temperature of the discharge.

The experimental setup used for the temperature evaluation is represented in Fig. 39. The monochromator (Jarrell Ash 82-000) has a focal length of 0.5 m and is equipped with a grating of 1180 grooves per millimeter. The spectral range of the monochromator is 190 nm to 910 nm. The resolution in the first order of the monochromator is 0.2 Å. The PMT is a Hamamatsu R928 with the wide spectral response range of 185 nm to 900 nm. The calibration of the spectroscopic equipment was performed using an argon discharge.

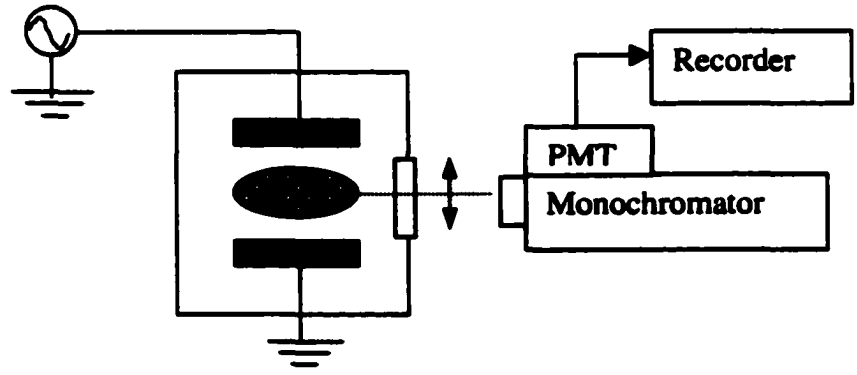

FIG. 39. Schematic of CO emission spectroscopy.

In the MSG discharge conditions, the most abundant constituents are CO_2, CO, O_2, and O. Among them, the CO molecule is the most favorable species for the rotational spectrum analysis due to its well-defined electric dipole moment, and its relatively strong band emission intensity, even in the visible spectrum. In the current experiment setup, we chose the Ångstrom system (Fig. 40) with the electronic transition from $B^1\Sigma^+$–$A^1\Pi$ (660.0–410.0 nm) in the visible range of the emission spectra of CO [50]. We observed the most intensive emission bands in the Ångstrom system ($B^1\Sigma^+$–$A^1\Pi$) with the band origin starting at 561.0 nm, 519.8 nm, 483.5 nm, and 451.0 nm. They correspond to *(0–3)*, *(0–2)*, *(0–1)*, and *(0–0)* of vibrational transitions respectively [51]. For the temperature analysis, we selected the rotational spectrum of *(0–2)* and *(0–0)* vibrational transitions, which correspond to the band origins 519.8 nm, and 451.0 nm, respectively.

The fine structure of each vibrational transition or band is comprised of many rotational transitions. Figure 41 shows an example of three rotational transitions belonging to the *P*, *Q*, or *R* branches in the *(0 – 0)* vibrational band of the B – A electronic excitation transition. In the example, three rotational transitions are from an excited state with a rotational quantum number $J' = 3$ to the lower states with rotational quantum numbers $J'' = 2$, 3, and 4 which are corresponding to $\Delta J = J' - J'' = +1$, 0, and -1, respectively. Therefore, in any excited vibrational band, with many upper rotational states, there are many rotational transitions which are categorized into *P*, *Q*, or *R* branches corresponding to the selection rules $\Delta J = J' - J'' = -1$, 0, or +1, respectively where J' and J'' are the upper and lower rotational quantum numbers.

The spectral location of the lines of each branch *R*, *Q*, or *P* in the spectrum can be identified accurately following the procedure outlined by Herzberg [50] including second order corrections of rotational constants. The wavelength is expressed in wavenumbers [cm^{-1}] (the number of wavelengths per centimeter).

$$\begin{aligned} \nu_R &= \nu_o + 2B' + (3B' - B'')J' + (B' - B'')J'^2 - (D' - D'')(J'+1)^2 J'^2 - 4D'(J'+1)^3 \\ \nu_Q &= \nu_o \quad + (B' - B'')J' + (B' - B'')J'^2 - (D' - D'')(J'+1)^2 J'^2 \\ \nu_P &= \nu_o \quad - (B' + B'')J' + (B' - B'')J'^2 - (D' - D'')(J'^2 + 1)J'^2 + 2(D' + D'')J'^3 \end{aligned} \tag{27}$$

where ν_o is the band origin of the electronic vibrational transition; *B* and *D* are the rotational constants of the first order and second order corrections; both *B* and *D* have wavenumber units, cm^{-1} and they depend on the specific vibrational level; *J* is the rotational quantum number; the single prime and double prime stand for the upper and lower states, respectively. For the *(0-2)* band of the $B^1\Sigma^+ - A^1\Pi$ transition, the values of the band origin, and other rotational constants ν_o, *B*, and *D* are given in Table II using constants taken from Ref. [51].

In the rotational spectrum obtained from the experiment, we could identify the rotational transition lines, and the rotational quantum numbers that correspond to them. In order to get the rotational temperature, we need to go further by comparing the relative intensities of rotational lines with respect to their rotational quantum numbers.

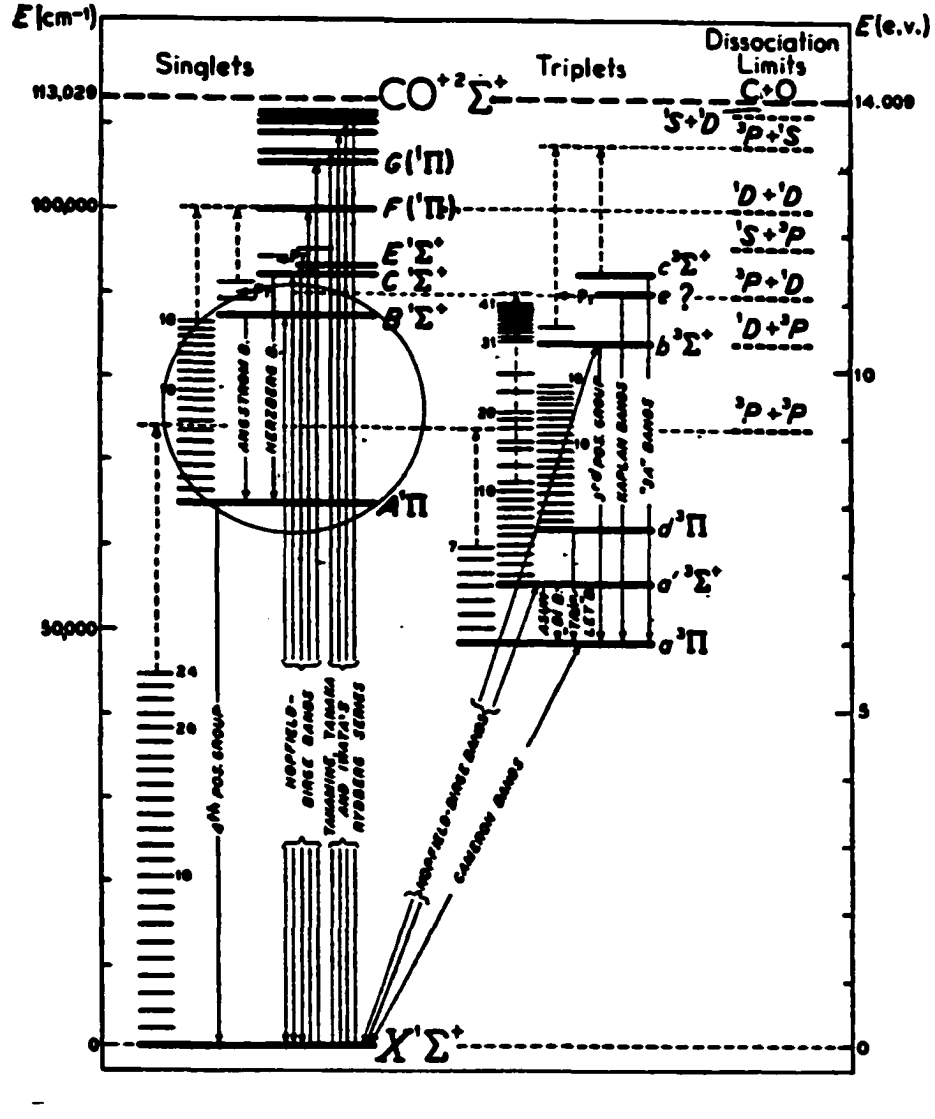

FIG. 40. Energy level diagram of the CO molecule from Ref. [50].

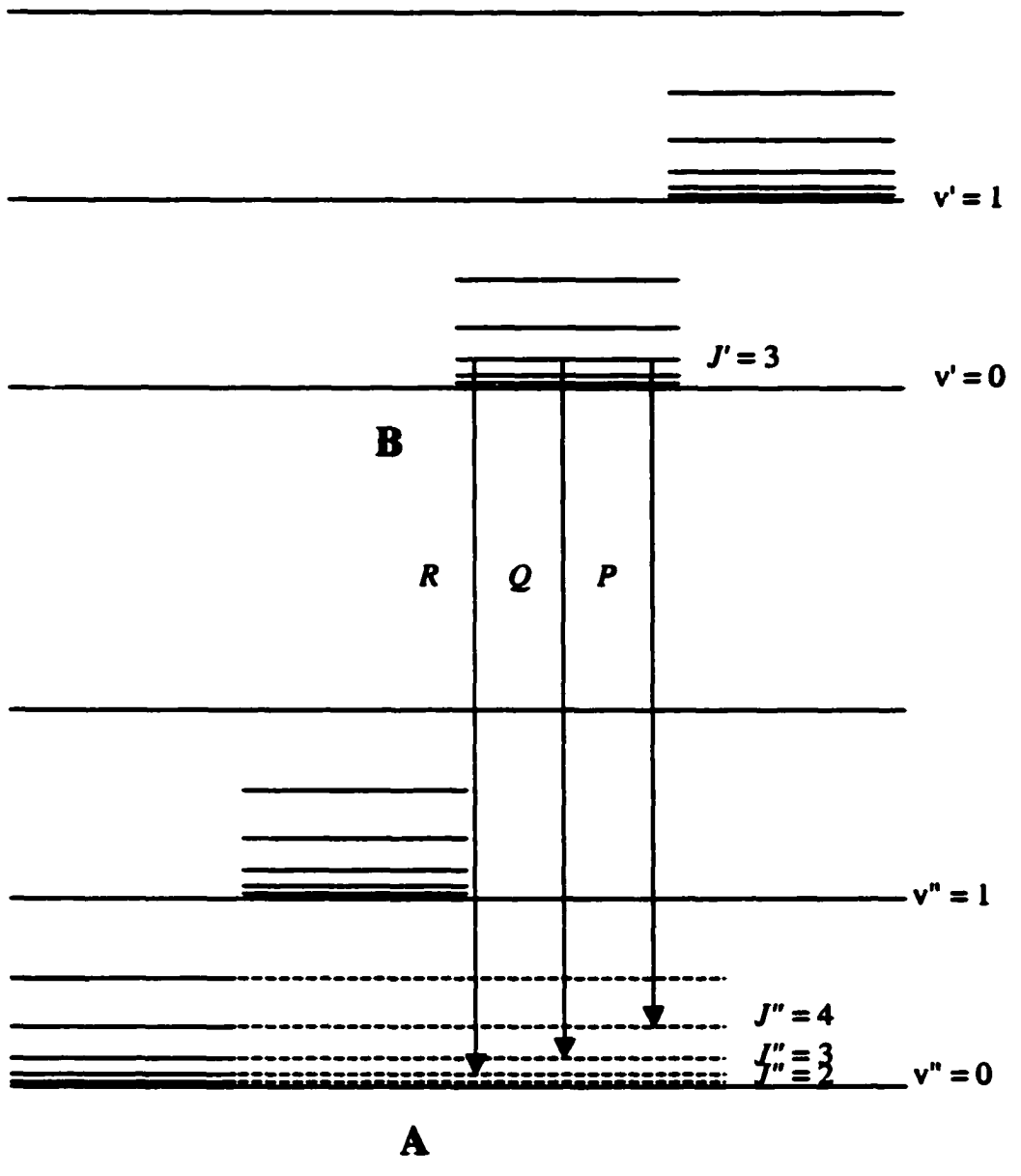

FIG. 41. Example of three rotational transitions belonging to the *P*, *Q*, and *R* branches in *(0 – 0)* vibrational band of *B – A* electronic excitation system. *P*, *Q*, and *R* correspond to $\Delta J = -1, 0, +1$, respectively.

The relationship between the spontaneous emission intensity and the rotational quantum number [50] is given as follows (see also Appendix B)

$$I_E = \frac{2C_E\nu^4}{Q_r} S_{J'} e^{-\frac{B'J'(J'+1)hc}{kT}} . \qquad (28)$$

C_E is the constant that depends on the change of the dipole moment and the total number of excited molecules; ν is the wave number of the transition expressed in conventional units of cm^{-1}; c, h, and k are the speed of light, Planck's, and Boltzmann's constants, respectively. Q_r is the partition function for all the rotational levels; B' and J' are the rotational constant and quantum number of the excited state; $S_{J'}$ is the light strength and is proportional to the matrix elements of the electric dipole moment, where the subscript indicates the dependency of the rotational quantum number of the excited state. The simplest expression for $S_{J'}$ is given by Hönl and London [52] based on the differences in total angular momentum between electronic levels (see Appendix B).

TABLE II. Rotational constants of *(0-2)* band in the Ångstrom system of CO emission spectrum, $B^1\Sigma^+ - A^1\Pi$ with the band origin, $\lambda_o = 519.8$ nm.

$B^1\Sigma^+$ state (upper state)	B'_e (cm^{-1})	1.961
Vibrational level v' =0	α'_e (cm^{-1})	0.027
	D'_e (cm^{-1})	6.958E-06
$B'_{v'} = B'_e - \alpha'_e(v'+1/2)+...$	$B'_{(v'=0)}$ (cm^{-1})	1.9475
$D'_{v'} = D'_e$	$D'_{(v'=0)}$ (cm^{-1})	6.958E-06
$A^1\Pi$ state (lower state)	B''_e (cm^{-1})	1.6116
Vibrational level v" = 2	α''_e (cm^{-1})	0.02229
	D''_e (cm^{-1})	7.289E-06
$B''_{v''} = B''_e - \alpha''_e(v''+1/2)+...$	$B''_{(v'=2)}$ (cm^{-1})	1.5558
$D''_{v''} = D''_e$	$D''_{(v'=2)}$ (cm^{-1})	7.289E-06
Band Origin	ν_0 (cm^{-1})	19240.3

In the Ångstrom system $B^1\Sigma^+ - A^1\Pi$ of CO molecules, the upper and lower electronic states have total angular momentum numbers 0 and 1, respectively, and the difference of total angular momentum $\Delta\Lambda = -1$. Using Hönl and London formulae [52], the line strength is found to have the largest value for the Q branch (e.g., $\Delta J' = 0$), which means we expect to see the strongest emission from this branch. Using Eq. (28) with a given temperature, $T = 450$ K, the plot of the relative intensity distribution of the P, Q, and R branches as functions of J' numbers shows the peak intensity of the Q branch almost twice that of the P or R branches, and the peak occurs around a J' value of 10 (Fig. 42). Furthermore, use of Eq. (27) to plot the rotational quantum number, J', as a function of the transition wavelength λ, also known as the Fortrat diagram, shows the close packing of rotational transitions at small J'. This is an indication of an overlap possibility and the difficulty in distinguishing which of the rotational transitions belong to different branches P, Q, or R at the low rotational quantum numbers (Fig. 43). Since the current resolution of the monochromator was relatively poor (~ 1 Å), large rotation quantum numbers were used in order to avoid the overlap of the rotational transitions.

Eq. (28) can be rewritten in the following form

$$\ln\left(\frac{I_E}{2J'+1}\right) \propto -\frac{B'hc}{kT}J'(J'+1), \tag{29}$$

where $S_{J'}$ was replaced with the factor $(2J'+1)/4$ which is calculated from the Hönl and London formulae for the Q branch of the $^1\Sigma^+ - {}^1\Pi$ transition; all other coefficients are treated as constants with respect to J' and their logarithms are also constants with respect to J'. Therefore, the linear plot of the logarithm of normalized emission intensity, $ln[I_E/(2J'+1)]$ with respect to $J'(J'+1)$ has a slope which is inversely proportional to the rotational temperature of the excited molecules.

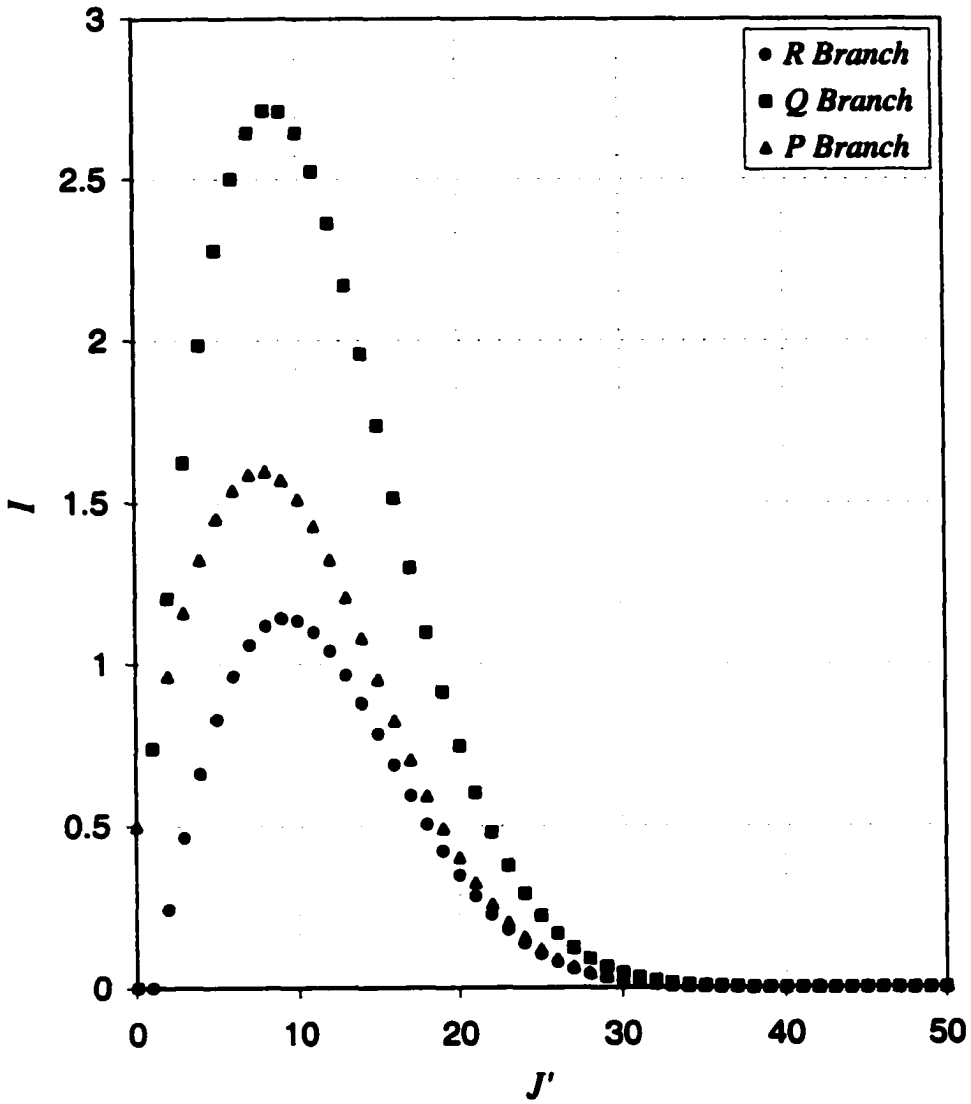

FIG. 42. Intensity distribution of rotational branches in *(0 – 2)* band of the Ångstrom system, $B^1\Sigma^+ - A^1\Pi$ in CO emission spectrum at $T = 450$ K.

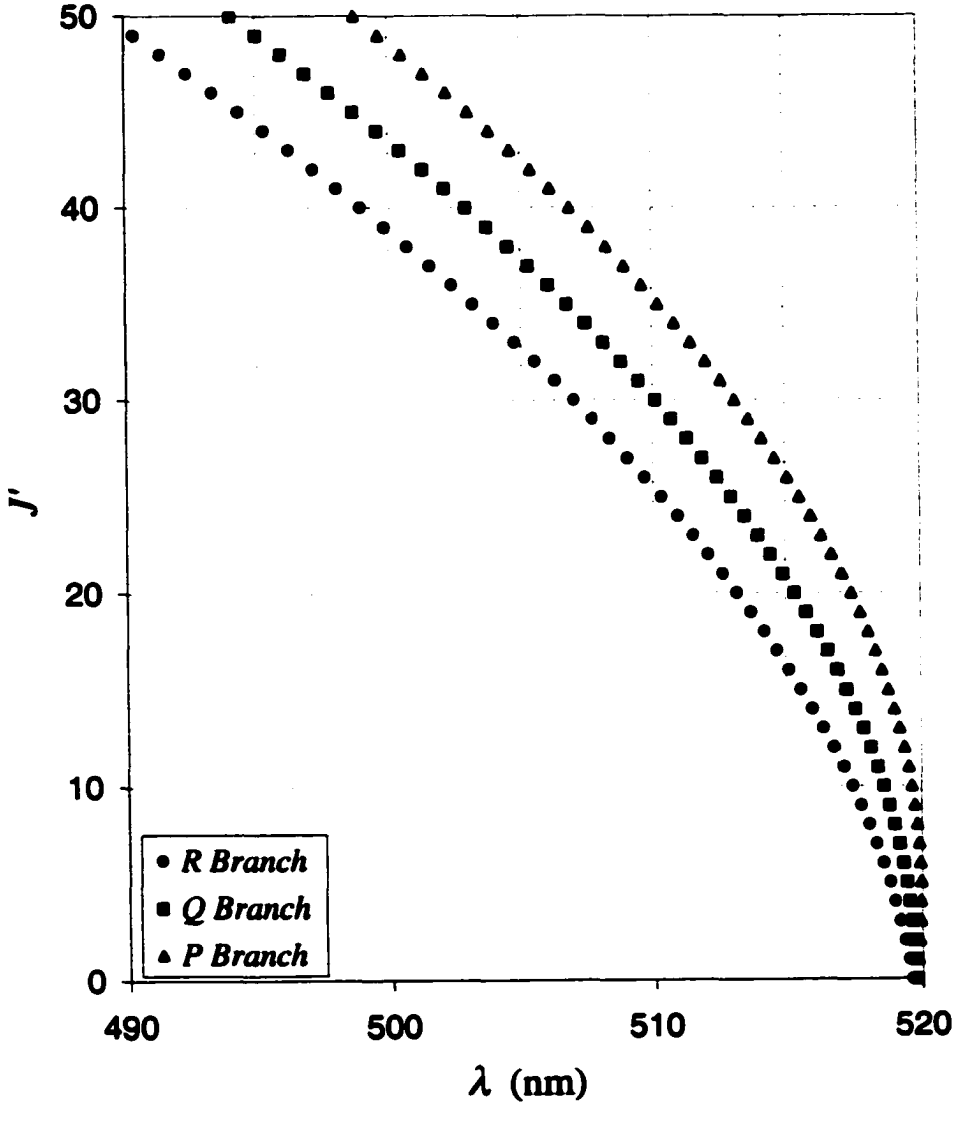

FIG. 43. Fortrat diagram of CO *(0 – 2)* band in $B^1\Sigma^+ - A^1\Pi$.

Figures 44 and 45 show the rotational temperatures deduced from the slopes of the fitting lines at two different power levels with other discharge parameters kept constant. The spectrum was taken at the discharge conditions assumed to be in equilibrium and after relatively long discharge times. The pressure remained practically constant during the data taking process. The purpose was to keep the chemical reactions at a low level and reduced the systematic error due to the chemical reactions when one evaluates the rotational temperature. The discharge gap was also fixed at D = 6.5 mm throughout all measurements to ensure a fixed discharge volume. Figure 46 shows the rotational temperature of CO at the same conditions as in Fig. 44 but the analysis was taken at the separated band, $(0-0)$ with the band origin at λ_o = 450.0 nm. The error bars in Fig. 44 to Fig. 46 are due to the uncertainty in the intensity measurements. The errors in the rotational temperatures are due to the slope differences by removing few rotational lines with the smallest rotational quantum numbers, which can have the most overlapped possibility (see Fig. 43, Fortrat Diagram).

The results of temperature measurements using a thermocouple and using CO rotational emission spectrum are compared in Fig. 47. All measurements were taken at the same discharge pressure p = 6.0 Torr, and discharge gap D = 6.5 mm. The thermocouple measurements were described in Section 3.3.1 and were performed with the dielectric shield. The agreement between the two measurements is within 10% in absolute temperature. There is a slightly higher temperature from the CO rotational emission spectrum than the temperature measured via thermocouple.

A comparison of measurements by the two completely different techniques gave us a relatively accurate idea about the actual discharge temperature range. The afterglow discharge temperature measurements (from the temperature decay after turning off the discharge) with the classical thermocouple could be used to identify the lower bound of the real temperature. On the other hand, the rotational temperature could be considered as the upper limit of the discharge temperature.

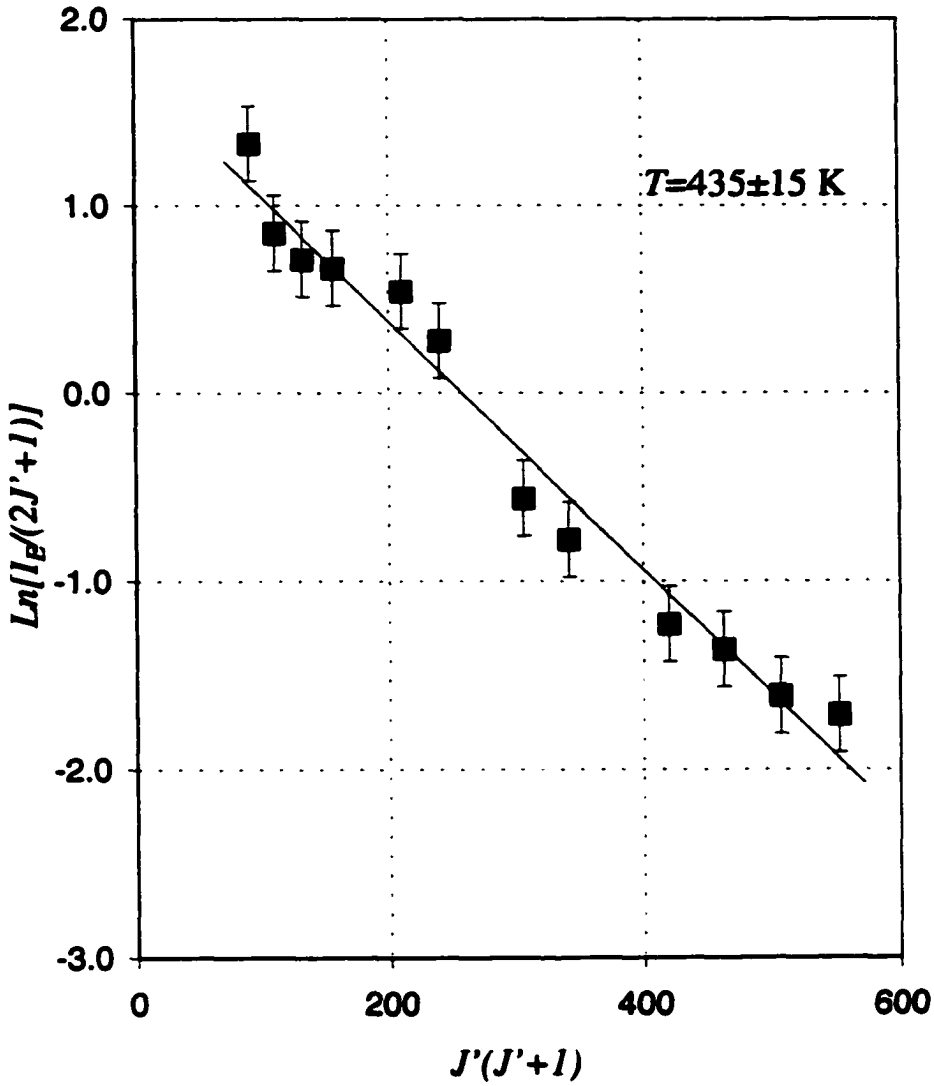

FIG. 44. Rotational temperature from the Q branch of the CO *(0 – 2)* band with λ_o=519.8 nm at $P = 5$ W and $p = 6$ Torr.

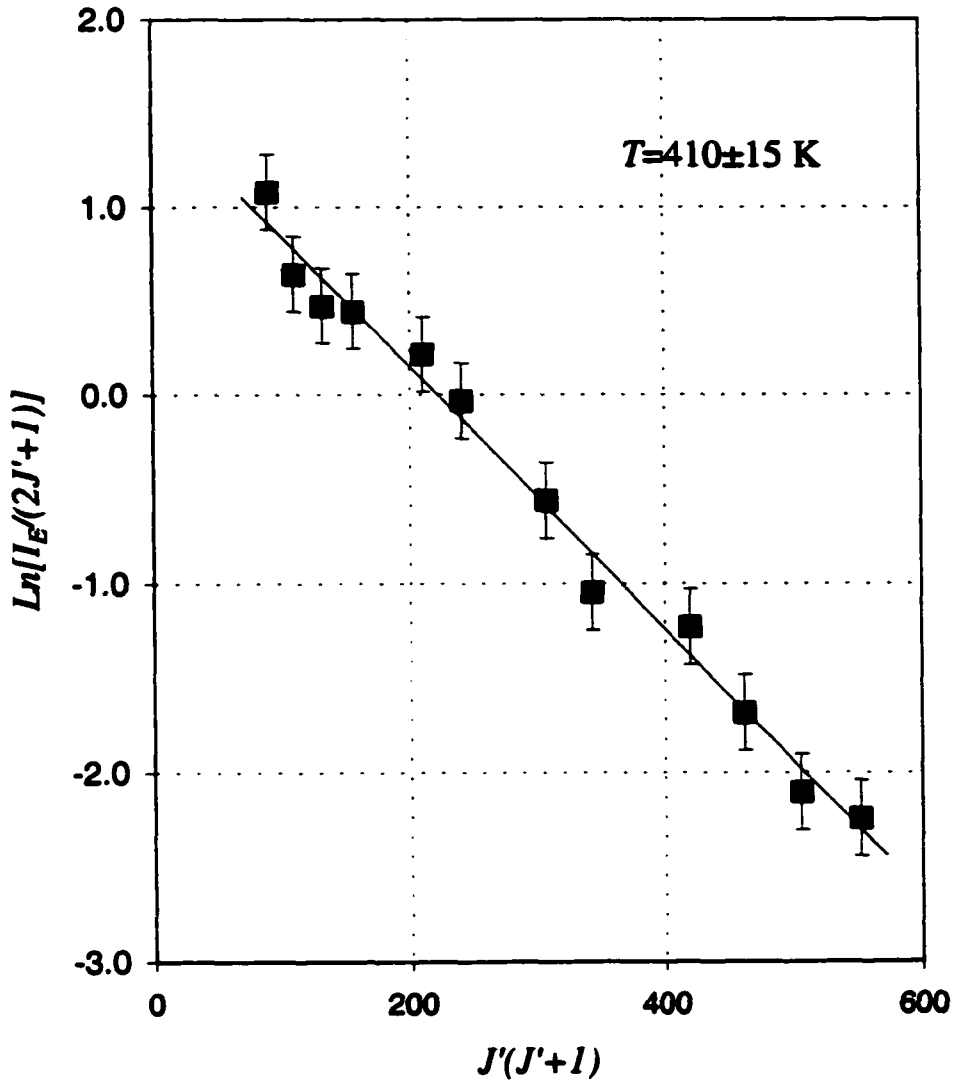

FIG. 45. Rotational temperature from the Q branch of the CO *(0 – 2)* band with $\lambda_o = 519.8$ nm at $P = 4$ W and $p = 6$ Torr.

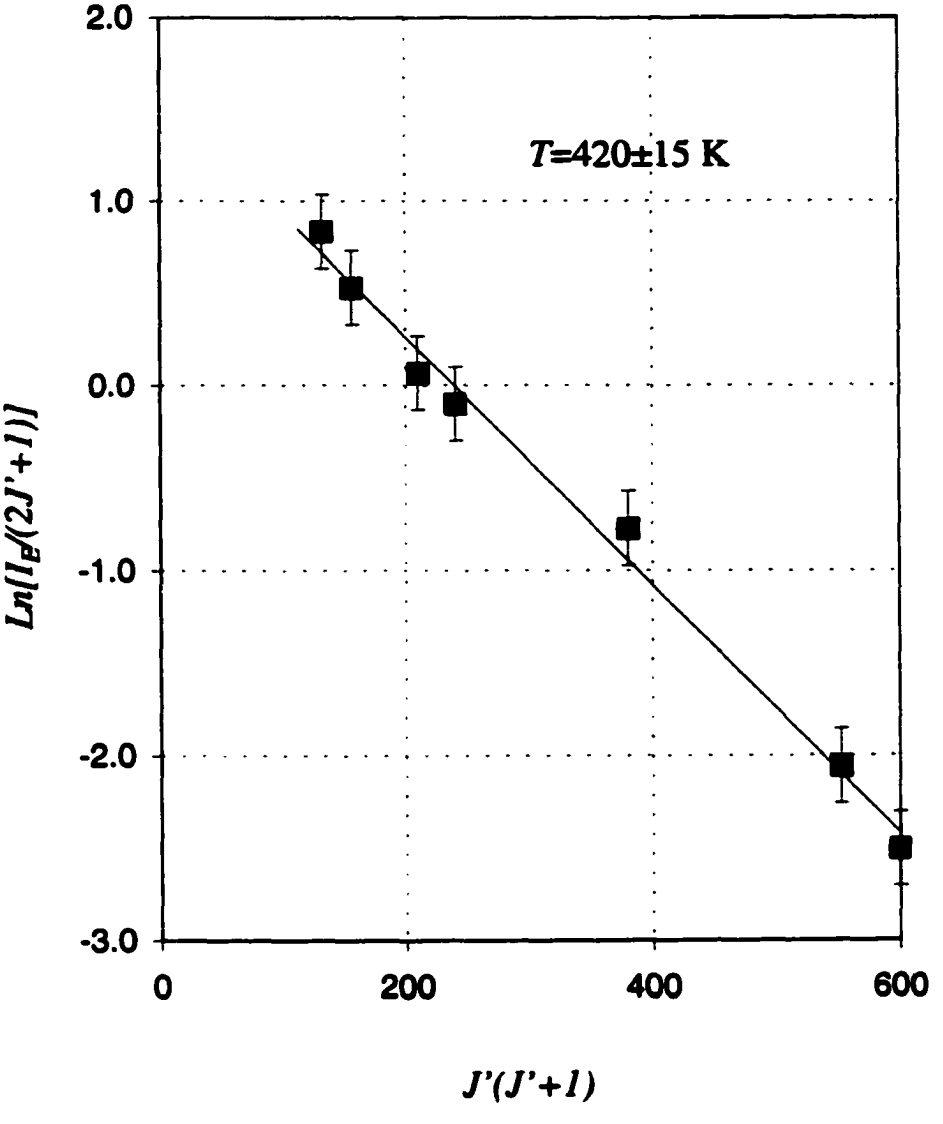

FIG. 46. Rotational temperature from the Q branch of the CO *(0 – 0)* band with $\lambda_o = 451.0$ nm at $P = 5$ W and $p = 6$ Torr.

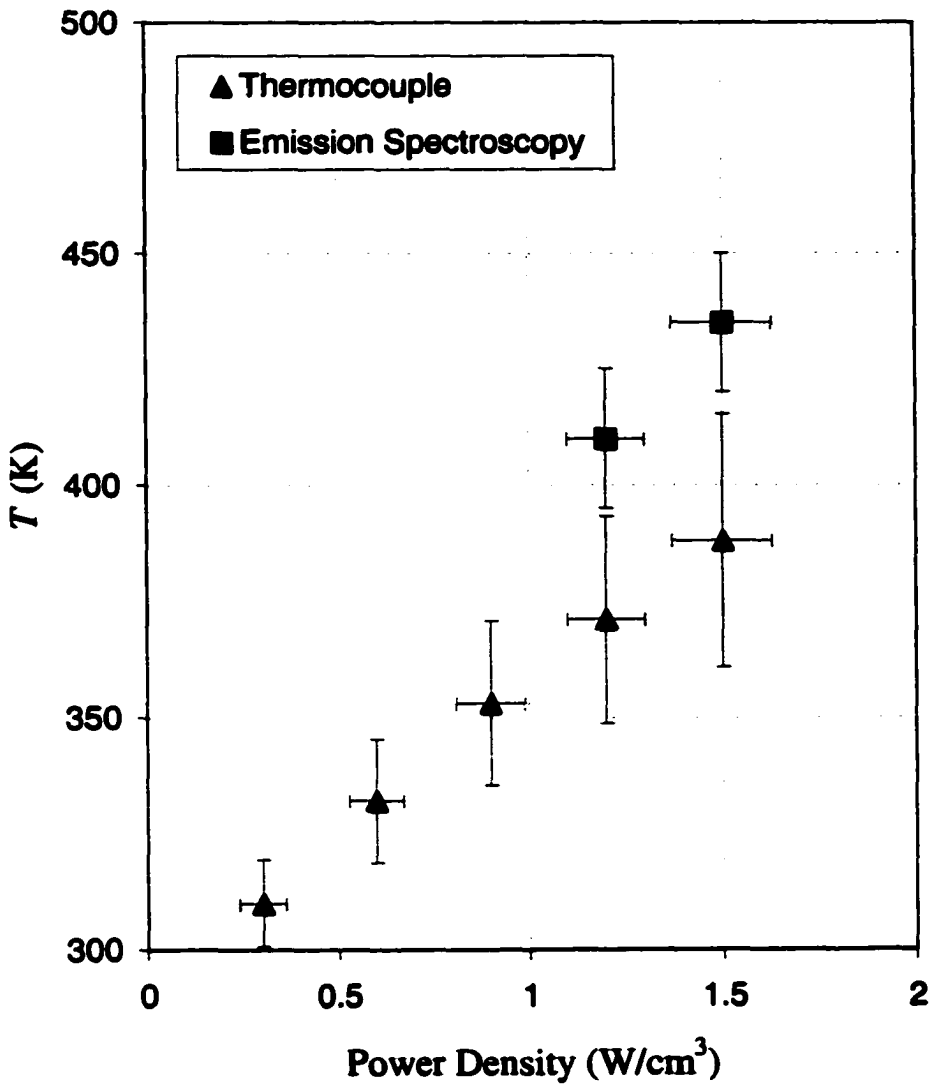

FIG. 47. Summary of gas temperature measurements.

The assumption of thermodynamic equilibrium between excited molecules and ground molecules, and the chemical equilibrium in the discharge may not always be true. The excited state molecules can obtain some additional rotational energy before they de-excite to the ground state due to excited – excited collisions or excited – ground collisions; moreover, during chemical equilibrium some chemical reactions can occur that increase the rotational temperature of the molecules. Therefore, the rotational temperature is always slightly higher than the actual discharge temperature. Imposing these temperature boundaries will guide us to deduce the appropriate discharge temperature. As seen in Fig. 47 two methods produce results that are in good agreement, and we can conclude that gas temperature in our discharge is determined to within about 10% uncertainty.

3.4 Gas Composition Measurements

3.4.1 Experimental set- up and QMS Calibration

The gas composition of MSG RF discharge was measured using a quadrupole mass spectrometer (QMS) (Fig. 18) at various discharge conditions. The gas mixture was sampled through a glass tube with an inner diameter of 1.5 mm and outer diameter of 3.5 mm. The glass tube was positioned closed to the edge of the electrodes to minimize possible distortion to the plasma and ensure that the gas is extracted the gas directly from the discharge region. Due to a large differential pressure between the discharge chamber (~few Torr) and the QMS chamber (10^{-7} Torr), a leak valve was used to sample the discharge gas. The signal to noise ratio of the QMS was maximized by keeping the QMS background pressure from 10^{-9} to 10^{-10} Torr when there was no measurement. The high vacuum of the QMS was achieved using two ion pumps with a total maximum pumping speed of 520 l/s. After taking several gas samples, the leak valve was closed completely so that the ion pumps had time to pump the QMS chamber down to normal background pressure. In every measurement, the leak valve was opened at the same position with the help of a precise dial (1/1000). The mass spectrum was calibrated with pure CO_2, Ar, O_2, and N_2 for mass to charge ratios (*m/e*) peaks of 44, 40, 32 and 28, respectively. The difference of ionization efficiencies between N_2 and CO is considered negligible. Indeed, the QMS was operated with electron energy around 70 eV. At that electron energy, the ionization cross sections of N_2 and CO vary by about 5% [55]. The calibration of the QMS with various gases was the essential procedure. The procedure was used to obtain not only an accurate mass spectrum but also the relative mass sensitivity due to the difference between the ionization cross sections. It was found that the sensitivity depends on the electron emission current in the QMS as shown in Fig. 48. The linearity of peak intensities with the pressure was also confirmed. Furthermore, pure CO_2 was used to determine the contribution of its fragments inside the QMS, such as CO, and O, which could alter the actual percentages of products from MSG decomposition. The consistency of the mass spectrum of initial MSG was always

verified before the discharge was activated. Final gas composition was obtained from the relative intensity in the mass spectrum and normalized to the initial MSG composition. Variation of sensitivity of CO and O_2 with respect to CO_2 was taken into account.

The gas mixture was sampled at various RF discharge parameters. RF power was operated within 1.0 W to 5.0 W. Pressure was varied from 3.0 Torr to 6.0 Torr. The interelectrode gap was changed from 6.0 mm to 8.0 mm. The discharge was also tested at different frequencies: 20 MHz to 40 MHz, and the resulting gas composition had no significant difference in its steady state condition. Therefore, we chose the RF frequency that had the best impedance matching. In the present experiment, we concentrated on the steady state gas composition only. Therefore, all measurements were obtained long after the discharge started.

The effect of water vapor was also investigated at various discharge conditions. Experiments were performed with and without a water trap. In addition, the edge effect in the discharge at high power density was excluded by placing a dielectric shield around the power electrode. The procedure was described in Section 3.3.

The intensity of atomic oxygen (m/e = 16) was found to be proportional to the intensity of CO_2 (m/e = 44). This implied the detected O signal was mainly a direct fragment of CO_2 decomposition inside the QMS and was not coming from the discharge. This could be expected since atomic oxygen is a strongly reactive species. Any atomic oxygen remaining after the discharge is deactivated will recombine to form an oxygen molecule either by a third body reaction like reactions (R5), and (R6) in Section 2.3, or at the wall. Therefore, the intensity of m/e = 32 is taken to be the fractional concentration of two moles of atomic oxygen and one mole of oxygen molecules from the discharge. The results were obtained in the form of relative concentrations of CO_2, O_2 and CO, which were the most abundant and stable species detected by the QMS at all discharge conditions.

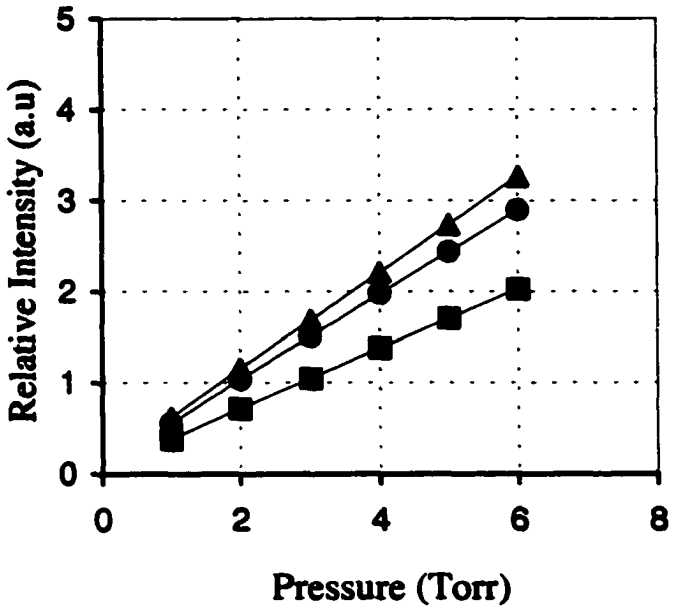

(a) Electron emission current, I_C = 1.0 mA.

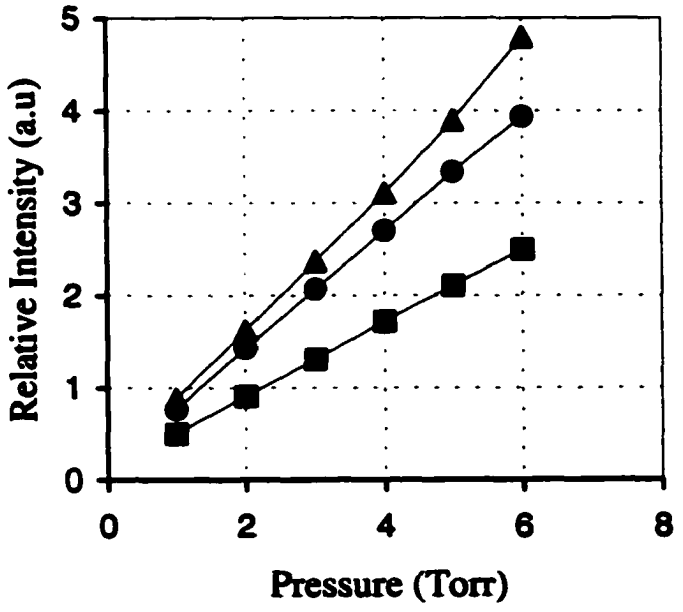

(b) Electron Emission current, I_C = 1.5 mA.

FIG. 48. QMS relative sensitivity of CO_2, O_2, and CO:
▲, 44 *m/e* (CO_2); ■, 32 *m/e* (O_2); ●, 28 *m/e* (CO).
The lines connected data points are use only to guide eyes.

3.4.2 Gas Composition Results and Discussion

In Fig. 49 to Fig. 51, the gas composition is shown as a function of power density at various discharge pressures, p and discharge gap D. In this work, we approximated the discharge power density as the total input power divided by the product of electrode area and electrode gap (i.e. discharge volume). Note that this assumes a total input power distributed uniformly over the whole range of discharge gap, D. The measurements were performed at two different gap lengths, D = 6.5 mm and D = 8.0 mm. In the first series of measurements, the power electrode was not enveloped by a dielectric layer, and no water trap was installed at the inlet gas tube. In the discharge power range of this experiment, between 40% and 50% of CO_2 was dissociated into CO and O and approximately an equivalent amount of CO was detected. The amount of O_2 was found to be nearly a half of CO. This was expected since every one mole of CO_2 dissociates into one mole of CO and one half mole of molecular oxygen.

The y-axis error bars are the statistical error of the measurements (e.g., a hit or miss of ionization electrons with neutral molecules inside the QMS) using the experiment standard deviation and the x-axis error bars are the uncertainty in power measurement. The RF noise effect was eliminated by observing the change of *m/e* intensities when discharge was activated and deactivated with the leak valve in a completely closed position. In addition, the pressure increase during discharge, due to CO_2 decomposition, was eliminated by taking into account the linear pressure dependence of these peaks at a fixed electron current emission of the QMS. Figures 49 to 51 show that CO_2 decomposition increases with power density up to 60%. We note that both electron density and electron temperature increase proportionally with power density (see Fig. 25 and Fig. 26), and that the electron impact is the main CO_2 decomposition mechanism (e.g., reaction (R1) in Section 2.2). Therefore, more CO_2 molecules are dissociated at higher power density. In addition, at given RF power, the percentage of CO_2 dissociation increases slightly with pressure. This is probably the result of an increase in the number density of CO_2 molecules. We have seen that the CO_2 decomposition rate depended on both electron density and CO_2 concentration (Section 2.3.2). If the total number of electrons does not change significantly with

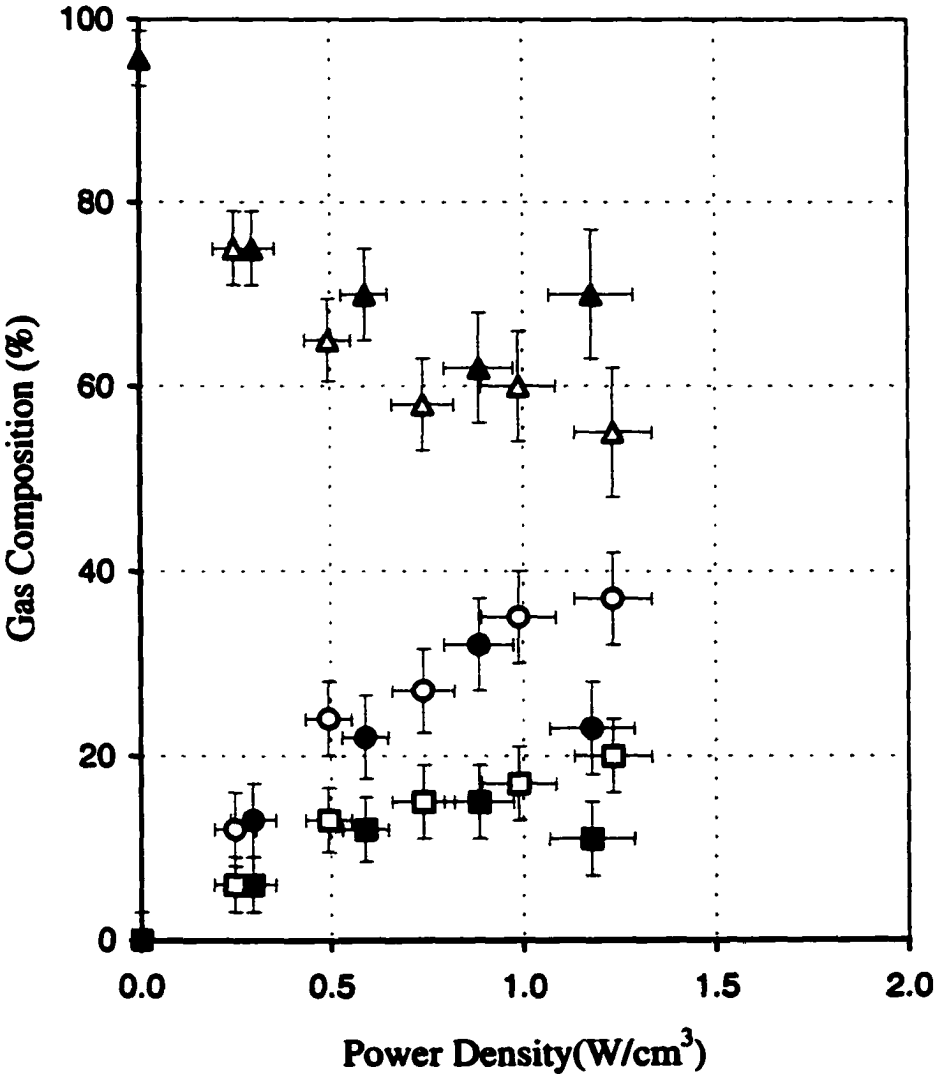

FIG. 49. Gas composition in RF discharge at p = 4.0 Torr as a function of power density. Solid and open symbols are discharge with gaps D = 6.5 mm and D = 8.0 mm, respectively: ▲,△: 44 *m/e* (CO_2); ■,□: 32 *m/e* (O_2); ●,○: 28 *m/e* (CO).

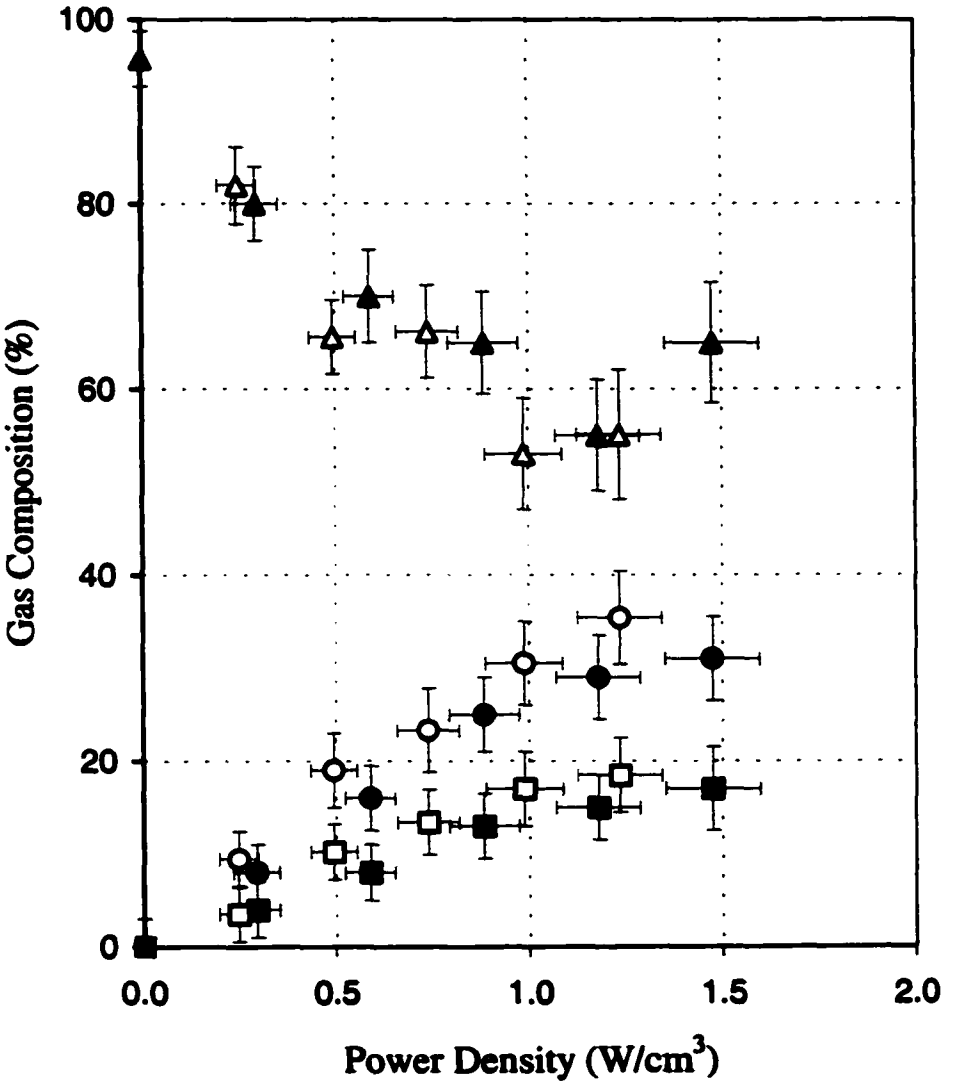

FIG. 50. Gas composition in RF discharge at p = 5.0 Torr as a function of power density. Symbols are the same as in Fig. 49.

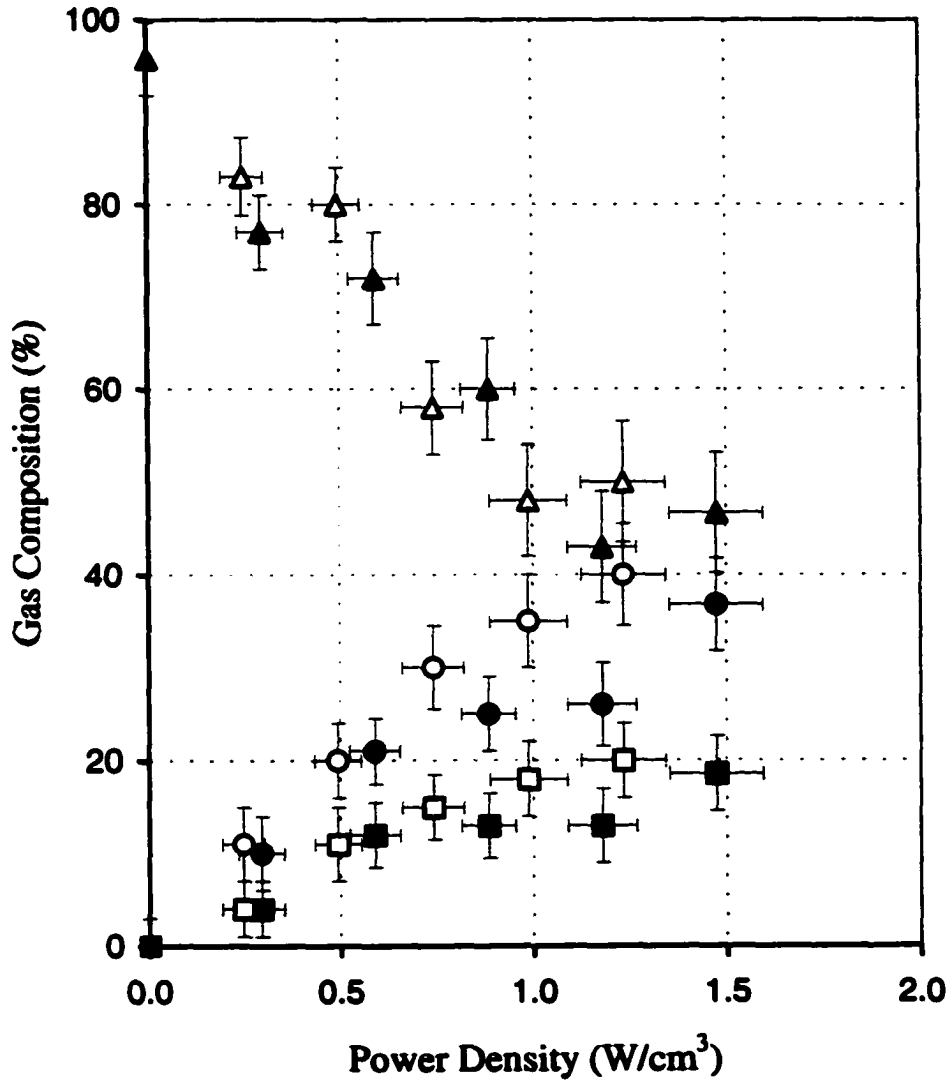

FIG. 51. Gas composition in RF discharge at p = 6.0 Torr as a function of power density. Symbols are the same as in Fig. 49.

pressure (see Fig. 26), the rate of CO_2 decomposition then depends on the CO_2 concentration in the discharge. Note that at lower pressure and higher power, CO_2 decomposition reaches a minimum and reverse its trend. A possible reason for this observation is the edge effect, which we described in Section 3.3. In this case, discharge is no longer confined between electrodes but it extends around the electrode edges. As a result, the discharge volume increases by several cubic centimeters, and the actual average power density will be smaller than estimated. As described earlier, the edge effect could be eliminated by placing a dielectric layer around the power electrode.

A small discrepancy in gas composition measurements at two different discharge gaps was also observed; CO_2 decomposition is slightly stronger at D = 8.0 mm than that at D = 6.5 mm. The effect is more significant at higher pressure and at higher power. From the experimental observation, it is possible that full sheaths were developed in the case of the larger gap. As the gap increased, there are more "tail" electrons forming near the sheath region, which are capable of dissociating the CO_2 (e.g., T_e ~ 7.0 eV) present in the discharge. As a result, more CO_2 molecules are dissociated. However, this is only the case when the reduced field distribution does not change significantly.

In order to improve CO_2 decomposition (to become more effective at higher power densities), a dielectric shield was placed around the power electrode as we did in Section 3.3. In addition, we found the amount of CO_2 decomposed into CO and O is much less than what we expected. A suspected cause is the water effect in the MSG mixture. OH radicals can easily recombine with CO to reform CO_2 (e.g., Reaction (R10) in Section 2.3.3). As we mentioned in Section 2.3.3, OH radicals in concentrations as low as 50 ppm can reduce CO_2 decomposition by as much as 40 to 50%. In order to reduce the water effect, the discharge chamber was baked at 300 to 350 °C for at least a day. In addition, a water trap was installed at the inlet gas line where a tube section was cooled below the water freezing point by immersion in dry ice. Figure 52 demonstrates the effect of water fraction in the system with an MSG pressure of 5 Torr. It was found that the use of the water trap reduced water vapor concentration by as much as 70% in comparison to the case without the trap. Furthermore, the measurements also show about 30% less water loss discharge, which is possibly due to the OH going to a recombination process with CO to form CO_2. Mass spectra of the gas

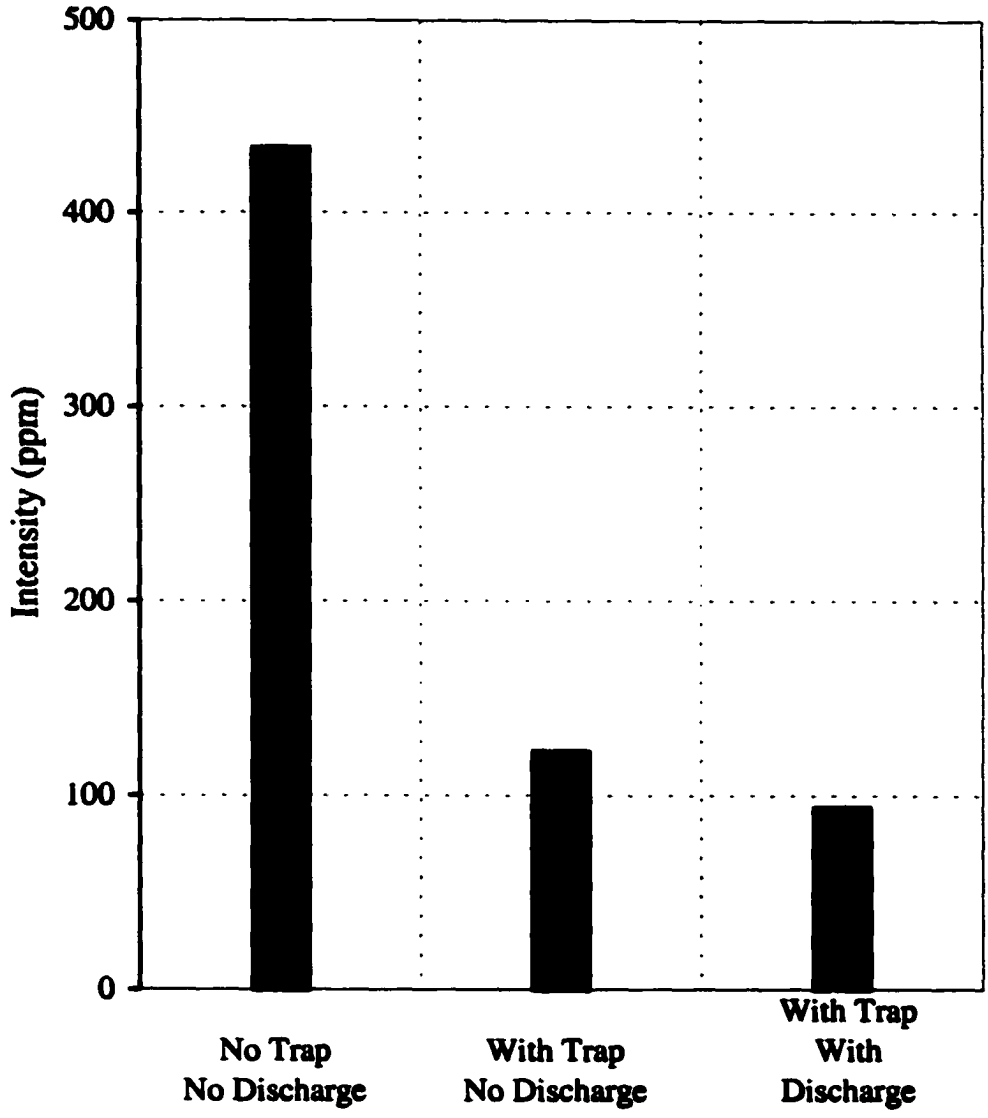

FIG. 52. Water trace concentration in MSG at pressure $p = 5$ Torr and power $P = 5.0$ W.

composition after discharge were obtained to confirm the effect of water vapor. Figures 53 and 54 illustrate gas composition measurements at various power densities with the installation of the water trap. The remaining CO_2 was reduced to as low as 25% from the initial MSG of 95.7%. At the same time the percentage of CO and O were observed to increase. There were no significant differences between two operation pressures, p = 4.0 Torr, and p = 5.0 Torr. Compared with results without the water trap (Fig. 49 to Fig. 51) at the same power and pressure range, more CO_2 is decomposed at lower power density. Therefore, the effective power to decompose CO_2 into CO and O_2 in the discharge is increased significantly.

Gas composition measurements were necessary to verify the validity of our plasma chemistry model developed in Section 2.3. These results showed reasonable agreement with our model (e.g., Fig. 13). Full CO_2 decomposition could be achieved if we could reduce further the presence of OH in the system. Furthermore, the elimination of edge effects makes the discharge more effective in the higher power range.

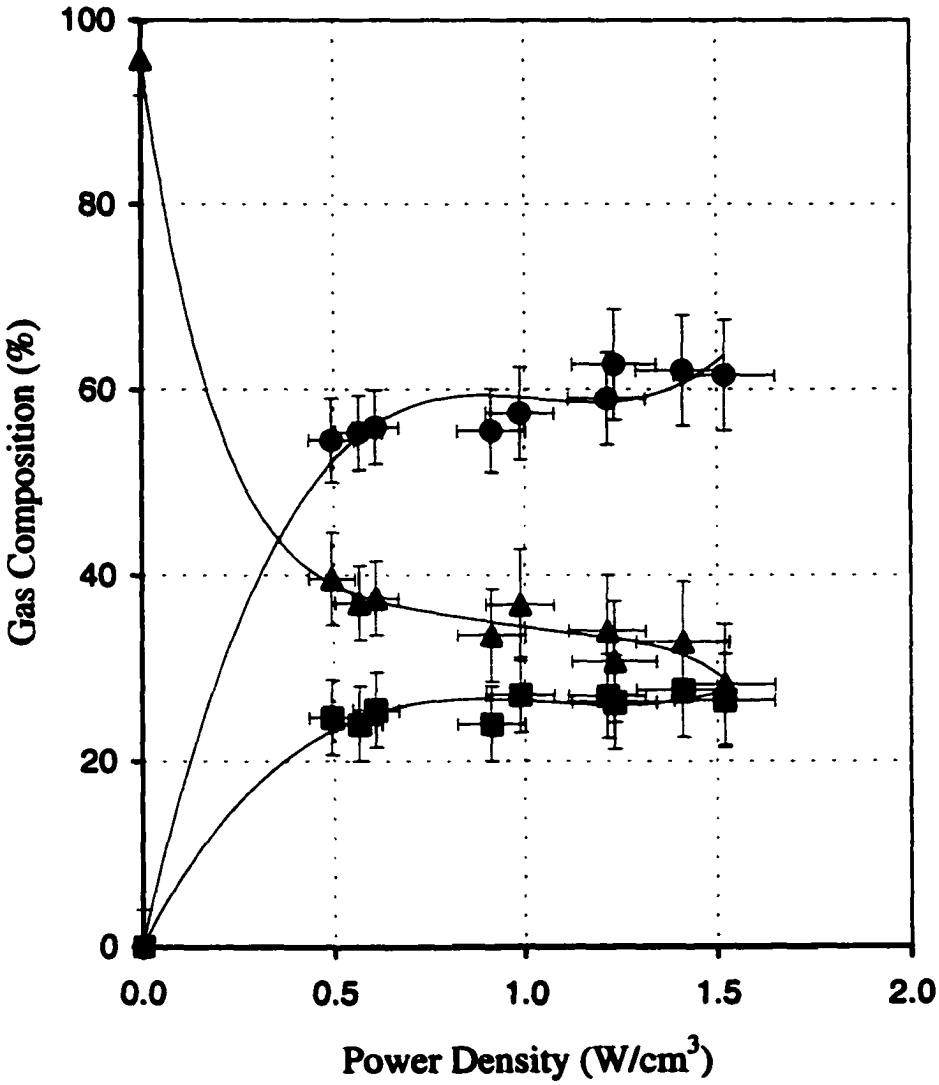

FIG. 53. Gas composition in RF discharge at p = 4.0 Torr with the addition of a dielectric layer around power electrode and a water trap as a function of power density: ▲, 44 *m/e* (CO_2); ■, 32 *m/e* (O_2); ●, 28 *m/e* (CO). The solid lines represent a smooth connection between the data points and use to guide the eyes.

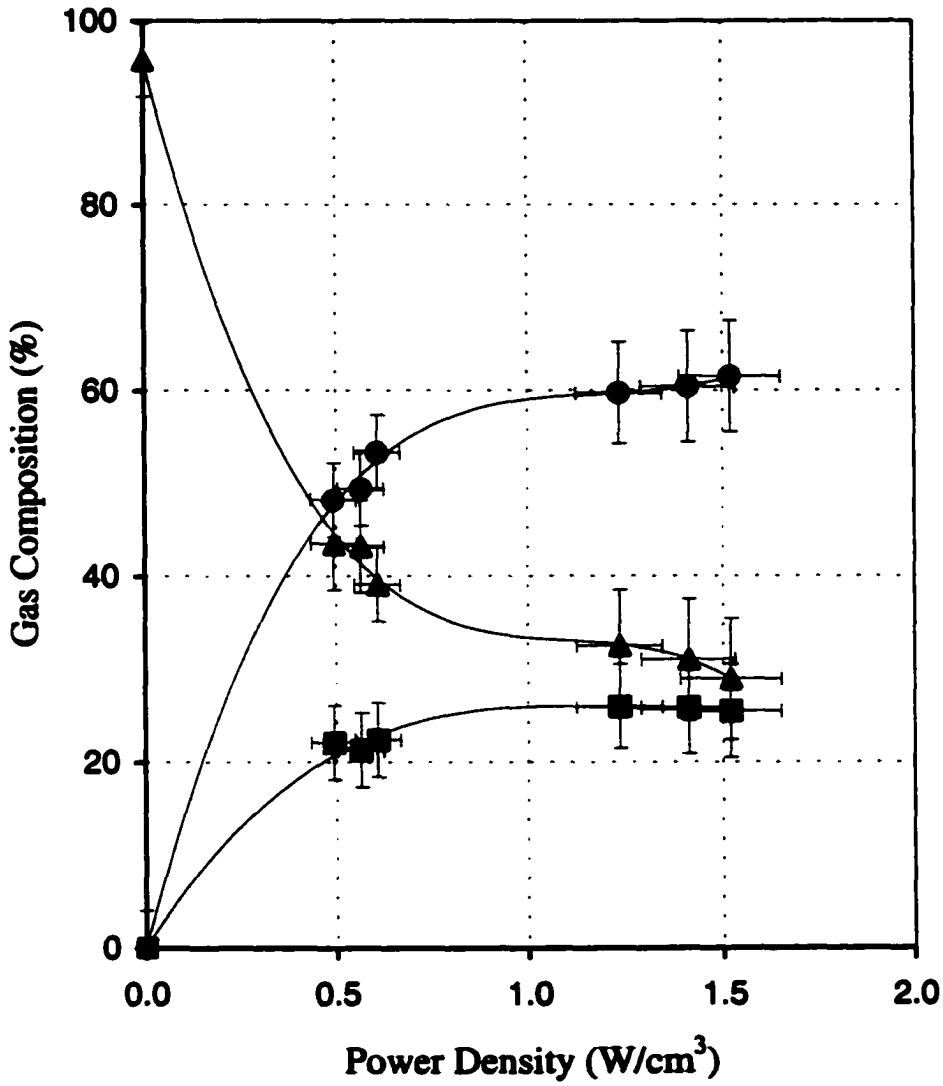

FIG. 54. Gas composition in RF discharge at p = 5.0 Torr with the addition of a dielectric layer around power electrode and a water trap as a function of power density. Symbols are the same as in Fig. 53. The solid lines represent a smooth connection between the data points and use to guide the eyes.

Section 4
RESULTS AND DISCUSSION

4.1 Decomposition of CO_2 in CCRF Discharge

The rate of CO_2 decomposition in the discharge depends on many parameters. It is most directly influenced by the electron density, N_e, the rate coefficient for electron impact dissociation k_{CO_2} (see Eq. (7)), and the initial CO_2 concentration $[CO_2]_o$. Within these parameters, the first two depend explicitly on the total power or power density (P) input to the system. They also depend implicitly on the reduced electric field (E/N) and the mean electron temperature (T_e). The last parameter $[CO_2]_o$ is defined by discharge pressure and temperature. The measured values of E/N, N_e, and T_e are compared with the theoretical results (see Section 2). These parameters are used to obtain the CO_2 dissociation rate. Finally, we discuss the steady state solution of CO_2 decomposition obtained from the model and experiment.

Reduced electric field is one of the fundamental parameters of the discharge model. In Section 2, we have seen that the mean electron temperature is a function of E/N (see Fig. 6). In addition, electron density in the center of the discharge as well as the electron density distribution can be determined from the reduced electric field distribution (see Fig. 14 and Fig. 15). In order to justify the values of E/N obtained from the model, the boundary conditions used in the model should be consistent with the actual experimental conditions and the given values of discharge parameters, such as discharge power density (P), pressure (p), temperature (T), and gap length (D). Instead of using direct boundary condition $\bar{E}$ (time averaged electric field) at the electrodes, we applied an intermediate boundary condition $\bar{V}$ (time averaged potential), which is proportional to discharge power and impedance. $\bar{E}$ was verified by integrating over the discharge gap (D), requiring that the integral is equal to $\bar{V}$. E/N was then obtained by dividing $\bar{E}$ with gas density N known from p and T. The axial distribution of E/N

obtained from the model and from experiments at the discharge conditions: P = 1.0 W/cm^3, p = 5.0 Torr, T = 400 K, and D = 6.5 mm is given in Fig. 55.

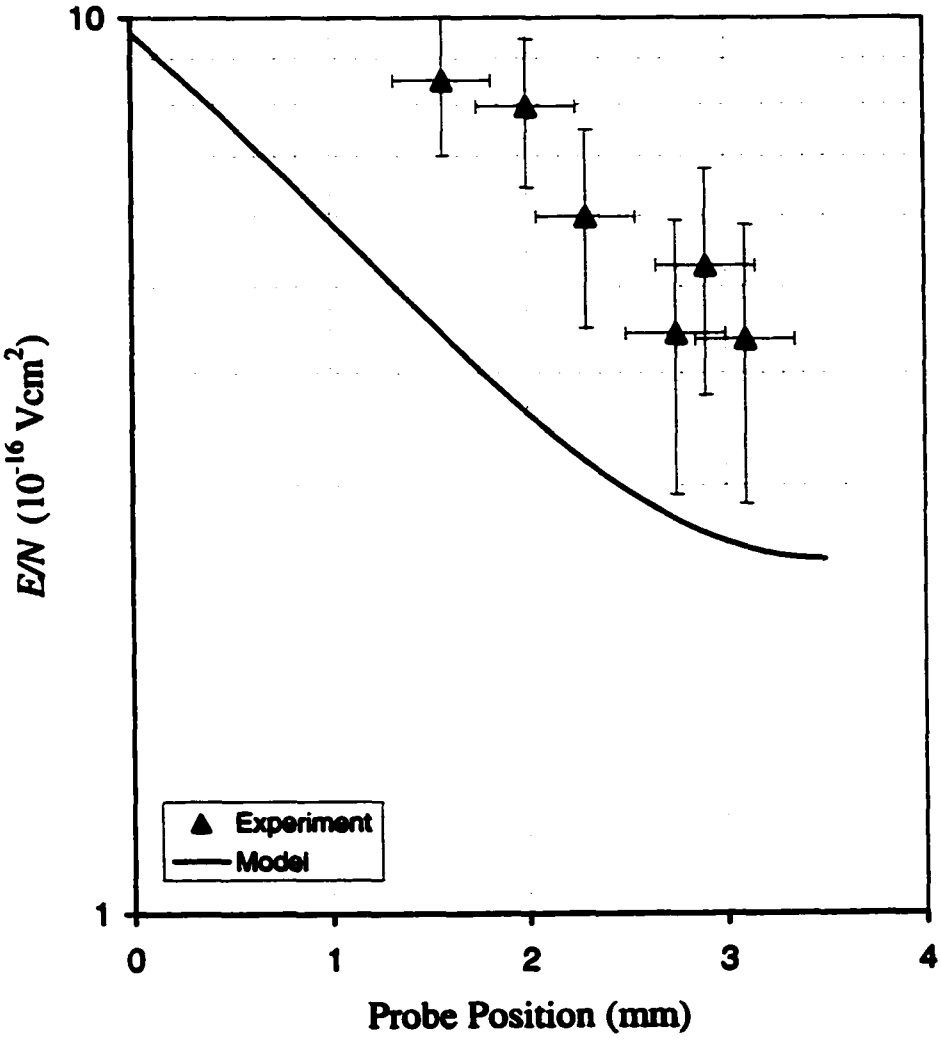

FIG. 55. Axial distribution of experimental and calculated reduced electric field, *E/N*.

The experimental and the calculated values of *E/N* show a reasonable agreement at the center of the discharge and they have the same increasing trend toward the electrode. In addition, the experimental values of *E/N* are higher and have a steeper slope than the theoretical values. One of the possible reasons for this discrepancy is the existence of capacitive coupling between the Langmuir probe and the electrode. The probe potential is distorted when it gets closer to the electrode. It results in larger measured values of the potential and the field. Another possible source of the discrepancy is due to the simplification of the present discharge model by neglecting electron diffusion to the electrodes and the electron loss process due to gas attachment. The depletion of electron density near electrodes results in larger values of *E/N*. Finally, the phase shift due to impedance mismatch between the RF source and the discharge chamber was not considered in the model, likely resulting in smaller theoretical values. For example, a phase shift φ exists between applied voltage $\overline{V}$ and discharge current $\overline{I}$. Then the time averaged power, $\overline{P}$, is proportional to $\overline{V}$, $\overline{I}$ and $cos\varphi$ ($\overline{P} = \overline{VI}cos\varphi$ or $\overline{P} = \overline{V^2}cos\varphi / Z$ with Z the discharge impedance). Therefore, $\overline{V}$ is larger when the phase shift is larger. In short, the actual *E/N* of the discharge is likely to be between the measured values (upper limit) and the theoretical *E/N* (lower limit).

Valuable information about time averaged electron density, N_e, in the discharge can be obtained from the model when compared with the experimental results. The axial distribution of N_e measured by the Langmuir probe at $P = 0.3$ W/cm^3, $D = 6.5$ mm, $p = 5.0$ Torr, and $T \sim 300$ to 400 K is shown in Fig. 56 compared with N_e obtained from the model for the same discharge conditions. The model predicts, successfully, the inverted parabolic shape of N_e with a maximum at the discharge center. The model and experimental results for N_e at the discharge center are in a good agreement, but some discrepancies are present. First, the peak position in the measured N_e is shifted toward the power electrode. A possible interpretation could be found in the existence of a non-symmetrical discharge configuration with one electrode (e.g., power electrode) having a higher time averaged potential. As a result, the probe "sees" more electrons closer to the power electrode over every cycle of the oscillatory field. Second, the measured N_e near the electrodes were lower than those predicted by the model. This effect could be due to

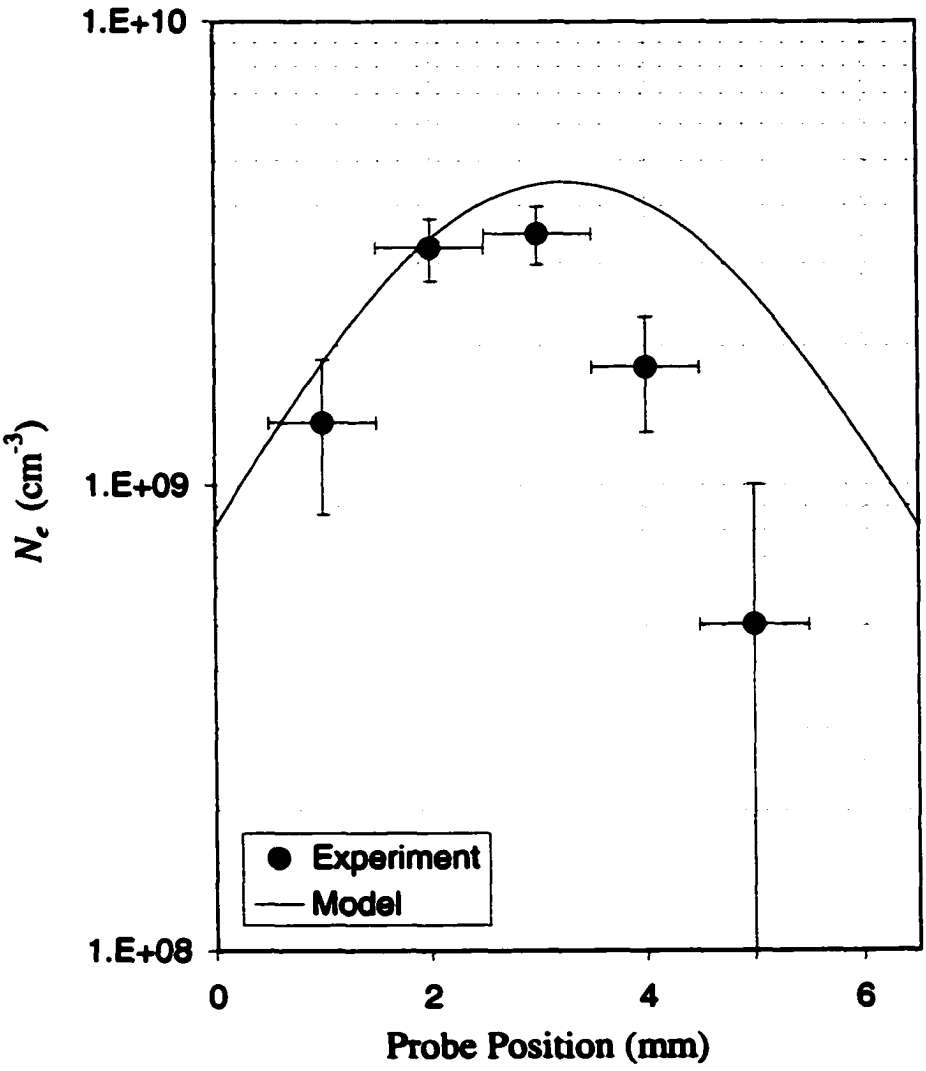

FIG. 56. Axial distribution of experimental and calculated electron density, N_e.

the significant diffusion of electrons to the bare electrodes (e.g., DC bias current) and was not taken into account in the present model as mentioned in the previous paragraph. The explanation is consistent with measurements of the large electric field near electrodes.

Comparison of measured and theoretical N_e values established the validity of our present model. The model can be applied to predict quantitatively the effect of various discharge conditions, such as power, pressure and temperature as well as the parameters that describe the characteristics of CCRF discharge such as E/N, N_+ and N_e.

It is known that when the applied power does not change significantly across the discharge gap, the voltage within the sheath can vary noticeably. However, the voltage and the field at the discharge center are not likely to change significantly. Therefore, with the lower density of $P \sim 0.5$ W/cm^3, the reduced electric field E/N could be the same as in the previous case, about 4 – 5x10^{-16} Vcm^2. According to Fig. 25, the corresponding measured T_e is about 5.0 – 5.5 eV which is between two and two and a half times the theoretical T_e (see Fig. 6). One explanation for the discrepancy is due to an intrinsic characteristic of the Langmuir probe. First, T_e obtained by the probe represents a Maxwellian temperature that results from the probe theory in which it is assumed that electrons have a Maxwellian distribution. However, this assumption is not exactly true since it is well known that the electron energy distribution (EEDF) in this type of discharge is non-Maxwellian distribution (Fig. 4 and Fig. 5). Second, T_e obtained by the probe can be overestimated due to the nature of the floating probe. Since the probe potential is floating, there is always a negative sheath of electrons surrounding the probe which prevents slow electrons from reaching the probe surface. As a result, the probe tends to collect the "tail" electrons in the EEDF and the measured T_e is likely higher than the actual T_e. On the other hand, the theoretical T_e was obtained by averaging the EEDF over the whole energy range (see Eq. (4)). The averaging process took into account the portion of slow electrons (i.e. categorize as $\varepsilon < 1.0$ eV), which is also the most populated portion in the EEDF and, unfortunately, is undetectable by the Langmuir probe. As a result, the measured T_e is always larger than the theoretical T_e. To demonstrate this, we use Fig. 57 to explain the above discrepancy. It shows an EEDF in MSG discharge at E/N of 6.0x10^{-16} Vcm^2 and the calculated average T_e over

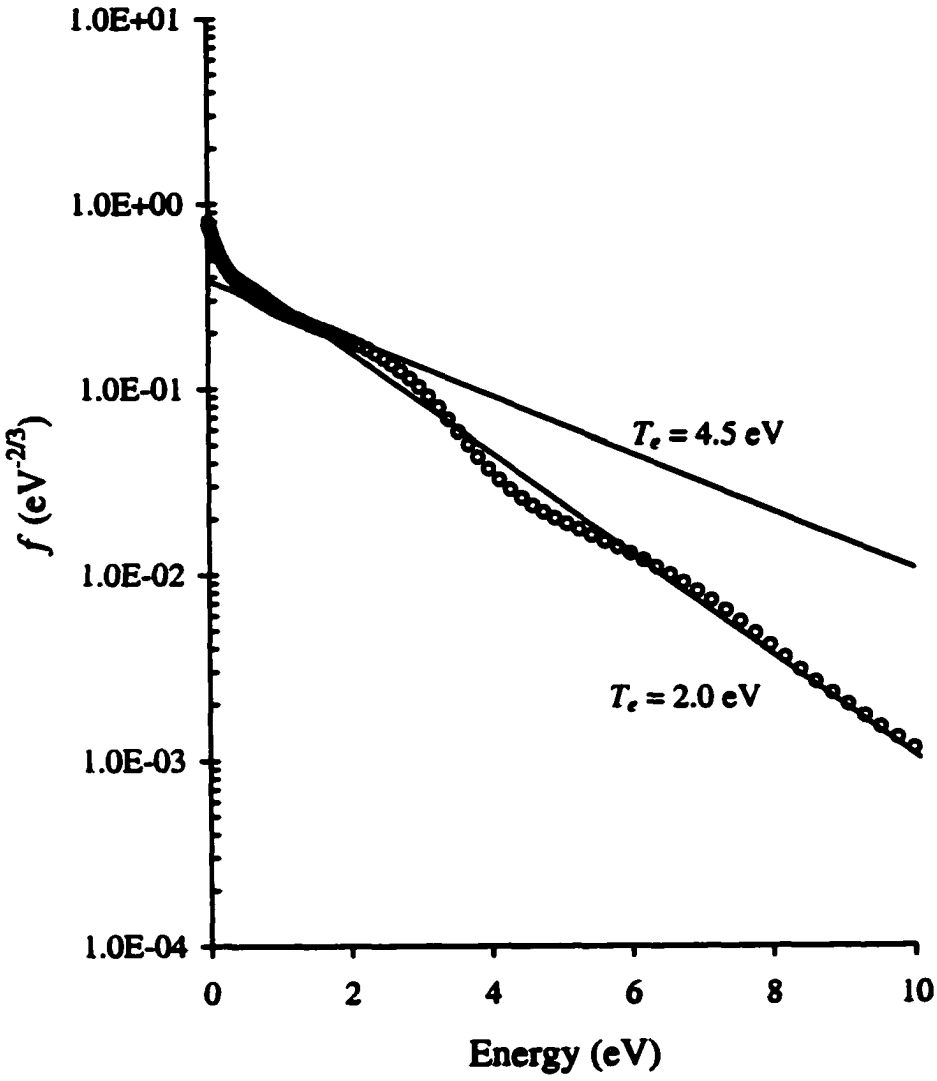

FIG. 57. Maxwellian electron temperature, T_e, of EEDF in CCRF discharge at $E/N = 6\text{x}10^{-16}$ Vcm^2.

the whole energy range. The obtained T_e is about 2.0 eV. Now consider a plateau of EEDF which well represents a Maxwellian distribution and note that the plateau is also the second most populated section of electrons in EEDF. T_e obtained in this plateau is 4.5 eV. This clearly shows that the Maxwellian temperature here is much larger than the average electron temperature. Therefore, the measured T_e from the Langmuir probe could be as large as twice the calculated T_e from the model or the actual T_e.

For the same reason, the actual electron density N_e in the discharge can be slightly higher than the results measured via Langmuir probe. By excluding the portion of slow electrons due to the floating condition, the probes receive a smaller number of electrons out of the total number of electrons in a unit volume of discharge. The fraction of slow electrons excluded from coming to the probe is proportional to the difference between the floating potential and the plasma potential.

The knowledge of E/N, N_e, T_e and initial CO_2 concentration $[CO_2]_o$ at various discharge conditions is necessary to predict the CO_2 decomposition rate. Theoretically, the full decomposition of CO_2 could be achieved at a very low applied RF power density (e.g., ~ 0.5 W/cm^3, Fig. 8). However, CO_2 decomposition can be limited by the presence of a small amount of water. In practice, concentrations of water, measuring not more than a few decades of ppm in the system is unavoidable, unless the experiment is performed in a high vacuum or ultrahigh vacuum system all the time. An alternate way to check the validity of our gas kinetic model is to incorporate the water effect into it (Section 2.3.3). A comparison was made between model and experiment in the steady state gas composition at various OH radical concentration levels. The $[OH]$ applied to the model was based on the measurements of water traces in the system (see Fig. 52) and noting that the OH radical concentration is about 30% of the water amount. Hence, $[OH]$ are estimated to be as much as 100-120 ppm and 30 – 50 ppm without and with a cold trap, respectively. In the present model, we assumed that OH radical concentration is constant over the applied power range. The modeled and experimental results are given in Fig. 58 and Fig. 59 for MSG RF discharge at the same conditions. Note that the gas composition was measured at afterglow conditions that allowed the dominant CO_2 recombination processes to take place at low electron density (e.g., no discharge). The estimated time of flight for the molecules before they enter the mass spectrometer is

several seconds. The model results here also included this recombination process and allowed the time evolution to obtain a set of steady state solutions. In addition, the forming of oxygen molecules was included through the recombination of atomic oxygen at the wall or through a third body molecule. Good agreement between the model and experimental results was obtained. The results confirmed the validity of our gas kinetic model.

We can conclude this discussion with the statement that our kinetic model and our experimental results are in good agreement. The approach to use a reduced number of reactions in the kinetic model has proven to be successful. Systematic errors in the diagnostic methods used do not affect experimental data too much, and we are able to conclude that they confirm both qualitatively and quantitatively the calculated data.

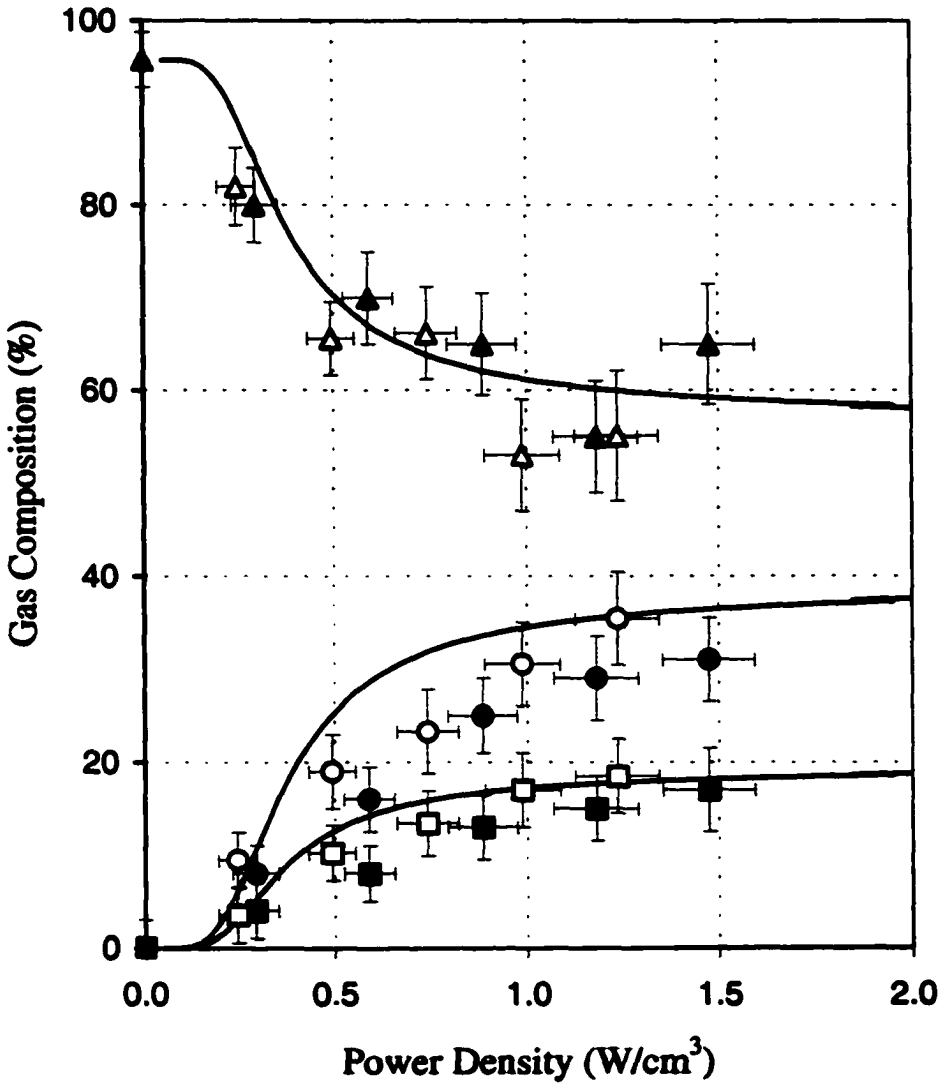

FIG. 58. Composition of MSG discharge at $p = 5.0$ Torr. Full lines are calculated data ($[OH] = 100$ ppm). Experimental results (without water trap) are obtained at discharge gap $D = 6.5$ mm and $D = 8.0$ mm (solid and open symbols, respectively). ▲,△: 44 *m/e* (CO_2); ■,□: 32 *m/e* (O_2); ●,○: 28 *m/e* (CO).

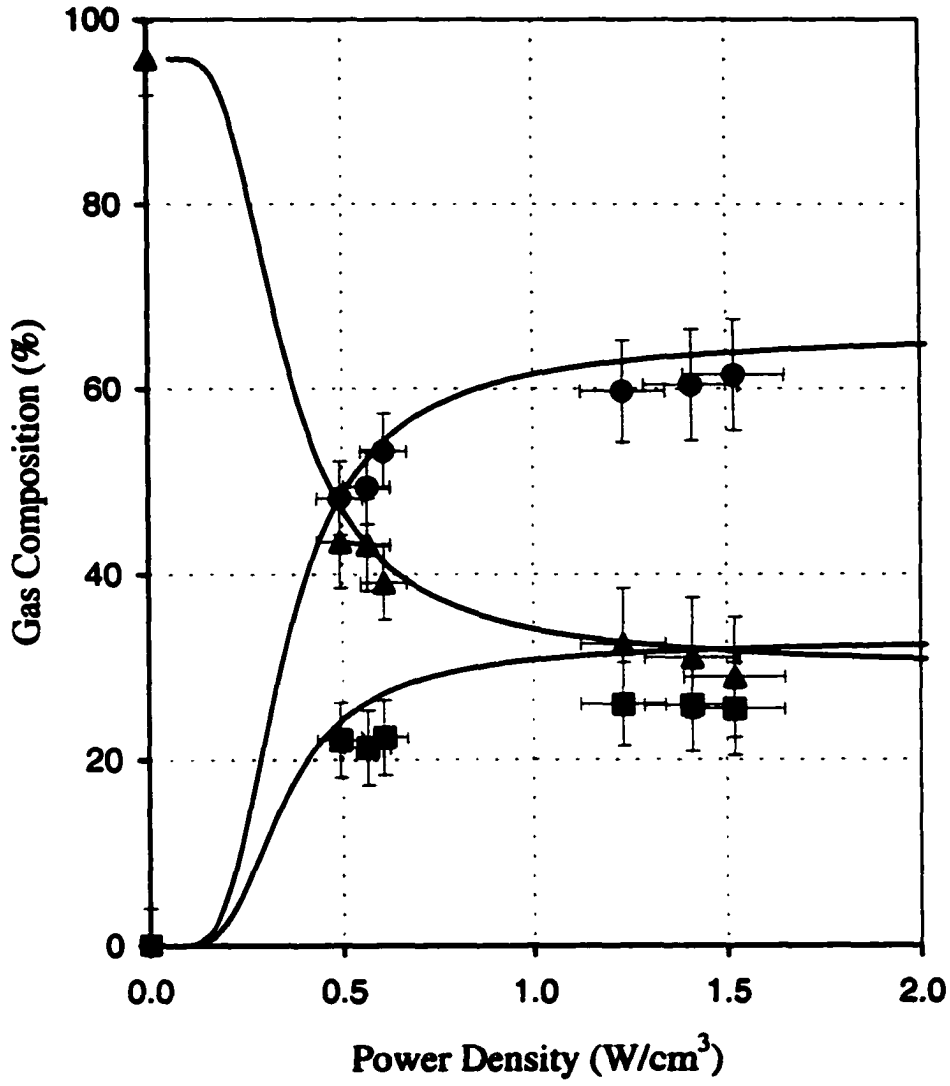

FIG. 59. Composition of MSG discharge at p = 5.0 Torr. Full lines are calculated data ([*OH*] = 30 ppm). Experimental results (with water trap) are obtained at discharge gap D = 6.5 mm and D = 8.0 mm (solid and open symbols, respectively). ▲,△: 44 *m/e* (CO_2); ■,□: 32 *m/e* (O_2); ●,○: 28 *m/e* (CO).

4.2 Application to Oxygen Production at Martian Atmosphere

The study of CO_2 decomposition in CCRF discharge can be applied in many practical works, and one possible application is oxygen production on Mars. As early as 1978, Ash et al [56] suggested the concept of producing propellant fuel from Martian resources. *In situ* resource utilization (ISRU) is considered the most important aspect for future Mars missions, and the direct oxygen production from Mars atmosphere is a major part of ISRU. The earth launch mass could be reduced significantly by using the oxygen produced on Mars as rocket propellant for the return trip to earth. An oxygen production facility on Mars could even be supported for future Mars human exploration. One present technique is using solid oxide electrolysis cells with yttria-stabilized zirconia (YSZ) medium to generate oxygen on Mars [57]. The technique is based on a combination of thermal dissociation and electrocatalysis to liberate oxygen from CO_2 in the Martian atmosphere. However, the technique requires rather high temperatures above 1000 K and high compression pressures, and its overall oxygen production efficiency is still not optimal. Recent studies [58-62] showed CCRF glow discharge with a silver membrane permeation technique could be an effective way to generate the oxygen on Mars. In addition, Vuskovic et al. [62] suggested the technique could also be used for filtering the micron-sized dust particles in the Mars atmosphere. These studies have been funded by NASA and pursued at Old Dominion University.

The experimental set-up of oxygen extraction from Martian gas is very much the same as in Fig. 18 except with some modification to the discharge cell. Figure 60 shows a schematic of a discharge cell in the oxygen extraction experiment. One of the electrodes was a membrane made of silver with various thicknesses from 300 – 100 μm. The membrane temperature can be varied by a heater and monitored by a thermocouple. The CCRF glow discharge with pure CO_2 or Martian Simulant Gas (MSG) was generated in front of the membrane with similar discharge conditions that have been described throughout this work. O_2 at the other side of membrane (or downstream) was monitored using a quadrupole mass spectrometer.

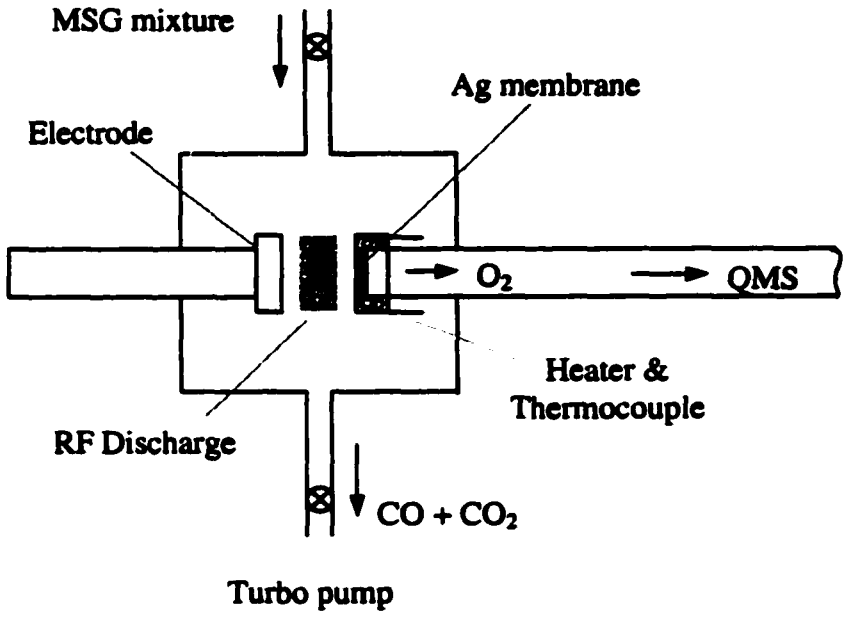

FIG. 60. Schematic of oxygen extraction cell with CCRF glow discharge.

The process of oxygen production on Mars using a CCRF glow discharge actually involves several steps. First, CO_2 dissociation occurs through a multi-electron molecule collision in an oscillatory field (e.g., RF field). Full dissociation of CO_2 could be achieved at 0.5 W/cm^3 (Section 2), and roughly one mole of CO and one mole of O are produced for every mole of CO_2.

Second, the adsorption of atomic oxygen on the membrane surface in the upstream region is relatively large. Our experimental results have indicated that a relatively dense and thin atomic oxygen layer was formed on the silver surface [62]. The formation of the layer is assumed due to the near unity sticking coefficient of atomic oxygen to the silver surface [61]. Some recent studies [63-64] suggested a strong dissociation of oxygen molecules on a Ag surface at a temperature close to 900 K before

the oxygen adsorption process. The large concentration of atomic oxygen at the surface in turn increases the rate of oxygen permeation through the membrane.

Finally, atomic oxygen recombines to form oxygen molecules on the other side of membrane or in the down stream region. The rate of that process is fast and only oxygen molecules are detected by the mass spectrometer.

The transport of oxygen through the membrane follows the diffusion law [61-62]

$$J_O = \frac{D_O \Delta n_O}{d}, \tag{30}$$

where D_O is the oxygen diffusivity in silver, Δn_O is the difference between upstream and downstream oxygen densities, and d is the thickness of the permeation membrane. D_O usually depends on bulk characteristics of the silver and depends on temperature. It was obtained from experiments by measuring the oxygen flux decay after the discharge was interrupted. The oxygen diffusivity through a silver membrane at various thicknesses and temperatures is shown in Fig. 61. The oxygen diffusivity increases exponentially with the temperature and is not significantly different at different membrane thicknesses.

The above relationship implies that the increase of oxygen flux in the downstream region can be obtained by either increasing D_O and Δn_O or decreasing d, the membrane thickness. The maximum oxygen flux then can be achieved from the optimum of these parameters. D_O could be increased by increasing the temperature; however, high temperatures result in smaller oxygen concentrations at the membrane surface. In the DC glow discharge, the oxygen concentration was found to have a maximum at a membrane temperature of 450°C [62]. For RF glow discharge, we found the upstream concentration was about 5×10^{18} cm^{-3} at this temperature. Finally, the reduction of membrane thickness, d, can boost significantly the oxygen flux. Figure 62 demonstrates the effect of the membrane thickness on the oxygen flux. The oxygen flux measurements were found to be inversely proportional to the membrane thickness. Theoretically, an oxygen flux on the order of 10^{16} $cm^{-2}s^{-1}$ can be achieved easily with a 1 μm thin silver membrane.

The power efficiency of oxygen production with RF glow discharge is estimated to be as much as 25% for current discharge conditions. This high power efficiency is due to the effective CO_2 dissociation by electron impact in RF glow discharge in

comparison to thermal dissociation or even DC glow discharge. Figure 63 gives an example of measured oxygen flux as a function of RF power density of MSG mixture with a 0.33 mm thick silver membrane at 500°C. The optimum RF power in this case is about 0.5 W/cm^3 where the flux rate reaches a maximum.

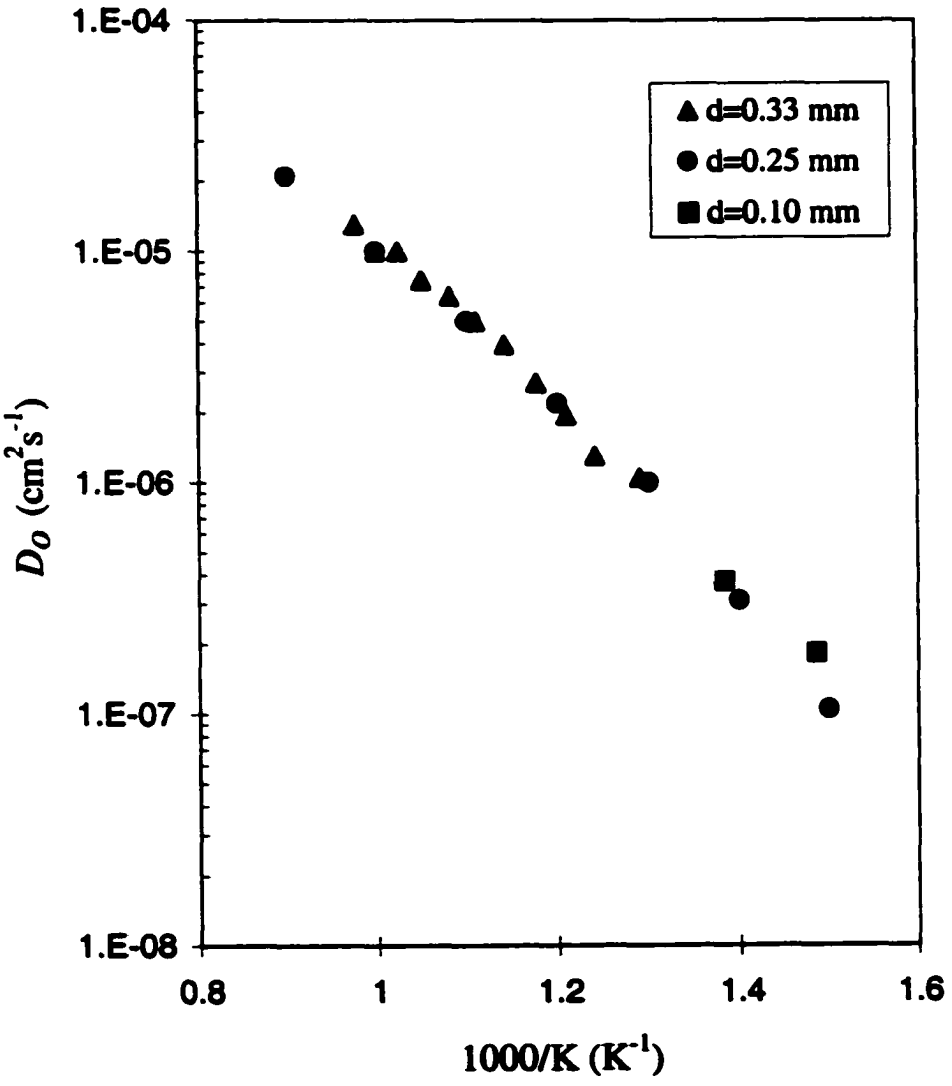

FIG. 61. Diffusivity of oxygen as a function of temperature at various silver membrane thickness.

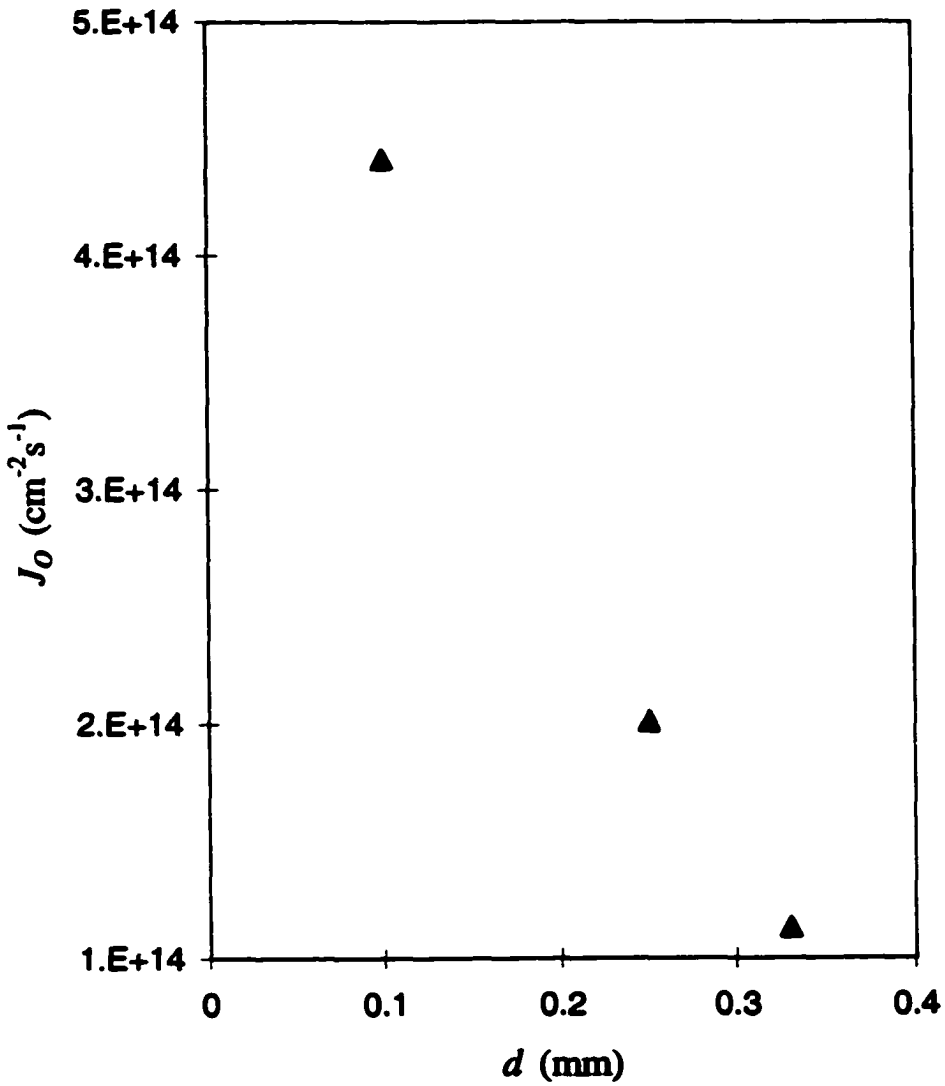

FIG. 62. Oxygen flux as a function of membrane thickness.

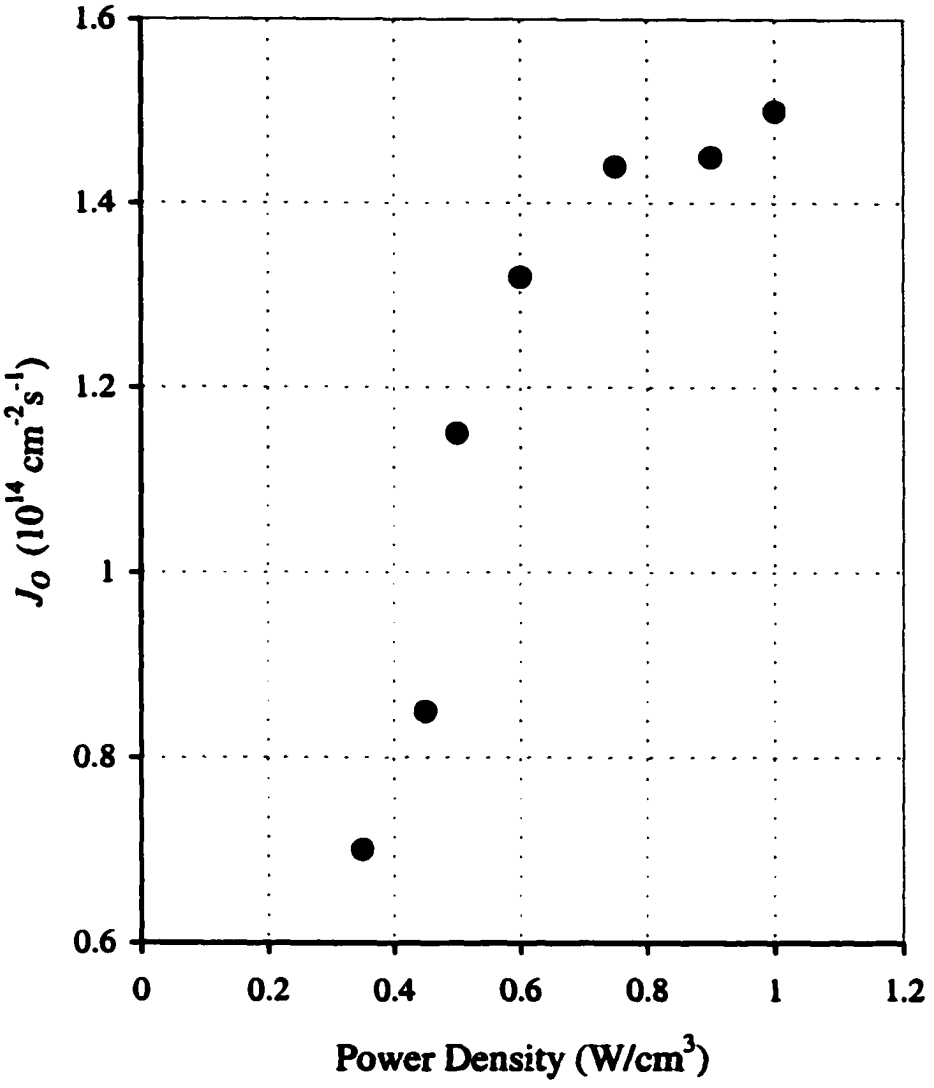

FIG. 63. Oxygen flux as a function of power density.

Section 5
CONCLUSIONS

Decomposition of CO_2 in a capacitively coupled radio frequency (CCRF) discharge was studied in the intermediate pressure and low power regimes. The main mechanism for CO_2 decomposition in CCRF discharge was an electron impact dissociation process with a threshold energy around 7.0 eV. The CO_2 decomposition rate is a function of the dissociation and recombination rate coefficients, mean electron density and temperature, and CO_2 density. CO_2 and O_2 dissociation rate coefficients, k_{CO_2}, and k_{O_2}, respectively, were calculated based on the electron energy distribution (EED) in the discharge, using the electron dissociation cross section of CO_2 and O_2. EED was obtained by solving the electron energy balance equation (e.g., Boltzmann equation) in the mixture (e.g., Martian Simulant Gas mixture). Rate coefficients k_{CO_2} and k_{O_2} were found to increase dramatically with reduced electric field strength, *E/N*, by as much as three orders of magnitude when *E/N* varies from 3 to 6×10^{-16} Vcm^2. This variation corresponds to a change in discharge power density from 0.3 to 1.0 W/cm^3 and a change in pressure from 3 to 6 Torr. A gas kinetic model which was based on major collision processes in the discharge including the electron impact dissociation rate coefficients k_{CO_2} and k_{O_2} has shown the possibility of obtaining full CO_2 decomposition under these discharge conditions. The model included the effect of trace concentrations of water vapor. The existence of OH radicals was confirmed as a factor that is able to impose a limit on CO_2 decomposition, and this effect was observed directly in the experiment. Experimental and model results have agreement for the final steady-state gas composition within an error of less than 5%.

Fundamental discharge parameters such as the mean electron energy, T_e, mean electron density, N_e, and reduced electric field *E/N* were obtained by Langmuir probe and showed qualitative agreement with model results.

High experimental values of electron temperature, T_e, compared to theoretical values, are due to the natural characteristics of the Langmuir probe which are based on

assumptions which are only approximately true, such as a Maxwellian distribution of electrons and the negative floating potential of the probe.

The axial distribution of electron density has a nearly parabolic shape with a maximum at the center of the discharge, decreasing toward the electrodes. The measured axial distribution has shown an agreement within an error margin of 50% with the results of the model at the discharge center, which is quite reasonable for electron density values. Both T_e and N_e, at discharge center, increase with power density. At a discharge power density of less than 1.0 W/cm^3 and a MSG pressure of 4-6.0 Torr, N_e was about 3 – 5x10^9 electrons/cm^3 and T_e varied from 1 – 3 eV.

The axial distribution of the reduced electric field *E/N* was opposite to that of the electron density. It exhibited a minimum at the discharge center and increased about an order of magnitude toward the electrodes due to the formation of an charged particle sheaths in front of the electrodes. At the same discharge power and pressure, *E/N* at the center was about 3 – 6x10^{-16} Vcm^2 which corresponded to a time averaged field of 80 – 100 V/cm and a discharge current density from 5 – 10 mA/cm^2.

The gas temperature was measured precisely by evaluation of the CO rotational temperature using the transition band $B^1\Sigma^+$-$A^1\Pi$ in the CO Ångstrom system. The gas temperature was also compared with results from the thermocouple measurements. The two temperature sets have shown an agreement to within 10%. In the operating discharge conditions, the gas temperature was about 300 – 450 K and is much lower than the electron temperature (e.g., 300 K ~ 0.026 eV).

In conclusion, the agreement between the experimental and theoretical results established the validity of our gas kinetic model and the rate of CO_2 decomposition in a CCRF discharge. Due to the effective energy transfer from the field to molecules via electrons, full CO_2 decomposition can be achieved at a relatively low discharge power density of less than 0.5 W/cm^3. This study can be applied to every process where the need for power efficiency to convert CO_2 is essential. One such example is an oxygen generation facility on the planet Mars.

REFERENCES

[1] A. L. S. Smith and J. M. Austin, J. Phys. D: Appl. Phys. **7**, 314 (1974).

[2] S. Ono and S. Teii, J. Phys. D: Appl. Phys. **17**, 1999 (1984).

[3] Z. Shi, D. Wu, and R. L. Ash, SAE Paper 961598, *26th International Conference on Environmental Systems*, Monterey, California July 1996.

[4] T. Holstein, Phys. Rev. **70**, 367 (1946).

[5] E. H. Holt and R. E. Haskell, *Foundations of Plasma Dynamics* (The Macmillan Company, New York 1965).

[6] L. C. Pitchford, S. V. O'Neil, and J. R. Rumble Jr., Phys. Rev. A. **23**, 294 (1980).

[7] W. J. Goedheer, Plasma Sources Sci. Technol. **9**, 507 (2000).

[8] R. Winkler, Adv. At. Mol. Opt. Phys. **43**, 19 (2000).

[9] L. S. Frost and A. V. Phelps, Phys. Rev. **127**, 1621 (1962).

[10] D. K. Gibson, Aust. J. Phys. **23**, 683 (1970).

[11] J. J. Lowke, A. V. Phelps, and B. W. Irwin, J. Appl. Phys. **44**, 4664 (1973).

[12] R. D. Hake, Jr. and A. Phelps, Phys. Rev. **158**, 70 (1967).

[13] T. W. Shyn, W. E. Sharp, and G. R. Carignan, Phys. Rev. A **17**, 1855 (1978).

[14] D. F. Register, H. Hishinmuirta, and S. Trajmar, J. Phys. B: At. Mol. Phys. **13**, 1651 (1980).

[15] L. J. Kieffer, JILA Inf. Cen. Rep. No. 13 , University of Colorado (1973).

[16] Y. Nakamura, Auts. J. Phys. **48**, 357 (1995).

[17] M. Takekawa and Y. Itikawa, J. Phys. B: At. Mol. Opt. Phys. **29**, 4227 (1996).

[18] M. Takekawa and Y. Itikawa, J. Phys. B: At. Mol. Opt. Phys. **31**, 3245 (1998).

[19] M. Takekawa and Y. Itikawa, J. Phys. B: At. Mol. Opt. Phys. **32**, 4209 (1999).

[20] K. K. Corvin and S. J. B. Corrigan, J. Chem. Phys. **50**, 2570 (1968).

[21] D. Rapp and P. Englander-Golden, J. Chem. Phys. **43**, 1464 (1965).

[22] J. E. Land, J. Appl. Phys. **49**, 5716 (1978).

[23] A. G. Middleton, M. J. Brunger, and P. J. O. Teubner, J. Phys. B: At. Mol. Opt. Phys. **26**, 1743 (1993).

[24] Y. Itikawa, A. Ichimura, K. Onda, K. Sakimoto, K. Takayanagi, Y. Hatano, M. HayaShi, H. Nishimura, and S. Tsurubuchi, J. Phys. Chem. Ref. Data **18**, 23 (1989).

[25] Y. Itikawa, J. Phys. B: At. Mol. Opt. Phys. **33**, 253 (1994).

[26] L. S. Frost and A. V. Phelps, Phys. Rev. **136**, A1538 (1964).

[27] W. L. Nighan, Phys. Rev. A **2**, 1989 (1970).

[28] P. Capezzuto, F. Cramarossa, R. D. Agostino, and E. Molinari, J. Phys. Chem. **80**, 882 (1976).

[29] G. C. R. Williams and A. L. S. Smith, J. Appl. Phys. **18**, 335 (1985).

[30] H. Shields, A. L. S. Smith, and B. Norris, J. Phys. D: Appl. Phys. **9**, 1587 (1976).

[31] P. W. Pace and M. Lacombe, IEEE J. Quantum Electron **14**, 263 (1978).

[32] S. R. Byron and H. Apter, J. Appl. Phys. **71**, 1976 (1992).

[33] I. C. Walker, J. M. Gingell, N. J. Mason, and G. Marston, J. Phys. B: At. Mol. Opt. Phys. **29**, 4749 (1996).

[34] P. H. Wine, J. M. Nicovich, R. J. Thompson, and A. R. Ravishankara, J. Phys. Chem. **87**, 3948 (1983).

[35] R. Atkinson, D. L. Baulch, R. A. Cox, R. F. Hampson Jr., J. A. Kerr, M. J. Rossi, and J. Troe, J. Phys. Chem. Ref. Data **26**, 1329 (1997).

[36] J. E. Morgan and H. I. Schiff, J. Chem. Phys. **38**, 1495 (1963).

[37] D. A. Parkes, J. Chem. Soc. Faraday Trans. **68**, 627 (1972).

[38] W. L. Nighan and W. J. Wiegand, Phys. Rev. A. **10**, 922 (1974).

[39] H. Hokazono and H. Fujimoto, J. Appl. Phys. **62**, 1585 (1987).

[40] C. Leys, C. V. Egmond, and E. Desoppere, J. Appl. Phys. **78**, 2265 (1995).

[41] B. Eliasson, U. Kogelschatz, and P. Baessler, J. Phys. B: At. Mol. Phys. **17**, L797 (1984).

[42] D. Stelman, J. L. Moruzzi, and A. V. Phelps, J. Chem. Phys. **56**, 4183 (1972).

[43] Y. P. Raizer, M. N. Shneider, and N. A. Yatsenko, "*Radio-Frequency Capacitive Discharge*," (CRC Press, Boca Raton 1995).

[44] W. H. Hayt, Jr., *Engineering Electromagnetics* (McGraw-Hill, New York 1989).

[45] Y. P. Raizer, *Gas Discharge Physics* (Springer-Verlag, Berlin 1991).

[46] J. W. Swift, and M. J. R. Schwar, *Electrical Probes for Plasma Diagnostics* (American Elsevier Publishing Company, New York).

[47] L. Loeb, *Basic Processes of Gaseous Electronics* (University of California Press, 1961).

[48] A. Chelouah, E. Marode, G. Hartmann, and S. Achat, J. Phys. D: Appl. Phys. **27**, 940 (1994).

[49] M. A. Lieberman, and A. J. Lichtenberg, *Principles of Plasma Discharges and Materials Processing* (John Wiley & Sons New York 1994).

[50] G. Herzberg, *Molecular Spectra and Molecular Structure: Spectra of Diatomic Molecules* (D. Van Nostrand Company New York, 1950).

[51] P. H. Krupenie, *The Band Spectrum of Carbon Monoxide,* (NSRDS-NBS-5 Washington D. C., 1966).

[52] H. Hönl and F. London, Z. Physik **33**, 803 (1925).

[53] D. M. Dennison, Phys. Rev. **28**, 318 (1926).

[54] F. Reiche and H. Rademacher, Z. Physik **39**, 444 (1926).

[55] D. Rapp and P. Englander-Golder, J. Chem. Phys. **43**, 1464 (1965).

[56] R. L. Ash, W. L. Dowler, and G. Varsi, Acta Astronautica **5**, 705 (1978).

[57] K. R. Sridhar and B. T. Vaniman, SAE Paper 951737, *25th International Conference on Environmental Systems*, San Diego, California, July 1995.

[58] R. A. Outlaw, S. N. Sankaran, G. B. Hoflund, and M. R. Davidson, J. Mater. Res. **3**, 1378 (1988).

[59] R. A. Outlaw, D. Wu, M. R. Davidson, and G. B. Hoflund, J. Vac. Sci. Technol. A **10**, 1497 (1992).

[60] D. Wu, R. A. Outlaw, and R. L. Ash, J. Appl. Phys. **74**, 4990 (1993).

[61] D. Wu, Ph. D. Dissertation, "The Development of a Method to Extract High Purity Oxygen from Martian Atmosphere," Old Dominion University, August 1994.

[62] L. Vuskovic, R. L. Ash, Z. Shi, S. Popovic, and T. Dinh, J. Aerospace **106**, 1041 (1997).

[63] D. A. Butler, J. B. Sanders, A. Raukema, A. W. Kleyn, and J. M. Frenken, Sur. Sci. **375**, 141 (1996).

[64] J. Wang, W. Dai, J. Deng, X. Wei, Y. Cao, and R. Zhai, Appl. Surf. Sci. **126**, 148 (1998).

[65] A. V. Phelps, Can. J. Chem. **47**, 1783 (1969).

[66] F. Bastien, R. Haug, and M. Lecuiller, J. Chem. Phys. **72**, 105 (1975).

[67] R. E. Beverly III, Opt. Quantum Electron, **14**, 501 (1982).

[68] M. Farland et al., J. Chem. Phys. **59**, 6629 (1973).

[69] J. L. Moruzzi and A. V. Phelps, J. Chem. Phys. **45**, 4617 (1966).

[70] F. E. Niles, J. Chem. Phys. **52**, 408 ((1970).

[71] D. E. Toodle, Final Technical Report (AD-A104344), Air Force Wright Aeronautical Lab., Ohio, 1981 (unpublished).

[72] J. Thones and S. C. Kurizius, Technical Report (AD-A083222), 1979.

[73] C. L. Lin and M. T. Leu, Int. J. Chem. Kinet. **14**, 417 (1982).

[74] O. Klais, P. C. Anderson, and M. J. Kurylo, Int. J. Chem. Kinet. **12**, 469 (1980).

[75] F. Stuhl and H. Niki, J. Chem. Phys. **55**, 3943 (1971).

[76] F. C. Fehsenfeld and E. E. Ferguson, J. Chem. Phys. **61**, 3181 (1974).

APPENDIX A

LIST OF GAS REACTIONS

Dissociative attachment:	Rate coefficient	Reference
$e + CO_2 \rightarrow CO + O^-$	5×10^{-13} cm^3s^{-1}	[38]
$e + CO \rightarrow C + O^-$	3×10^{-14} cm^3s^{-1}	[38]
$e + O_2 \rightarrow O + O^-$	3×10^{-12} cm^3s^{-1}	[38]
$e + O_3 \rightarrow O^- + O_2$	1×10^{-8} cm^3s^{-1}	[32]
	1×10^{-11} cm^3s^{-1}	[40]
	1×10^{-11} cm^3s^{-1}	[42]
Three body attachment:		
$e + O_2 + M \rightarrow O_2^- + M$	2×10^{-30} cm^6s^{-1} $(M=O_2)$	[65]
	1×10^{-31} cm^6s^{-1} $(M=N_2)$	[65]
	3×10^{-30} cm^6s^{-1} $(M=CO_2)$	[65]
$e + O + M \rightarrow O^- + M$	1×10^{-31} cm^6s^{-1} $(M=O_2)$	[66]
	1×10^{-31} cm^6s^{-1} $(M=N_2)$	[66]
Associative detachment:		
$O^- + CO \rightarrow CO_2 + e$	$5.8\times10^{-9}\times T_e^{-0.4}$ cm^3s^{-1}	[67]
	7×10^{-10} cm^3s^{-1}	[32, 68-69]
	7.3×10^{-10} cm^3s^{-1}	[37]
$O^- + O \rightarrow O_2 + e$	2×10^{-10} cm^3s^{-1}	[30, 38-40]
$O^- + O_2 \rightarrow O_3 + e$	1×10^{-12} cm^3s^{-1}	[38-39]
$O^- + CO_2 \rightarrow CO_2 + O + e$	4×10^{-12} cm^3s^{-1}	[38]
$O^- + N_2 \rightarrow N_2O + e$	1×10^{-12} cm^3s^{-1}	[38]
Neutral dissociation:		
$CO_2 + e \rightarrow CO + O + e$	present work	
$O_2 + e \rightarrow O + O + e$	present work	
$H_2O + e \rightarrow H + OH + e$	2×10^{-9} cm^3s^{-1}	[30]

Neutral two-body reaction:

$O + O_3 \rightarrow O_2 + O_2$	$8\times10^{-12}\exp(-2060/T)$ cm^3s^{-1}	[32, 34-35]
	9×10^{-15} cm^3s^{-1} (T=300 K)	[31,70]
$O + OH \rightarrow O_2 + H$	3.3×10^{-11} cm^3s^{-1}	[31]
$O + CO \rightarrow CO_2$	2×10^{-20} cm^3s^{-1}	[31]
$O + N \rightarrow NO$	2×10^{-17} cm^3s^{-1}	[71]
	1.5×10^{-13} cm^3s^{-1}	[31]
$CO + OH \rightarrow CO_2 + H$	1.5×10^{-13} cm^3s^{-1}	[31, 39-40]
	1.44×10^{-13} cm^3s^{-1}	[72]
$O_2 + H \rightarrow O + OH$	1.2×10^{-15} cm^3s^{-1}	[31]

Neutral three-body reaction:

$O + O + M \rightarrow O_2 + M$	8×10^{-33} cm^6s^{-1} ($M=CO_2$)	[32, 36]
	7.2×10^{-33} cm^6s^{-1} ($M=CO_2$)	[71]
	3×10^{-33} cm^6s^{-1} ($M=N_2, O_2$)	[32, 36, 70]
	2.8×10^{-33} cm^6s^{-1} ($M=N_2$)	[36]
$O + O_2 + M \rightarrow O_3 + M$	$4.2\times10^{-34}(T/300)^{-2}$ cm^6s^{-1} (laser gas)	[32]
	$5.6\times10^{-34}(T/300)^{-2.8}$ cm^6s^{-1} ($M=N_2$)	[35]
	$6\times10^{-34}(T/300)^{-2}$ cm^6s^{-1} ($M=N_2, O_2$)	[32]
	5.7×10^{-34} cm^6s^{-1} ($M=N_2$)	[74]
	3.8×10^{-34} cm^6s^{-1} (M=Ar)	[73]
	3.9×10^{-34} cm^6s^{-1} (M=Ar)	[74]
$O + CO + M \rightarrow CO_2 + M$	2.4×10^{-36} cm^6s^{-1} ($M=CO_2$)	[71]
	2×10^{-36} cm^6s^{-1} ($M=CO_2$)	[75]

Ion-molecule reaction:

$O^- + CO_2 + M \rightarrow CO_3^- + M$	9×10^{-29} cm^6s^{-1} ($M=CO_2$)	[31, 69]
	3×10^{-28} cm^6s^{-1} ($M=O_2$)	[76]

APPENDIX B
LIGHT EMISSION INTENSITY AND ROTATIONAL LINE STRENGTH

The emission intensity of the transition from the upper state n to the lower state m is expressed as in Herzberg [50]

$$I_{em.}^{nm} = N_n h c \nu_{nm} A_{nm} . \tag{B.1}$$

where N_n is the number of molecules in the initial state; ν_{nm} is the wave number of the transition in units of cm^{-1}; h and c are Planck constant and the speed of light; A_{nm} is the Einstein transition probability of spontaneous emission, which is proportional to the matrix elements of the electric dipole moment:

$$A_{nm} = \frac{64\pi^4 \nu_{nm}^{\ 3}}{3h} \frac{\sum |R^{nm}|^2}{d_n} . \tag{B.2}$$

R^{nm} is the matrix elements of the electric dipole moment; d_n is the degeneracy of the initial state. In particular, for the emission of rotation-vibration band, the distribution of the number of molecules, $N_{J'}$, in the rotational quantum number J' at the temperature T is

$$N_{J'} = \frac{N}{Q_r}(2J'+1)e^{-\frac{BJ'(J'+1)hc}{kT}} . \tag{B.3}$$

where N is the gas density, Q_r is rotational state sum or partition function, B is the rotational constant of the state, k is the Boltzmann constant. Substituting the A_{nm} and $N_{J'}$ into Eq. (B.1) and letting the degeneracy $d_n = 2J' + 1$, the intensity of the emission in the rotation-vibration spectrum can be rewritten [50] as

$$I_{em.} = \frac{64\pi^4 c N \nu^4}{3Q_r}\left(\sum |R^{nm}|^2\right) e^{-\frac{B'J'(J'+1)hc}{kT}} \tag{B.4}$$

$$I_{em.} = \frac{2C_{em.}\nu^4}{Q_r} S_{J'} e^{-\frac{B'J'(J'+1)hc}{kT}} \tag{B.5}$$

$S_{J'}$ is the line strength and a part of $\Sigma|R^{nm}|^2$ and depends on J', and $C_{em.}$ is a constant.

The formulae for the line strengths of the symmetric top were given first by Hönl and London [52] based on the old quantum theory, and were later derived on the basis of wave mechanic by Dennison [53], Reiche and Rademacher and others [54].

For $\Delta\Lambda = 0$ the Hönl-London formulae are:

$$S_{J''}^{R} = \frac{(J''+1+\Lambda'')(J''+1-\Lambda'')}{J''+1} = \frac{(J'+\Lambda')(J'-\Lambda')}{J'}$$
$$S_{J''}^{Q} = \frac{(2J''+1)\Lambda''^{2}}{J''(J''+1)} = \frac{(2J'+1)\Lambda'^{2}}{J'(J'+1)} \qquad \text{(B.6)}$$
$$S_{J''}^{P} = \frac{(J''+\Lambda'')(J''-\Lambda'')}{J''} = \frac{(J'+1+\Lambda')(J'+1-\Lambda')}{J'+1}$$

For $\Delta\Lambda' = +1$

$$S_{J''}^{R} = \frac{(J''+2+\Lambda'')(J''+1+\Lambda'')}{4(J''+1)} = \frac{(J'+\Lambda')(J'-1+\Lambda')}{4J'}$$
$$S_{J''}^{Q} = \frac{(J''+1+\Lambda'')(J''-\Lambda'')(2J''+1)}{4J''(J''+1)} = \frac{(J'+\Lambda')(J'+1-\Lambda')(2J'+1)}{4J'(J'+1)} \qquad \text{(B.7)}$$
$$S_{J''}^{P} = \frac{(J''-1-\Lambda'')(J''-\Lambda'')}{4J''} = \frac{(J'+1-\Lambda')(J'+2-\Lambda')}{4(J'+1)}$$

For $\Delta\Lambda' = -1$

$$S_{J''}^{R} = \frac{(J''+2-\Lambda'')(J''+1-\Lambda'')}{4(J''+1)} = \frac{(J'-\Lambda')(J'-1-\Lambda')}{4J'}$$
$$S_{J''}^{Q} = \frac{(J''+1-\Lambda'')(J''+\Lambda'')(2J''+1)}{4J''(J''+1)} = \frac{(J'-\Lambda')(J'+1+\Lambda')(2J'+1)}{4J'(J'+1)} \qquad \text{(B.8)}$$
$$S_{J''}^{P} = \frac{(J''-1+\Lambda'')(J''+\Lambda'')}{4J''} = \frac{(J'+1+\Lambda')(J'+2+\Lambda')}{4(J'+1)}$$

where J is the rotational level; Λ is the total angular momentum. P, Q, and R are the labels of the rotational transitions which follow the selection rule, $\Delta J = -1, 0, +1$, respectively. The single prime and double prime stand for the upper state and the lower state, respectively.

VITA

NAME Thao Hoang Dinh
ADDRESS Department of Physics, Old Dominion University, 4600 Elkhorn Ave, Norfolk, VA 23529

EDUCATION

May 2002 **Ph.D.**, Applied Physics, Old Dominion University
Dissertation: *Decomposition of Carbon Dioxide in a Capacitively Coupled Radio Frequency Discharge*

Auguest 1995 **B.S.**, Physics, Old Dominion University
Honor Thesis: *Measurement of a Sodium Atomic Beam's Velocity*

HORNORS AND AWARDS

1999 Arch T. Colwell Award for the best paper at the 27th International Conference on Environmental System

1995-1997 GAANN Fellowship, Graduate School of Science, Old Dominion University, 1995-1997

1995-1998 Outstanding Graduated Student Award of the year, Old Dominion University, 1995

PROFESSIONAL MEMBERSHIP

American Physical Society